

ISSN 0914-9244
CODEN JSTEEW

Journal of
Photopolymer
Science and Technology
Volume 36 Number 4

2023

JOURNAL OF PHOTOPOLYMER SCIENCE AND TECHNOLOGY

Home Page <https://www.spst-photopolymer.org>
<https://www.jstage.jst.go.jp/browse/photopolymer>

Journal of Photopolymer Science and Technology publishes papers on the scientific progress and the technical development of photopolymers.

Editorial Board

Editor-in-Chief:

Hiroyuki MAYAMA, *Asahikawa Medical University*

Editors:

Masayuki ENDO, *Osaka University*

Teruaki HAYAKAWA, *Tokyo Institute of Technology*

Yoshihiko HIRAI, *Osaka Metropolitan University*

Takashi HIRANO, *SUMITOMO BAKELITE CO., LTD.*

Taku HIRAYAMA, *Hoya Co., Ltd.*

Hideo HORIBE, *Osaka Metropolitan University*

Takanori ICHIKI, *The University of Tokyo*

Takashi KARATSU, *Chiba University*

Yoshio KAWAI, *Shin-Etsu Chemical Co., Ltd.*

Shin-ichi KONDO, *Gifu Pharmaceutical University*

Hiroto KUDO, *Kansai University*

Kazuma KURIHARA, *AIST*

Takayuki MUROSAKI, *Asahikawa Medical University*

Tomoki NAGAI, *JSR Corporation*

Haruyuki OKAMURA, *Osaka Metropolitan University*

Hideo OHKITA, *Kyoto University*

Itaru OSAKA, *Hiroshima University*

Shu SEKI, *Kyoto University*

Atsushi SEKIGUCHI, *Litho Tech Japan Corporation*

Takehiro SESHITA, *Tokyo Ohka Kogyo Co., Ltd.*

Akinori SHIBUYA, *Fuji Film, Co., Ltd.*

Kuniharu TAKEI, *Hokkaido University*

Jun TANIGUCHI, *Tokyo University of Science Takumi*

UENO, *Shinshu University*

Takeo WATANABE, *University of Hyogo*

Masashi YAMAMOTO, *Nat. Inst. Tech. Kagawa College*

International Advisory Board

Robert D. ALLEN, *IBM Almaden Research Center*

Paul F. NEALEY, *University of Chicago*

C. Grant WILLSON, *The University of Texas*

Ralph R. DAMMEL, *EMD Performance Materials*

Christopher K. OBER, *Cornell University*

The Editorial Office

Assoc. Prof. Hiroyuki MAYAMA

Department of Chemistry, Asahikawa Medical University, 2-1-1-1 Midorigaoka-Higashi, Asahikawa, Hokkaido 078-8510, Japan.

FAX: +81-166-68-2782, e-mail: mayama@asahikawa-med.ac.jp

Information for Contributors

Submit Manuscripts to the SPST Homepage (Journal --> Submission of Papers --> Editorial Manager). Submission is a representation that the manuscript has not been published previously elsewhere. The manuscript should be accompanied by a statement transferring copyright from the authors (or their employers-whoever holds the copyright) to the Society of Photopolymer Science and Technology. A suitable form for copyright transfer is available from the SPST Homepage. This written transfer of copyright, which previously was assumed to be implicit in the act of submitting a manuscript, is necessary under the Japan copyright law. Further information may be obtained from the "Manual for Manuscript Writing" at the SPST Homepage.

Proofs and All Correspondence: Concerning papers in the process of publication should be addressed to the Editorial Office.

Manuscript Preparation: All the papers submitted are reproduced electronically as they were. For this reason, the manuscripts should be prepared according to

the Manual for Manuscript Writings shown at the SPST Homepage.

Subscription Price (Airmail Postage included):

¥12,000 (in Japan), US\$ 150.00 (for Foreign)

Subscriptions, renewals, and address changes should be addressed to the Editorial Office. For the address changes, please send both old and new addresses and, if possible, include a mailing label from the wrapper of recent issue. Requests from subscribers for missing journal issues will be honored without charge only if received within six months of the issue's actual date of publication; otherwise, the issue may be purchased at the single-copy price.

Publication Charge (Reprint Order): To support a part of the cost of publication of journal pages, the author's institution is requested to pay a page charge of ¥3,000 per page (with a one-page minimum) and an article charge of ¥12,000 per article. The page charge (if honored) entitles the author to 50 free reprints. For Errata the minimum page charge is ¥3,000, with no articles charge and no free reprints.

JOURNAL
OF
PHOTOPOLYMER
SCIENCE
AND
TECHNOLOGY

Volume 36 Number 4

2023

Published by

THE SOCIETY OF PHOTOPOLYMER SCIENCE AND TECHNOLOGY

THE SOCIETY OF PHOTOPOLYMER SCIENCE AND TECHNOLOGY (SPST)

<https://www.spst-photopolymer.org>

Honorary President:
Minoru TSUDA
SPST & Chiba University

President:
Takeo WATANABE
SPST & University of Hyogo

Director of Publication:
Hiroyuki MAYAMA
Asahikawa Medical University

Director of Scientific Program:
Itaru OSAKA
Hiroshima University

Director of International Affairs:
Teruaki HAYAKAWA
Tokyo Institute of Technology

Director of Administration:
Hirotō KUDO
Kansai University

Office of the Administration:
c/o Prof. Hirotō KUDO
*Department of Chemistry and Materials
Engineering, Faculty of Chemistry,
Materials and Bioengineering, Kansai
University
3-3-35, Tamate-cho, Suita-shi, Osaka
564-8680, Japan
e-mail: hkudo@kansai-u.ac.jp*

THE SPST REPRESENTATIVES 2023

Robert ALLEN, *IBM*
Hitoshi ARAKI, *Toray Co., Ltd.*
Masataka ENDO, *Osaka University*
Teruaki HAYAKAWA, *Tokyo Institute of Technology*
Taku HIRAYAMA, *HOYA Co., Ltd.*
Yoshihiko HIRAI, *Osaka Metropolitan University*
Takashi HIRANO, *Sumitomo Bakelite Co., Ltd.*
Hideo HORIBE, *Osaka Metropolitan University*
Takanori ICHIKI, *The University of Tokyo*
Takashi KARATSU, *Chiba University*
Yoshio KAWAI, *Shin-Etsu Chemical Co., Ltd.*
Shin-ichi KONDO, *Gifu Pharmaceutical University*
Hirotō KUDO, *Kansai University*
Kazuma KURIHARA, *AIST*
Masayuki KUZUYA, *Chubu Gakuin University*
Hiroyuki MAYAMA, *Asahikawa Medical University*
Takayuki MUROSAKI, *Asahikawa Medical University*
Seiji NAGAHARA, *Tokyo Electron Ltd.*

Tomoki NAGAI, *JSR Corporation*
Hideo Ohkita, *Kyoto University*
Haruyuki OKAMURA, *Osaka Metropolitan University*
Itaru OSAKA, *Hiroshima University*
Takehiro SEHITA, *Tokyo Ohka Kogyo Co., Ltd.*
Shu SEKI, *Kyoto University*
Atsushi SEKIGUCHI, *Litho Tech Japan Corporation*
Kohei SOGA, *Tokyo University of Science*
Akinori SHIBUYA, *Fuji Film Co., Ltd.*
Kuniharu TAKEI, *Hokkaido University*
Jun TANIGUCHI, *Tokyo University of Science*
Minoru TSUDA, *SPST & Chiba University*
Takumi UENO, *Shinshu University*
Takeo WATANABE, *SPST & University of Hyogo*
Shinji YAMAKAWA, *University of Hyogo*
Masahi YAMAMOTO, *Nat. Inst. Tech. Kagawa College*
Takashi YAMASHITA, *Tokyo University of Technology*
Wang YUEH, *Intel*

Notice about photocopying

Prior to photocopying any work in this publication, the permission is required from the following organization which has been delegated for copyright clearance by the copying owner of this publication.

- In the USA
Copying Clearance Center Inc.
222 Rosewood Drive, Danvers MA 01923, USA
Tel: 1-978-750-8400, Fax: 1-978-750-4744, e-mail: info@copyright.com
<http://www.copyright.com>
- Except in the USA
Japan Academic Association for Copyright Clearance (JAACC)
9-6-41 Akasaka, Minato-ku, Tokyo 107-0052, Japan
Tel: 81-3-3475-5618, Fax: 81-3-3475-5619, e-mail: info@jaacc.jp
<http://www.jaacc.org>

Novel Photoinitiator System for Simultaneous Physical Drying and Free Radical Polymerization of Water-Borne Dispersions with Near-Infrared Excitation

(Dedicated to D.C. Neckers (1938-2022) and Y. Yagci (1952-2023) according to their achievements in photopolymer science)

Lukas Appelhoff^{1*}, Nicolas Hornemann², Remco Fokkink³,
Jochen S. Gutmann⁴, Thomas E. Kodger³, and Bernd Strehmel^{1**}

¹Niederrhein University of Applied Sciences and Institute for Coatings and Surface Chemistry (ILOC), Adlerstr. 1, 47798 Krefeld, Germany

²ACTEGA Terra GmbH, Industriestr. 12, 31275 Lehrte, Germany

³Wageningen University & Research, Droevendaalsesteeg 4, 6708 PB Wageningen, Netherlands

⁴University Duisburg-Essen, Universitätsstraße 2, 45141 Essen, Germany

[*lukas.appelhoff@hochschule-niederrhein.de](mailto:lukas.appelhoff@hochschule-niederrhein.de) [**bernd.strehmel@hs-niederrhein.de](mailto:bernd.strehmel@hs-niederrhein.de)

Energy efficient processes in industry represent a key factor to realize a fast transition to renewable energy sources. In the coatings industry, oven technologies applied for drying and curing, mainly contribute to energy consumption. Substitution of these wasting technologies by near infrared radiation (NIR) in combination with a NIR-absorber represents a promising alternative to reduce the energy use. Here, combining of a NIR-LED with a heptamethine cyanine operating as absorber can significantly accelerate the drying process of a water borne coating as measured by Laser Speckle Imaging (LSI). The combination of cyanine and bis(tert-butyl)iodonium salts as radical initiator results in an initiation system that efficiently works in combination with a NIR-LED to dry the coating followed by crosslinking in the same step. photo-DSC and FTIR measurements confirmed the results obtained. The use of a water compatible photoinitiator system based on a cyanine with sulfonate groups and bis(tert-butyl)iodonium lactate as water soluble cointiator opened the possibility to eliminate the cosolvent needed for film formation and to create a complete VOC free formulation.

Keywords: Water-borne Coatings, Near infrared, Drying, Curing, Cyanine, Iodonium Salt

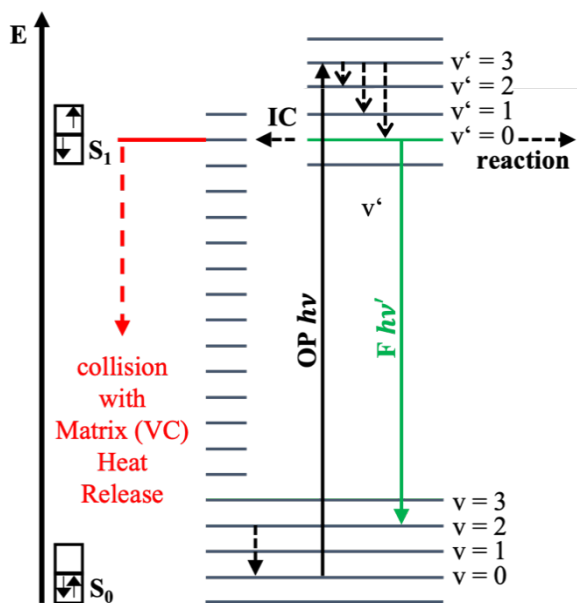
Nowadays, elimination of factors affecting climate change requires to consider renewable energy sources and their use in high-energy consuming production lines. This demand would be easier to achieve with a significant lower request of energy by enabling energy-efficient processes. In the coating industry, substitution of conventional oven technologies for drying and curing with high demand on energy address to enable energy saving technologies; that is efficient radiation technologies fitting into these goals. Although radiation curing technologies have been already well established

[1-4], conventional oven processes have been still widely used [5, 6]. Therefore, there exists a need to develop alternatives to make the transition easier feasible.

Cyanines may receive a certain operational part to solve these issues. They are very efficient light absorber molecules with an odd number of methine groups [7-9]. For example, heptamethine based cyanines exhibit strong absorbance. These compounds usually possess very high extinction coefficients; that is $>10^5 \text{ M}^{-1}\text{cm}^{-1}$. An additional vinyl group in the methine chain results in a

bathochromic absorption shift of the absorption maximum of about 100 nm known as the 100 nm rule [9].

Exposure of the cyanine with a suitable light source results in one-photon absorption (OP). Excitation promotes the molecules ground state (S_0) into the first excited state (S_1). The latter can radiatively deactivate by fluorescence (F) or non-radiatively by internal conversion (IC). Here, a higher vibrational level of the ground state couples with the lowest vibrational level of the S_1 resulting in formation of a very hot state assigned to the S_0 . Collision of this hot state with matrix molecules results in transfer of the excessive energy to the surrounding matrix. This released heat can operate in physical processes such as melting of powders [5, 10-13]. On the other hand, vibrational relaxation cannot be seen as the major non-radiative reaction pathway because the very hot molecule would burn during this stepwise deactivation procedure. Until today, the description for generation of heat in such processes has been poorly explained in literature. Scheme 1 shows the proceeding processes. The main deactivation in heptamethine cyanines typically proceeds nonradiative with a yield of > 80% with respect to the absorbed energy [14-17]. Fluorescence occurs as minor event [4].



Scheme 1. Simplified photophysical processes of the electronic states of cyanines (redrawn from [18]).

Furthermore, the S_1 of the photoexcited cyanine can react in an oxidative mechanism with an acceptor if the free enthalpy of the photoinduced

electron transfer (PET) results in negative values. The oxidation potential of the cyanine and the reduction potential of the iodonium cation drive this system in the right direction by excitation at 860 nm [4]. The PET results in efficient bleaching of cyanine with minor possibility of electron back transfer. PET leads to reduction of the iodonium cation. The respective $Ar_2I\cdot$ radical fast decomposes in an iodine arene and the respective aryl radical. The latter efficiently initiates radical polymerization. This work mainly focused on radical polymerization. Here we focus only on radical polymerization because processing proceeded in water.

As already described, heptamethine cyanines efficiently absorb near-infrared radiation [4]. Deactivation mostly proceeds nonradiative while collision with matrix molecules leads to a huge temperature increase of the surrounding matrix. In other words, excitation of these compounds with a light source emitting a suitable emission wavelength (diode Laser or light emitting diodes) can lead to an increase of several hundred degrees Celsius of the matrix in a short time frame depending on heat capacity of the system, heat flow conditions, irradiation intensity, concentration, and thickness.

Accordingly, experiments approved the possibility to use this heat generated for the drying of aqueous coating dispersions. This was also claimed in a recent patent application [19]. Nevertheless, observation of the physical drying process applying photonic sources instead of ovens does not appear as trivial. Water often interferes the signal taken to analyze the process of lot. Thus, a defined thickness needs to be established with a sample has no coverage on top. Furthermore, high spatial and temporal resolution can be seen as additional parameters together with a defined relative humidity of the surroundings. Thus, an airflow needs to be realized complementing the setup to get reliable data from those drying experiments. Increasing temperature of the sample should not significantly interfere the signal. In addition, opaque/pigmented systems should not show major issues during the measurement. Nevertheless, thickness appears as an additional important parameter because it may affect diffusion of volatile components such as water/solvent while penetration of absorbed light into the film depicts a further point controlled by the absorption of the cyanine by Lambert-Beer's Law.

These criteria represent big obstacles for methods

such as real-time infrared spectroscopy (RT-FTIR), rheology measurements, magnetic resonance imaging (MRI), optical microscopy or classical gravimetric techniques.

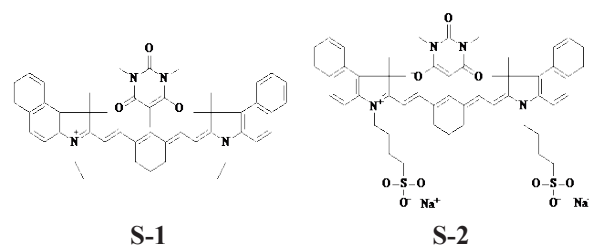
Laser Speckle Imaging (LSI) represents a suitable technique meeting all these criteria. It was introduced in the early 1980's to map the retinal blood flow as studied by multiple scattering photons [20]. In this work, LSI was applied to collect scattered light of pigment particles (TiO₂) added to study temporal and spatial changes proceeding upon exposure with a coherent emitting 532 nm laser. This source generates a speckle image resulting in a 2D interference pattern. The information available from such experiments where speckle images were generated (see SI for an example) relate to the instantaneous position of the pigment particles [20]. The scattered light and its propagation in the sample possesses a significant higher speed compared to the particle movement. This movement completely proceeds randomized after a small number of scattering events. The information provided by the speckle image relates therefore to the instantaneous position of the pigment particles. Consequently, spatial comparison of the speckle intensities within the image of another speckle intensity after a certain delay or lag time, namely τ , results in an intensity fluctuation available from the measurement. As a result, this quantity gives information about the dynamics and mobility of pigment particles within the coating over experimental time t . Equation 1 shows the relation between these parameters helping to understand the complex spatial dynamics. It appropriately fits the obtained data to an exponential decay function $g_1(t, \tau)$:

$$g_1(t, \tau) = \exp(-\gamma[\tau/\tau_0(t)]^{\alpha(t)}) \quad (1)$$

The value γ relates to an experimental numerical constant which was defined elsewhere [21]. The most important parameters are the characteristic relaxation time $\tau_0(t)$ to define the drying process. This can be seen as a quantity related to the viscosity of the drying coating solution on the substrate. Furthermore, the stretching/compressing exponent $\alpha(t)$ represents as a value for the type of motion of the particles. Here, $\alpha < 0.5$ indicates sub-diffusive dynamics while values of $\alpha = 0.5$ relate to Brownian/diffusive dynamics. Values of α appearing above this number are caused by super-diffusive processes approaching ballistic motion.

Three different samples were analyzed during the drying; that is the neat coating, the coating comprising cyanine **S-2**, and the coating comprising the cyanine **S-2** processed with near-infrared

irradiation (NIR). The sample comprising **S-2** and with no processing of NIR radiation was brought to the experiment to evaluate if the laser of the LSI affects somehow the measurement of the sample. This is relevant because the cyanines possess notable absorption in the visible region although it is lower compared to the absorption in NIR. Nevertheless, most cyanines possess a minimum of absorption at the emission wavelength of the Laser (532 nm). In the case of cyanine **S-2**, the extinction coefficient at 532 nm was $2500 \text{ M}^{-1} \times \text{cm}^{-1}$ in water which is around 17 times lower compared to the absorption maximum at 795 nm ($43080 \text{ M}^{-1} \times \text{cm}^{-1}$). This ratio can be larger for other cyanines. Thus, the laser intensity was kept as low as possible. Here, the laser operated with 25 mW to keep excitation of **S-2** as low as possible by the green laser.



Nevertheless, the measurement denoted a small impact of the laser resulting in a shift of $\tau_0(t)$ to about 84 s while $\alpha(t)$ had an offset of 87 s (see blue and black data points Fig. 1). The first kink at t_1 in the $\tau_0(t)$ refers to the concentration. It relates therefore close to the packing of the scattering particles resulting in a constant mobility. As expected, a faster drying could be observed in the sample with 0.2 wt% **S-2** applying NIR radiation as shown by the red data points in Fig. 1. The first kink t_1 appeared at 287 s significant earlier compared to a value of 1329 s of the same sample without NIR radiation (●). This confirmed faster drying of at least 1042 s of the coating comprising absorber **S-2** after processing with NIR radiation. Interestingly, there was a small decrease of $\tau_0(t)$ to about 35 s in the sample dried with NIR (●), which did not proceed in the other samples. Possibly, this indicates a decrease in viscosity because of a rapid heating on a molecular level caused by absorption of NIR radiation during exposure. After a small decrease at the beginning, a rapid increase of viscosity was observed resulting in a value of 287 s where $\tau_0(t)$ starts to decrease again. This rapid increase related to water evaporation. It referred to the close packing followed by the deformation of the binder particles due to the capillary pressure [22]. In the capillaries formed, the TiO₂ particles were likely to be drawn downward toward the substrate as drying continues. This led to a temporary increase in mobility. Also,

the value of $\alpha(t)$ increased, whereas the motion of the particles became more and more advective. Interestingly, there was a bigger time lag in the kink of $\tau_0(t)$ and $\alpha(t)$ in the radiation dried sample (●) which could indicate a skin formation on the surface due to the fast drying/strong absorption. Such events would be undesired. Nevertheless, also the kink of the $\alpha(t)$ value of the radiation dried sample (●) occurred already at 801 s compared to a value of 1248 s for the same sample without irradiation (●), which would still enhance the drying about 447 s / 7:27 min. In general, the increased temperature promotes film formation by increasing the mobility of the particles [22].

Physical dried coatings often exhibit a poor resistance against chemical or mechanical impacts. Therefore, chemical crosslinking with NIR radiation appeared as a further challenge of this type of water-borne coating. Conventional coatings of this type normally were dried in energy consuming convection ovens followed by consecutive curing UV-radiation in a two-step process [19]. Here we propose a process with NIR of physical drying and curing in just one step. This would substitute the energy consuming drying process as well as

hazardous UV-radiation.

Here the heptamethine cyanines operate as a sensitizer to reduce iodonium salts resulting in formation of free radicals to initiate free radical polymerization (FRP)[15, 16]. In the first step, an already known photoinitiator system used for 100% systems [15,16] was modified to obtain initiating components facilitating their use in a water-borne coating. Butyldiglycol was added as cosolvent. The initiator system contains the cyanine S-1 and an iodonium salt with different counter ions such as nitrate (NO₃), a perfluorinated aluminate (ALU), tetraphenylborate (BPh₄), hexafluoro-phosphate (PF₆), Bis(trifluoromethanesulfonyl)-imide (NTf₂) and lactate (LAC). Bis-(4-methyl-phenyl)-iodonium was only used as cation for the nitrate counter anion (Table 1). The remaining experiments used bis(tert-butyl)iodonium salts. The use of the cosolvent was necessary to solve the cyanine S-1 and most of the iodonium salts.

The reactivity of the formulations was determined from the peak in the exothermic signal of the photo-DSC (Fig. 2). Surprisingly the iodonium salt with the lactate anion appeared as the most reactive coinitiator. This was counter intuitive

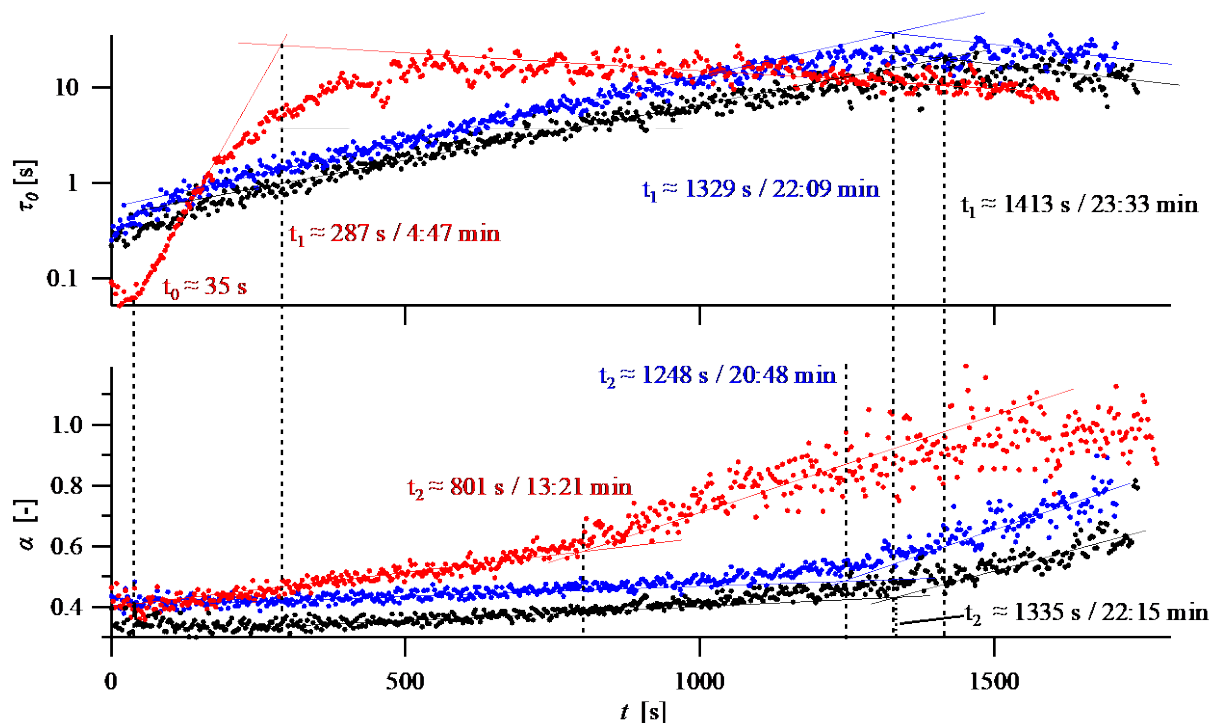


Fig. 1. Physical drying observed by Laser Speckle Imaging (LSI). τ_0 : relates to viscosity, α : type of motion of the particles ($\alpha < 0.5$ indicate sub-diffusive dynamics, $\alpha = 0.5$ indicate Brownian motion, $\alpha = 1$ indicate ballistic motion) – kink in either τ_0 or α marks phase transition - (●) 0.2 wt% S-3/with NIR ($\lambda_{\max}=820$ nm, $E \approx 200$ mW/cm²), (●) 0.2 wt% S-2/no NIR (●) pure Coating/no NIR

because this anion did not perform well in 100% systems with a less polar matrix [16]. Additionally, it opens the possibility of eliminating the co-solvent, as the iodonium salt with lactate has good compatibility with aqueous solutions. This leads to formulation with less VOC. The iodonium nitrate was not analyzed more in detail because ion exchange processes as well as precipitation was expected to interfere the experiment. Therefore, the focus was put on the iodonium lactate. Furthermore, the cyanine requests also a sufficient water solubility to improve the compatibility in the system processed. This can be achieved by introduction of sulfonate groups in the side chain or at the indolium rings. Consequently, the cyanine **S-1** was substituted resulting in **S-2**. This reduced the reactivity of the system (Fig. 3), which can be explained by the lower extinction coefficient of **S-2** in butyldiglycol ($45788 \text{ M}^{-1}\text{cm}^{-1}$ at $\lambda_{\text{max}} = 799 \text{ nm}$). For comparison, **S-1** exhibited a significant larger extinction coefficient in organic surrounding ($198480 \text{ L}\cdot\text{cm}^{-1}\text{mol}^{-1}$ at $\lambda_{\text{max}} = 794 \text{ nm}$). Consequently, **S-2** absorbs less radiation/energy compared to **S-1** based on the same molar amount explaining the lower reactivity. Replacement of the remaining cosolvent butyldiglycol by water led to a small decrease of the reactivity.

Table 1. Structures of the nitrate, aluminate and tetraphenylborate iodonium salts.

Name	Cation	Anion
NO3		NO_3^-
ALU		
BPh4		

In summary, we report the successful drying and simultaneous curing of a waterborne coating with near infrared (NIR) and a photoinitiator system based on a heptamethine cyanine (**S-2**) and iodonium lactate (IS-LAC) being dynamically measured using Laser Speckle Imaging. With this approach the physical drying can be accelerated, and high double bond conversion are achievable.

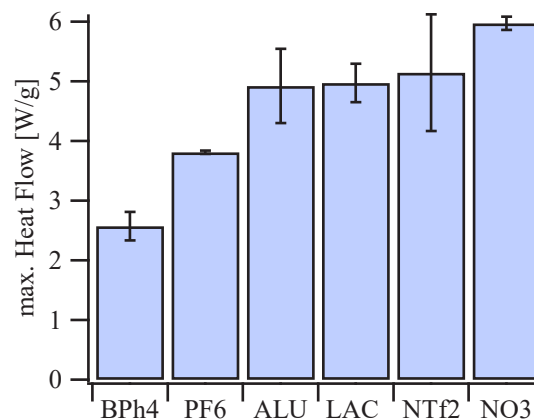


Fig. 2. Max reactivity of different Ionium-Salts in combination with **S-1** measured by photo-DSC with NIR radiation ($\lambda_{\text{max}} = 820 \text{ nm}$, $E \approx 200 \text{ mW/cm}^2$) - the error bars show the standard deviation ($n = 2$).

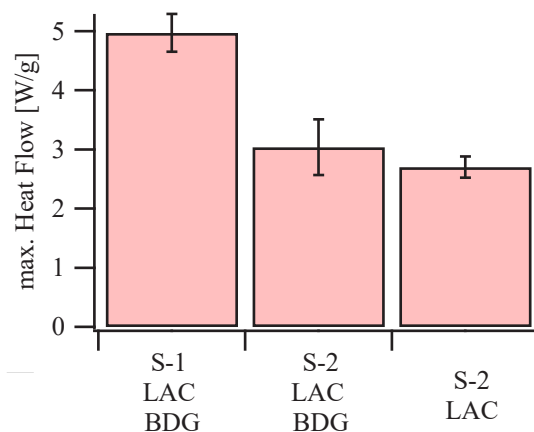


Fig. 3. Max reactivity of different photoinitiator system in combination with and without the cosolvent butyldiglycol (BDG) measured by photo-DSC with NIR radiation ($\lambda_{\text{max}} = 820 \text{ nm}$, $E \approx 200 \text{ mW/cm}^2$) - the error bars show the standard deviation ($n = 2$).

Experimental Section

More details about the materials used, the coating formulation as well as the measurement setups can be found in the supporting information.

References

1. S. Dadashi-Silab, S. Doran, and Y. Yagci, *Chem. Rev.*, **116** (2016) 10212.
2. C. Aydogan, G. Yilmaz, A. Shegiwal, D. M. Haddleton, and Y. Yagci, *Angew. Chem. Int. Ed. Engl.*, **61** (2022), e202117377.
3. A. Kocaarslan, K. Kaya, S. Jockusch, and Y. Yagci, *Angew. Chem. Int. Ed. Engl.*, **61** (2022), e202208845.
4. B. Strehmel, C. Schmitz, C. Kütahya, Y. Pang,

- A. Drewitz, and H. Moustroph, *Beilstein J. Org. Chem.*, **16** (2020) 415.
5. C. Schmitz and B. Strehmel, *Farbe Lack*, **124** (2018) 40.
 6. M. Meixner, J. Stollenwerk, W. Weigt, and M. Zschuppe, *Farbe Lack*, (2015) 89.
 7. H. Moustroph, *Dyes Pigments* (2022) 110783.
 8. H. Moustroph, *Phys. Sci. Rev.*, **4** (2019) 20190040.
 9. H. Moustroph, *Phys. Sci. Rev.*, **5** (2019) 20190084.
 10. C. Schmitz and B. Strehmel, *Eur. Coat. J.*, **124** (2018) 40.
 11. C. Schmitz, D. Oprych, C. Kutahya, and B. Strehmel, "NIR Light for Initiation of Photopolymerization", in *Photopolymerisation Initiating Systems* (Eds.: J. Lalevée, J.-P. Fouassier), Royal Society of Chemistry, 2018, pp. 431-478.
 12. C. Schmitz and B. Strehmel, *ChemPhotoChem*, **1** (2017) 26.
 13. C. Schmitz, B. Gökce, J. Jakobi, S. Barcikowski, and B. Strehmel, *ChemistrySelect*, **1** (2016), 5574.
 14. T. Brömme, C. Schmitz, D. Oprych, A. Wenda, V. Strehmel, M. Grabolle, U. Resch-Genger, S. Ernst, K. Reiner, D. Keil, P. Lüs, H. Baumann, and B. Strehmel, *Chem. Eng. Technol.*, **39** (2016) 13.
 15. T. Brömme, C. Schmitz, N. Moszner, P. Burtscher, N. Strehmel, and B. Strehmel, *ChemistrySelect*, **1** (2016) 524.
 16. T. Brömme, D. Oprych, J. Horst, P. S. Pinto, and B. Strehmel, *RSC Adv.*, **5** (2015) 69915.
 17. C. Schmitz, A. Halbhuber, D. Keil, and B. Strehmel, *Prog. Org. Coat.*, **100** (2016) 32.
 18. Q. Wang, S. Popov, A. Feilen, V. Strehmel, and B. Strehmel, *Angew. Chem. Int. Ed. Engl.*, **60** (2022) 26855.
 19. L. Appelhoff, Q. Wang, and B. Strehmel, WO2022200192, Hochschule Niederrhein, 2022.
 20. A. F. Fercher and J. D. Briers, *Opt. Commun.*, **37** (1981) 326.
 21. H. M. van der Kooij, R. Fokkink, J. van der Gucht, and J. Sprakel, *Sci. Rep.*, **6** (2016) 34383.
 22. P. Mischke and B. Strehmel, *Filmbildung: 2.*, complete revised version, Vincentz Network, Hannover, 2018.

Supporting Information

Novel Photoinitiator System for Simultaneous Physical drying and Free Radical Polymerization of Water-Borne Dispersions with Near-Infrared Excitation

Lukas Appelhoff^{1*}, Nicolas Hornemann², Remco Fokkink³, Jochen S. Gutmann⁴, Thomas Kodger³, and Bernd Strehmel¹

¹Niederrhein University of Applied Sciences and Institute for Coatings and Surface Chemistry (ILOC), Adlerstr. 1, 47798 Krefeld, Germany

²ACTEGA Terra GmbH, Industriestr. 12, 31275 Lehrte, Germany

³Wageningen University & Research, Droevendaalsesteeg 4, 6708 PB Wageningen, Netherlands

⁴University Duisburg-Essen, Universitätsstraße 2, 45141 Essen, Germany

Coating Formulation:

The coating for LSI and for the curing measurements were prepared according to the following Table and homogenized by a SpeedMixer from Hauschild. The curable polyurethane acrylate dispersion was provided as Lux 260 by Alberdingk & Boley, The TiO₂-Dispersion was provided as K-9900 by Kronos, the thickener Rheobyk-425, the defoamer BYK-025 and the wetting additive Rheo-BYK-UV3530 were provided by BYK-Chemie GmbH. The cyanine S-1 and S-2 were provided as S2265 and S2283 from FEW Chemicals. Two of the Bis(4-tert-butylphenyl)iodonium salts were purchased as S2617 (aluminate) from FEW Chemicals and as B2380 (hexafluorophosphate) from TCI Chemicals. The other (lactate, ntf2, tetraphenylborate) as well as the Bis(methylphenyl)iodoniumnitrat were prepared in our lab according to T. Brömme, *Untersuchungen zur NIR-sensibilisierten radikalischen Photopolymerisation in multifunktionellen Monomeren*, 2016, University Duisburg-Essen, PhD Dissertation.

Type	Amount [%]
curable Polyurethanacrylate	58
TiO ₂ dispersion (50%ig)	19
Water	19
Rheology Additive	1
Defoamer	1
Wetting Additive	1
Cyanine	x
Iodonium Salt	y
	100%

Drying Time - LSI

The prepared coatings were coated with a four-way film applicator from Erichsen with 180 µm on glass plates. The sample was irradiated with a NIR-LED from Phoseon Technology with an emission maximum of 820 nm and approx. 200 mW/cm² in the LSI setup. The sample chamber was closed and flushed with nitrogen and held constant at approx. 45% relative humidity. The laser of the laser had an emission at 572 nm with 500 mW. We reduced the intensity to 25 mW through a transmission of only 5%. The LED light was filtered out by a Band Pass color filter (FGB37S). The field of view (FOV) was set to 150 x 150 with 500 fps.

Conversion - ATR FTIR

The prepared coatings were coated with with a four-way film applicator from Erichsen with 180 μm on microscope slides from VWR and put into an inert-box from Addix. The chamber was then flushed with nitrogen and the samples were irradiated with the NIR-LED (820 nm and approx. 1 W/cm²). After 1, 2, 5, 10 and 20 min samples were measured by ATR-FTIR (Vertex 80 by Bruker) and the conversion was calculated by the depletion of the C=C signal with respect to the C=O signal as internal reference (Equation 1).

$$\text{conversion [\%]} = \left(1 - \frac{Abs_{C=C, \text{ cured}} \cdot Abs_{C=O, \text{ dried}}}{Abs_{C=O, \text{ cured}} \cdot Abs_{C=C, \text{ dried}}}\right) \cdot 100 \tag{1}$$

Reactivity Measurement - Photo-DSC:

For the reactivity measurements with the photo-DSC the sampled were prepared only with the curable polyurethane acrylate dispersion provided as Lux 260 by Alberdingk & Boley as and water. The photo-DSC is based on the Q2000 DSC by TA Instruments with a self-made shutter system and a light fiber connection for incorporating the LED light. The NIR-LED from Phoseon Technology with an emission maximum of 820 nm were used with an irradiance of approx. 200 mW/cm². All samples were heat to 60°C for 15 min to evaporate the water. After that the sample is kept on 30°C and irradiated for 15 min. The used dry sample mass was between 2-3 mg for each measurement.

Type	Amount [%]
curable Polyurethanacrylate	36.2
Water	63.8
Cyanine	x
Iodonium Salt	y
	100%

Extinction coefficient - UV-VIS:

To obtain the extinction coefficient for every cyanine and solvent four different concentrated solutions are prepared and measured with the UV-3600 i Plus spectrometer from Shimadzu. The extinction is then plotted against the concentration and fitted with a linear regression. From the slope the extinction coefficient can be obtained.

Physical and Chemical Drying of Coatings with NIR Absorbers to Replace Oven Technologies

Sascha Driesen^{1*}, Nicolai Meckbach¹, Jochen S. Gutmann², and Bernd Strehmel¹

¹ Niederrhein University of Applied Sciences and Institute of Coatings and Surface Chemistry (ILOC), Adlerstraße 1, 47798 Krefeld, Germany

² Department of Physical Chemistry, Center of Nanointegration (CENIDE), University of Duisburg-Essen, 45141 Essen, Germany

*sascha.driesen@hs-niederrhein.de

Functionalized polymethine-based NIR absorbers with extinction coefficients of several $10^5 \text{ M}^{-1}\text{cm}^{-1}$ can replace older energy-wasting oven techniques by integration of photonic sources such as high-power NIR-LEDs or NIR lasers with line-shaped focus emitting between 700–1100 nm. The combination of these materials with NIR sources facilitates film formation on a glass substrate. During photonic drying, it can reach a temperature comparable to baking conditions. Compared to oven drying, the heat can be generated in the coating on DEMAND by switching the light source ON and OFF. The results of the DSC measurements showed that photonic drying results in similar glass transition temperatures and, in most cases, exhibits almost no post-polymerization indicating almost completed polymer formation. Photonic drying of coating systems offers many advantages, including energy savings of over 90% compared to oven technologies, cost savings, and waste reduction. It complements nowadays disclosed field of light-induced polymer formation.

Keywords: Photonic drying, Near-infrared, Absorber, Polymethine, Cyanine, LED, laser

1. Introduction

NIR absorbers based on functionalized polymethines possess the potential to replace older oven techniques by a photonic source namely a high-power NIR-LED or NIR-Lasers with line-shaped focus emitting between 700–1100 nm [1]. These materials facilitate conversion of absorbed light energy into heat as the main proceeding process. Therefore, combination of them with NIR sources facilitates film formation of processed coatings on a selected substrate. High power NIR-LEDs have received increased attention in the field as their use offers many advantages compared to NIR lasers [2]. This work preferably focuses on LEDs emitting at 860 nm, and 1050 nm and a NIR-Laser emitting with line-shaped focus at 980 nm. There exists a relationship between the structural pattern of the cyanine used as absorber and non-radiative deactivation as main route to generate heat. Internal conversion proceeding between the lowest vibrational mode of the excited state and a higher

vibrational mode of the ground state explains the scenario [3] (Fig. 1). Collision of such a hot molecule with matrix molecules fundamentals the main process contributing to heat generation. Generated temperature can reach several hundred Celsius degrees.

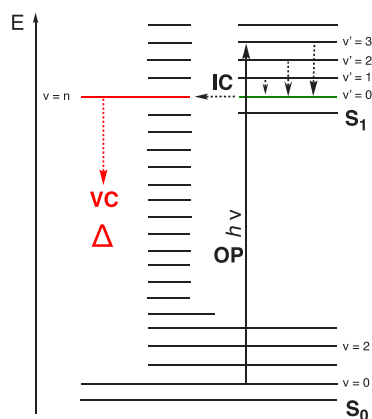


Fig. 1. Simplified Jablonski diagram for overview of photophysical processes taken from reference [4].

This technology works also well on temperature-sensitive substrates because light absorption and heat generation take place mainly in the coating with high selectivity and no significant thermal damage of the substrate. NIR absorbers comprising either benzo[c,d]- or benzo[e]indolium pattern absorb between 700-1100 nm with extinction coefficients of several $10^5 \text{ M}^{-1}\text{cm}^{-1}$ [5]. An example shows thermal initiation of a chemical reaction leading to formation of a polyurethane comprising a blocked isocyanate [6]. Temperature generated results in formation of the isocyanate $>180 \text{ }^\circ\text{C}$. This new type of photopolymerization, which may be more accurately named as photoinduced thermal polymerization, results in crosslinking.

Compatibility of the absorber, controlled by the molecular pattern of the absorber at different positions, with the matrix can be seen as a further important parameter. Aggregation should be therefore avoided because this results in a decrease of the absorption at the excitation wavelength and therefore in a loss of absorption efficiency. Photonic drying of coating systems offers the great advantage that the heat required for solidification penetrates directly to the place where it would be needed on demand [7]. This results in huge energy savings of more than 90% of the requested energy required in traditional oven technologies [8]. In addition, this technology can result in savings in cost and waste.

2. Experimental

The organic compounds of the absorbers consist of heptamethine cyanines comprising naphthostyryl (benzo[c,d]-indolium as terminal group [9]). These end groups can be introduced by alkylation or alkylarylation of benzo[c,d]indol-on (Fig. 2). The changes in the side chain can alter the chemical property of the absorber. The absorber comprises two end groups and a chain builder in the center of the molecule. The chain builder responsibly tunes the position and the maximum of the absorber in the absorption spectrum. It can exhibit a cyclohexene moiety in the center with conjugated carbons on both sides. Chlorine, phenyl, or barbiturate can stand in the center; that is the *meso*-position. The exchange of chlorine by phenyl in the *meso*-position can cause a red shift in the spectrum. Besides the benzo[c,d] compound as cation, the absorber also bears an anion as long as the net charge of the cyanine remains larger than zero. This counter-ion can be chloride, hexafluorophosphate, tetrafluoroborate or dodecylbenzenesulfonate. This part of absorber decisively determines the solubility

in the application medium. Based on this knowledge, the absorbers could be adapted for the application medium, and the light sources used for the application.

The following part discloses a general synthesis route of the absorbers. In a first reaction step, the benzo[c,d]indol-2(1H)-one reacts by heating in the presence of sodium hydroxide solution, NMP and the alkyl bromide. The mixture is then transferred to an ice/water mixture with the reaction product was obtained by extraction with toluene. The resulting yellow-orange liquid was dried with sodium sulfate and concentrated in a rotary evaporator [10].

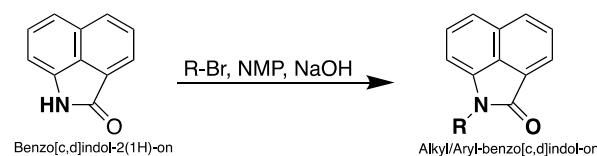


Fig. 2. Synthesis of alkyl/arylbenzo[c,d]indol-one from benzo[c,d]indol-2(1H)-one.

After alkylating/alkylarylation the benzo[c,d]indolone, the liquid reactant reacted with methyl magnesium chloride in a Grignard reaction resulting in a green alkyl/aryl benzo[c,d]indolium salt (Fig. 3). In this step, the desired anion can be introduced but later exchange by metathesis is possible either. Due to different solubilities, this process is limited and requires the understanding of salt formation reactions in organic surroundings.

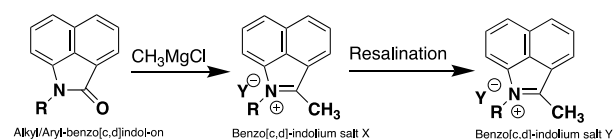


Fig. 3. Synthesis of benzo[c,d]indolium salt from alkyl/arylbenzo[c,d]indol-one followed by ion exchange reaction of the counter ion.

For the synthesis of the respective absorber, the chain builder is needed as central building block (Fig. 4). This compound is manufactured by reaction of cyclohexanone with the Vilsmeier-Haack reagent made by reaction of dimethylformamide and phosphorus oxychloride. The crude product is poured onto ice and allowed to crystallize. After crystallization the brown-yellowish raw product is washed with water [11].

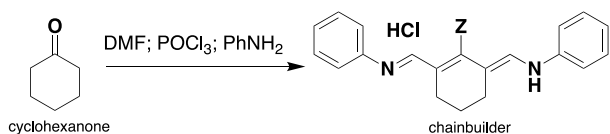


Fig. 4. Synthesis of the chain builder for the absorber synthesis starting from cyclohexanone with the Vilsmeier-Haack reagent.

After synthesis of the indolium salt and the chain-builder, formation of the absorber proceeds by reaction between them in methanol under reflux (Fig. 5). A shiny powder is obtained. Depending on the target salt, the color of the product may change from red to brown [12].

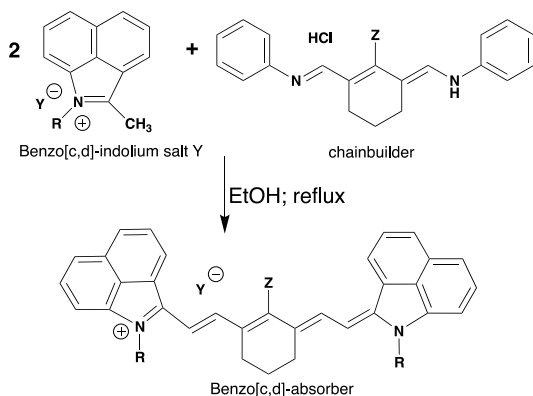


Fig. 5. General absorber synthesis based on benzo[c,d]indol-2(1H)-one and a chain builder for absorption in the near-infrared region.

After synthesis of the absorber, the counter ion can be exchanged to obtain a better solubility in the application medium. For this purpose, the absorber and the achievable anion are added in a solvent such as dichloromethane (Fig. 6). Addition of water results in phase separation. Washing of the organic phase followed by concentration of the target material results in the final absorber as shiny powder.

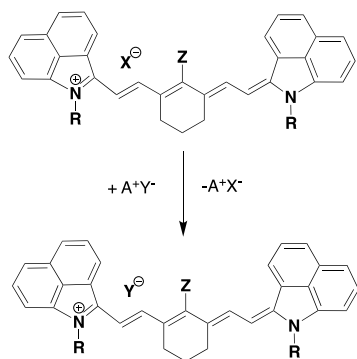


Fig. 6. General reaction equation for the exchange of the counter ion of benzo[c,d] absorbers.

The absorption spectra of the Absorbers were recorded in dichloromethane with a UV-3600i Plus UV-VIS-NIR spectrophotometer. Knowledge of the extinction coefficient connects to the solubility of the absorber in the respective medium. The solubility of the absorbers in the application medium can be seen as a major point to affect the efficiency of such systems.

Photonic drying of the coating requires overlap of the absorption spectrum of the absorber with the emission spectrum of the light source. After successful matchmaking, the samples were set up and prepared for photonic drying using the LED/Laser source. The samples were prepared by incorporating 0.5 wt% of the absorber into the coating. Formvar 2440-3500 from ELANTAS and an aqueous acrylic dispersion from ALTANA were applied as coating solutions, which typically request oven drying and curing. For the photonic drying of Formvar 2440-3500, absorber **A** (S0991 in Fig. 7) was chosen. The drying experiment used a LED and a laser with line-shaped focus emitting at 1050 nm and 980 nm, respectively. Absorber **B** (S2493 – Fig. 8) was taken for drying of the aqueous acrylic dispersion with a LED emitting at 860 nm. For comparison, samples of the coatings without absorbers were prepared as well. All samples were applied on glass substrates resulting in a wet film thickness of 90 μm . The samples without absorbers were dried in the oven at 220 $^{\circ}\text{C}$ (Formvar244-3500) and 120 $^{\circ}\text{C}$ (aqueous acrylate dispersion) for 15 minutes each.

Films dried with absorbers were exposed at different time frames (Laser irradiation 10 seconds, LED irradiation 1 minute). During irradiation, a temperature profile of the photonic drying process was recorded with a Testo-890 thermal imaging camera from Testo SE & Co. KGaA. After drying, all samples were prepared for DSC measurements. These were carried out with the DSC Q200 from TA Instruments. This tool was used to check the glass transition temperature T_g and possible post-polymerization in comparison between oven drying and photonic drying.

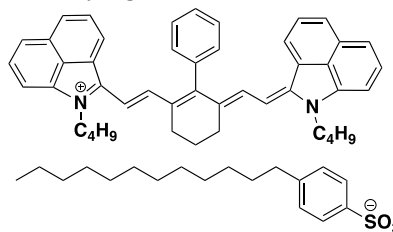


Fig. 7. Absorber A S0991 from FEWChemicals [13].

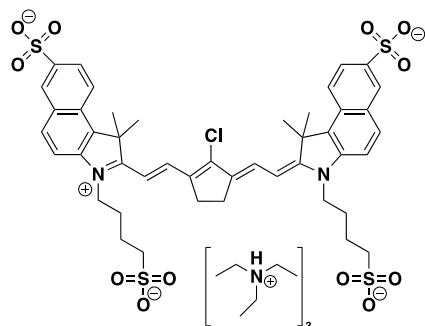


Fig. 8. Absorber **B** S 2493 from FEW Chemicals [13].

3. Results and discussion

3.1. Strategy

For a successful photonic drying of the coating, there are requirements which are necessary as the overlap of the emission spectrum of the light source with the absorption spectrum, a high extinction coefficient of the absorber, the solubility of the absorber in the coating and thus a high heat generation within the coating. These parameters require deeper consideration to optimize conditions for photonic drying.

3.2. UV/VIS/NIR-Measurements and light source compatibility

Figure 9 shows the absorption spectra of the absorbers **A** and **B** *vide infra*. **A** was measured in dichloromethane and **B** in water. The extinction coefficients relate to the absorption maximum. Absorber **A** absorbs at 1010 nanometers and appears therefore as ideal candidate to operate with the LED device emitting at 1050 nm. **B** shows its absorption maximum at 838 nm enabling the LED emitting at 838 nm. These data provide the respective extinction coefficients for **A** ($2.71 \times 10^5 \text{ M}^{-1} \text{ cm}^{-1}$) and **B** ($2.60 \times 10^5 \text{ M}^{-1} \text{ cm}^{-1}$) as shown in Table 1.

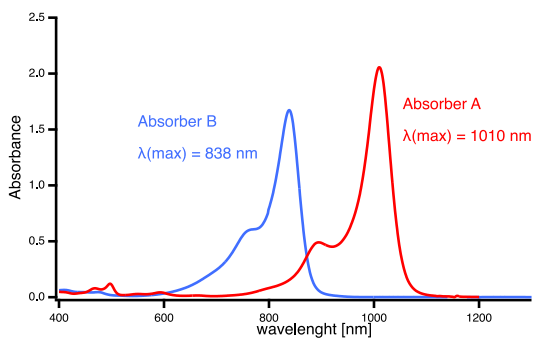


Fig. 9. Absorption spectra of absorbers **A** and **B** measured in dichloromethane and water with UV-3600i Plus UV-VIS-NIR spectrophotometer. Plot of absorbance versus wavelength in nm.

Table 1. Measured values of the absorption spectra and results of the extinction coefficients of the absorbers.

Absorber	maximum wavelength λ_{max} [nm]	solvent	Absorption coefficient ϵ ($10^5 \text{ M}^{-1} \text{ cm}^{-1}$)
A	1010	CH_2Cl_2	2,71
B	838	water	2,60

For photonic drying, the emission spectrum of the LEDs must overlap with the absorption spectrum of the absorbers. Figure 10, *vide infra*, shows such an emission spectrum of the respective LED intensity taken with an OceanOptics HR4000 spectrometer. Here, complete overlap is not mandatory to obtain an efficient system. Absorption at the edges of the absorption spectrum in the NIR facilitates deeper penetration into the sample. Thus, the photochemical reaction can also take place in deeper layers compared to the light absorbed in the absorption maximum, where it mainly enables processes nearby the surface. The irradiance of the LEDs is 2.3 W/cm^2 at 860 nm and 0.89 W/cm^2 at 1050 nm with a distance to the substrate of 0.5 cm in each case.

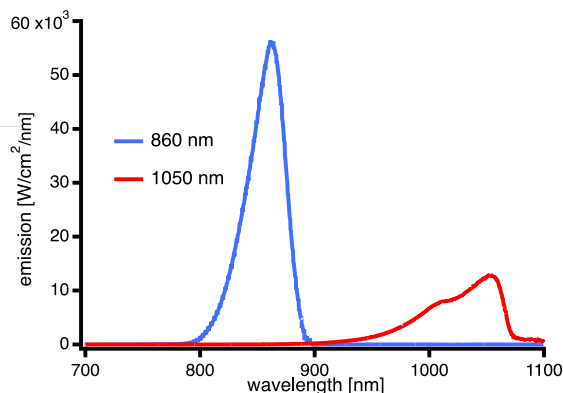


Fig. 10. Emission spectra of LEDs at 860 nm and 1050 nm from Easytec GmbH measured with spectrometer OceanOptics HR4000. Plot of emission in $\text{W/cm}^2/\text{nm}$ against wavelength in nm.

3.3. Solubility of the absorbers in the coating

In addition to the absorption of light, the solubility of the absorbers in the coating is very important. This appears crucial for a homogeneous heat distribution in the coating and prevents the occurrence of imperfections [14]. In addition to this, the maximum absolute amount of the absorber that can be dissolved in the coating also plays an important role. One approach can be that the solubility tests can be carried out in the neat solvent

that is also part of the coating. This can be water or butan-1-ol to obtain a starting point for the solubility. However, it seems more accurate to calculate this directly in the coating solution. For coatings with very high viscosity, this is usually not possible because the solid components of the absorber cannot be separated from the saturated solution. In this case, the problem can be solved by creating a regression line from diluted solutions with defined amounts of a low viscosity facilitating easier handling during spectroscopic measurements [15].

Table 2. Solubility of the absorbers in the coatings.

Absorber	dissolved in	Solubility [g/l]
A	Formvar 2440-3500	1.2
B	acrylate dispersion	0.5

As shown in Table 2, Absorber **A** possesses a solubility of 1.2 g/l in Formvar 2440-3500. This is higher than the solubility of **B** in the acrylate dispersion where a value of 0.5 g/l was taken. However, higher solubility does not necessarily result in better photonic drying performance. It simply means that more photons can be absorbed by more absorber molecules. Further tests of photonic drying, used samples containing 0.5 wt% weight percent of absorber.

3.4. Photonic drying and temperature profile

Five different samples were used to compare oven and photonic drying. The samples were applied to glass substrate with a wet film thickness of 90 μm. The oven drying temperature was set according to the baking conditions. Temperature profiles were recorded with a thermal imaging camera for photonic drying as shown in Fig. 11.

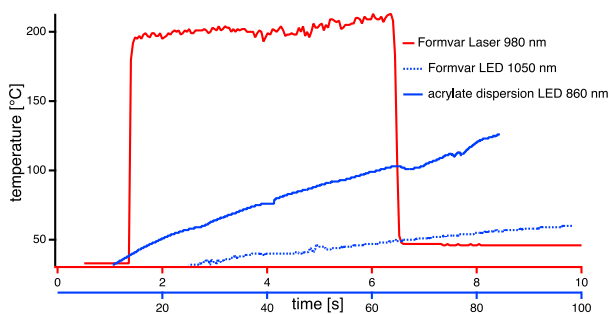


Fig. 11. Temperature profile of photonic drying of Formvar 2440-3500 with irradiation of a laser at 980 nm (300 watts) and a LED at 1050 nm (0.89 W/cm²) and of an acrylic dispersion with irradiation of an LED at 860 nm (2.3 W/cm²) using a Testo-IR 890 thermal imaging camera from TESTO.

This Figure shows the immediate temperature increase at the begin of irradiation for each sample. The recorded temperature of Formvar 2440-3500 with irradiation of the laser at 980 nm possesses a maximum temperature of 213 °C due to the high power of the laser at 300 W. This temperature is reached immediately after the laser is switched on and immediately drops to about 50 °C when the laser is switched off. It demonstrates the great advantage of this technology over conventional oven technologies. If, in comparison, the coating is then irradiated with the 1050 nm LED at an irradiance of 0.89 W/cm² in a stationary state for one minute, the temperature reaches its maximum at 60 °C. This result demonstrates that the lower intensity as provided by the high-power LED results in less heat generation compared to more intense laser exposure. In other words, the laser provides a higher number of photons that contribute to a higher amount of absorbed energy converted to heat according to the mechanistic pattern in Figure 1. Thus, sufficient drying temperature cannot be achieved in the considered frame. In comparison, the baking conditions of this coating in the oven are about 220 °C and 15 minutes.

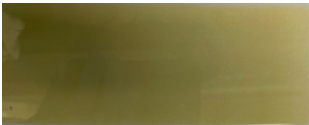
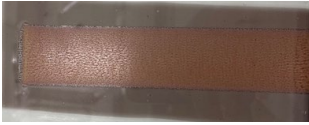



Consideration of the temperature curve of the acrylate dispersion generated with the LED at 860 nm at 2.3 W/cm² demonstrates temperature increase to a value of 126 °C after one minute of exposure. This quantity is similar compared to baking conditions at 120 °C for 15 min. As a result, combination of the respective absorber and the light source appears sufficient to obtain the required temperature for processing.

3.5. Glass transition temperature T_g and post polymerization

The glass transition temperature and the post-polymerization of the remaining monomer in the processed sample indicate whether photonic drying of the samples was successful compared to the oven drying or not. Table 3 shows the measured values of the glass transition temperatures and post-polymerizations of the samples obtained after light processing. Post-polymerization is the exothermal peak area in the first heating run of the sample (in J/g). The glass transition temperature was taken in the second heating run.

The results show that the measured values of photonic drying are comparable with oven drying. The T_g of Formvar 2440-3500 in the oven is 128 °C while photonic drying by the laser at 980 nm resulted in a T_g of 127 °C. On the other hand,

Table 3. Glass transition temperatures in °C, amount of heat in joules per gram and the appearance after drying of Formvar 2440-3500 and an acrylate dispersion.

Coating	Absorber	Type of Drying	T_g [°C]	post polymerisation [J/g]	appearance
Formvar 2440-3500	-	Oven 220 °C	128	39	
Formvar 2440-3500	A	Laser 980 nm	127	40	
Formvar 2440-3500	A	LED 1050 nm	94	151	
Acrylate dispersion	-	Oven 120 °C	73	18	
Acrylate dispersion	B	LED 860 nm	73	18	

LED induced curing at 1050 nm resulted in a glass transition of the cured sample of 94 °C. Thus, the values between oven drying and laser drying appear almost similar. The temperature curve from Fig. 11 confirms this statement. Thus, the temperature generated is sufficient to dry and crosslink the coating. In comparison between Laser and LED, the temperature, which occurs by irradiation and the intensity of the light source are too low to provide the required amount of heat for drying. This is reflected in the T_g values and post-polymerization. The T_g is much lower and the process of drying does not lead to a fully crosslinked coating. The T_g of the acrylate dispersion in the oven is 73°C and after irradiation with LED 860 nm for 1 minute it appears at 73 °C either. The temperature generated appears sufficient to dry the coating with the light source. The amount of heat at post-polymerization confirms the results.

4. Conclusion

Photonic drying of the coatings showed the feasibility to use this technology as a substitution for drying and curing in conventional ovens. This results in a huge saving of energy in production lines. Here curing of Formvar 2440-3500 with laser exhibiting line-shaped focus operated at 980 nm

resulted in similar T_g values if the sample was cured in the traditional more energy consuming oven technology or by application with the new photonic drying technique. The LED operated at 1050 nm, which is less powerful than the laser, could not achieve this result. Here, further development would be needed to optimize the output of emitted photons. This would require focusing on optimization for the alignment of optical components because there do not exist so many choices regarding the development of stronger emitting semi-conductors nowadays.

The aqueous acrylate dispersion could also be dried by the new photonic technique. Here, the combination of the absorber and the LED at 860 nm was able to generate a sufficiently high temperature, which can be seen as a big feature.

Acknowledgement

This work was supported by ZIM project KK5297501TA1.

References

1. C. Schmitz and B. Strehmel, *Farbe Lack*, **124** (2018) 40.
2. C. Schmitz and B. Strehmel, *J. Coat. Technol. Res.*, **16** (2019) 1527.

3. Q. Wang, S. Popov, A. Feilen, V. Strehmel, and B. Strehmel, *Angew. Chem., Int. Ed.*, **60** (2021) 26855.
4. A. Pigliucci and E. Vauthey, *Chimia*, **57** (2003) 200.
5. B. Strehmel, S. Ernst, K. Reiner, D. Keil, H. Lindauer, and H. Baumann, *Z. Phys. Chem.*, **228** (2014) 129.
6. U. Meier-Westhues, Polyurethane, Vincentz Network Hannover 2007, 1. Auflage.
7. C. Schmitz, Y. Pang, A. Gülz, M. Gläser, J. Horst, M. Jäger, and B. Strehmel, *Angew. Chem. Int. Ed.*, **58** (2019) 4400.
8. A. Goldschmidt, H.-J. Streitberger, *BASF Handbuch Lackiertechnik*, Vol. 1. Auflage, Vincentz Network, Hannover, 2014.
9. T. Karatsu, M. Yanai, S. Yagai, J. Mizukami, T. Urano, and A. Kitamura, *J. Photochem. Photobiol., A*, **170** (2005) 123.
10. S. Pascal, Y. Getmanenko, Y. Zhang, I. Davydenko, M. Ngo, G. Pilet, S. Redon, Y. Bretonniere, O. Maury, I. Ledoux-Rak, and S. Barlow, *Chem. Mater.*, **30** (2018) 3410.
11. G. A. Reynolds and K. H. Drexhage, *Org. Chem.*, **42** (1977) 885.
12. P. Roschger, S. Michaelis, K. Hassenrueck, H. Berneth, P. Callant, and A.-G. Bayer, *DE4331162A1*, 1995.
13. https://www.few.de/fileadmin/daten/Kataloge/FEW_FUN_Dyes_2017.pdf (accessed on 10.03.2023).
14. S. Cirak, B. Strehmel, and S. Driesen, ASTA Transmission Energy GmbH, *EP20213339*, 2021.
15. C. Schmitz, A. Halbhuber, D. Keil, and B. Strehmel, *Prog. Org. Coat.*, **100** (2016) 32.

The Design and Synthesis of New NIR-Active Sensitizers for Use in Photochemical Processes and Controlled Polymerizations

Nicolai Meckbach^{*1}, Sascha Driesen¹, Jochen S. Gutmann²,
and Bernd Strehmel¹

¹Niederrhein University of Applied Sciences,
Institute for Coatings and Surface Chemistry
Adlerstr. 1, 47798 Krefeld, Germany

²Department of Physical Chemistry, Center of Nanointegration (CENIDE),
University of Duisburg-Essen, 45141 Essen, Germany

*nicolai.meckbach@hs-niederrhein.de

The NIR-absorbers **S1-S3** derived from heptamethines covering the absorption from 700–1100 nm were used to study photopolymerization of vinyl monomers in organic and aqueous surroundings. Polymerization conditions were chosen to follow an ATRP protocol using ethyl α -bromophenylacetate (**EBPA**) as initiator in organic surroundings and ethyl-2-bromoisobutyrate in aqueous medium. Excitation proceeded at 820 nm using a new high power NIR-LED. PtBr₄, AuBr₃, and NiBr₂ served as metal catalyst to complement previous findings where CuBr₂/L and FeBr₃/Br⁻ served as metal catalysts in photo-ATRP explorations using NIR-radiation for excitation. UV-Vis-NIR titration experiments were pursued to receive more detailed information about interactions between the sensitizer (**Sens**) and the 3d-metal ion added. Except for NiBr₂, all metal salts resulted in a change of the absorption spectrum. This occurred bathochromic in case of FeBr₃ addition and hypsochromic upon addition of CuBr₂, PtBr₄, and AuBr₃.

Keywords: Cyanine, near-infrared radiation, photo-ATRP, metal catalysis

1. Introduction

Macromolecules have been part of people's everyday lives after their first disclosure for about 100 years [1]. Although work on polymer research has been going on for a century, there certainly exists demands in academia and industry to promote and develop alternative reaction routes to get access to improved environmentally friendly and more energy-efficient alternatives procedures compared to classical polymer synthesis. In particular, the synthesis of macromolecules with well-defined architectures has increasingly attracted the focus of research in university and industrial groups around the world [2]. This type of synthesis is, as so often, inspired by exploration of mechanistic aspects and naturally inspired reactions.

Photochemical strategies of material synthesis have received increased interest. This follows from the simple conclusion that light as the smallest

reagent and tool enables in chemical, technological processes and on demand. Photochemistry, here, represents as interdisciplinary discipline of material sciences and engineering to connect different fields. This offers the opportunity to work on practical problems with almost well-established methods and considers challenges to develop new photochemical methods with focus on surfaces and coating chemistry [3–5].

NIR-induced photopolymerization can be seen as one operating field used in some industrial applications such as the Computer-to-Plate (CtP) technology to name one example [6,7]. Nevertheless, the fundamentals can be considered still in its infancy [8]. Although some detailed mechanistic studies of photosensitized radical and cation formation in the visible range were disclosed [9], the spectral range of NIR absorbers, in which heptamethine cyanines operate as sensitizer (**Sens**),

has not been well understood [8]. Here, internal conversion results in efficient formation of heat. [8,10] This feature enables some of these systems with technological processes requesting a certain amount on thermal energy. Their use in photonic technologies addresses the question of further increase the efficiency in industrial applications. Here, it would be desirable to tailor the overlap of the emission of LED arrays or diode lasers with the absorption band of the sensitizer. It is therefore advantageous to organize reaction protocols following tailor-made synthesis of such absorbers. The advantages of NIR light, as already mentioned, should be exploited with the goal to tailor the absorption wavelength between 700-1100 nm with respect to the emission of the light source. Possible problems, such as interfering of UV-absorbing monomers in the case of UV-induced polymerization, are therefore excluded from the outset. Therefore, NIR-sensitized photo-ATRP developed in previous work [11-13] appears suitable as a controlled radical polymerization method to test the new absorbers synthesized regarding a possible practical application. Considering their use in paint and surface chemistry, the polymers could be used in coating materials for UV protection of substrates or in the synthesis of tailor-made polymers. Such systems may be also of interest for lithographic systems operating with NIR-excitation since controlled polymerization would diminish polymerization and therefore crosslinking in the shadow areas.

The synthesis of new NIR active sensitizers and the practical application of these NIR-sensitized photo-ATRP systems appears of highly interest. In addition, it can be seen as a practical topic regarding various aspects such as sustainability and new synthesis possibilities. First industrial applications of the synthesized systems have been already in the testing phase in other projects [4].

2. Experimental

2.1. Preparation of NIR-Absorbers

A possible general synthetic route describes manufacture of benzo[c,d]-based cyanine compounds as an example. Starting from benzo[c,d]indole-2(1H)on, which requires purification in boiling ethanol prior to use, the synthesis begins with alkylation the nitrogen. For this purpose, 0.03 mol of the crude product is introduced into N-methyl-2-pyrrolidone under inter conditions and vigorous stirring. Portions of 0.6 mol sodium hydroxide solution are added, followed by

addition of 1-bromobutane while the internal temperature should not exceed of 30°C. The next step, which is boiling, transfers the reaction solution to an ice-water mixture. A yellow-red reaction product precipitates, which is extracted in toluene. The combined toluene phases are washed with water, dried over disodium sulfate while the solvent is removed in the last step.

Following, alkylation takes place by a Grignard reaction on alkylated nitrogen in toluene. After two hours at 90 °C follows cooling to 10 °C, hydrochloric acid is carefully added to form the reaction product. This step follows addition of potassium hexafluorophosphate as slurry resulting in phase separation. After washing the organic phase with water and other organic solvents, the alkylated benzo[c,d]indolium ion is obtained.

The chain builder reacts the above product disclosed, which can be purchased or prepared by the Vilsmeier-Haack reaction [14]. Further modification can be done later in the *meso*-position, where often a chlorine substituent facilitates easy exchange with other organic nucleophilic groups.

The previously synthesized components are now linked to form a cyanine absorber. Thus, 10 mmol of the indolium salt and 5 mmol of the chain builder are heated in methanol in the presence of hydrochloric acid at 60 °C for one hour. The solvent is then removed, and dichloromethane is added to the residue. The mixture is short heated up until boiling occurs followed by hot aspiration of precipitate and washing of the filter cake. The product obtained is dried at 50°C overnight in a vacuum oven. Overall, final yields of about 50% can be expected agreeing with literature data of similar compounds.

For the synthesis of a *meso*-substituted absorber with barbiturate as the inner salt, the previous product (1 mmol) and dimethylbarbituric acid are placed in methanol under nitrogen introduction. It is stirred at 50°C for three hours under reflux. The product thus obtained is purified through a column of basic alumina, using chloroform as eluent. Unwanted fractions, such as by-products, remain on the column. During purification, the obtained fractions are continuously analyzed and characterized by UV/VIS/NIR spectroscopy.

2.2. Controlled Photopolymerization

A Schlenk reaction vessel equipped with a magnetic stirrer and Teflon screw cap septum was filled with 0.045 mM Sens, 0.04 mM PtBr₄ in DMF, and 0.1 mM TBABr (ligand L) in DMF. To this

mixture, monomer (45 mmol), DMF and ethyl- α -bromophenyl acetate, **EBPA** (0.150 mmol), were added and the solution was homogenized by stirring. The solution was degassed almost completely by four freeze-pump-thaw cycles and brought under nitrogen atmosphere. The reaction mixture was placed in a photoreactor irradiated at the desired wavelength (NIR LED irradiation at 790 nm) applying an intensity of 0.1 W/cm². At the end of exposure, the resulting polymers were precipitated in cold methanol and then dried under reduced pressure. Conversion was determined gravimetrically.

2.3. UV-Vis-NIR Titrations

In general, UV VIS NIR titrations are used to observe and graphically display the change of absorption bands upon addition of other substances. In this case, change of absorbance of the sensitizer in solution upon stepwise addition of metal halides was observed and graphically evaluated. The changes observed relate to formation of new absorption bands while that of the substrate decreases.

Two stock solutions are prepared. The first solution consists of the sensitizer (**Sens**, 3.665 mg S2265) in the solvent intended to be used in the subsequent polymerization (DMF, 100 mL). The second stock solution comprises of the transition metal halide (PtBr₄ 11.3 mg) in the same solvent as solution **1** (DMF, 6 mL). As a reference and zero sample, 2.5 mL is then added to a cuvette and a first absorption spectrum in the range of 400 to 1400 nm is recorded. Solution **2** is then added in 10 μ L steps while the spectrum is recorded in each case. The subsequent graphical representation of all measured spectra produces a representation comparable with that of Fig. 1.

2.4. Electrochemical Experiments

The redox potentials of the absorbers were determined by measuring cyclic voltammetry. For this purpose, a three-electrode setup with platinum plates as working or auxiliary electrodes and Ag/AgCl electrode as reference was used. For the internal standard, a conducting solution was prepared beforehand. This consisted of a 0.1 M solution of NBu₄PF₆ dissolved in acetonitrile. From this, a solution of ferrocene and the stock solution at a concentration of 10⁻³ mol/L was generated.

The absorbers were diluted to the same concentration. Changes of the current were measured by first increase and then a decrease of the

potential. If electrochemical reactions took place during this course, this resulted in a change in the current intensity. The oxidation/reduction potential could be determined by reading the high/low point.

3. Results and discussion

Formation of a new absorption band appeared upon addition of 3d-metal ions to the NIR-absorber comprising a barbiturate group. Here, the new absorber shown in Fig. 1 shows a decrease of its absorption while a new bathochromic shifted absorption appeared. Complexation between the NIR-absorber and the metal ion added caused such spectral changes. Such reactions would not proceed as unusual and were almost described in the 1930's as the ZWICKER-reaction. This result confirms previous studies using a barbiturate comprising sensitizer with different indolium end groups [10]. Fig. 1 shows the intersection of both lines corresponding to a ratio of [**Sens**]:[Cu²⁺]= 1:2 agreeing well with previous findings where the respective benzo[e]indolium derivative (see Fig. 2 *vide infra*) was studied [4,12]. It should be emphasized that in case of the latter, both the band of the substrate and the new band formed in the reaction between absorber and metal ion, exhibited photoreactivity. This was demonstrated by the proceeding controlled photopolymerization with NIR-excitation. [12] Nevertheless, the sensitizer shown in Fig. 1 did not show any activity in controlled polymerization in this work. As result, change of the benzindolium pattern from benz[e]indolium to benz[c,d]indolium mainly caused this result although the number of π -electrons did not change. One reason can be the higher oxidation potential of 0.71 V and the lower excitation energy (1016 nm). Here, the free reaction enthalpy of the photoinduced electron transfer ΔG_{e1} would not be any more negative and therefore requires more activation energy compared to the sensitizer comprising benzo[e]indolium groups, see Fig. 2 *vide infra* for the structural pattern. For, comparison, this compound possesses an oxidation potential of 0.4 V [8] while absorption proceeds at 790 nm. Nevertheless, the fact that new absorption above 1100 nm appears can be seen as an important result because this can connect alternative applications using such sensitizers shown in Fig. 1.

Addition of copper(II) ions results in a hypsochromic shifted new absorption band as shown in Fig. 2. This was demonstrated by titration of the respective NIR-sensitizer where gradual amounts of Cu²⁺ was added. The spectral changes

observed in the experiment do not appear as so significant as shown in Fig. 1. Nevertheless, a rough estimate would lead to the conclusion that a 1:1 complex formation between sensitizer may explain the changes observed.

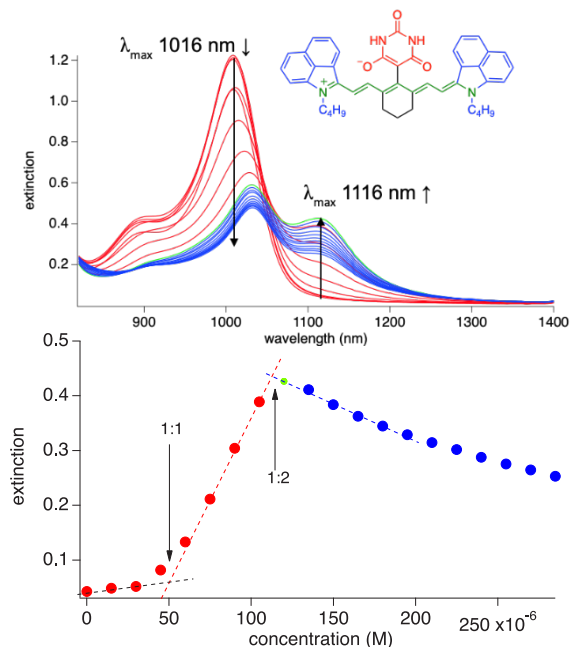


Fig. 1. Addition of $\text{FeBr}_3/\text{Br}^-$ and Sens ($c = 5 \times 10^{-5}$ M) in DMF: The inset shows the change of the OD at 1116 nm ($[\text{FeBr}_3]:[\text{L}] = 1:1 // 1:2$) but no response in photo-ATRP experiment.

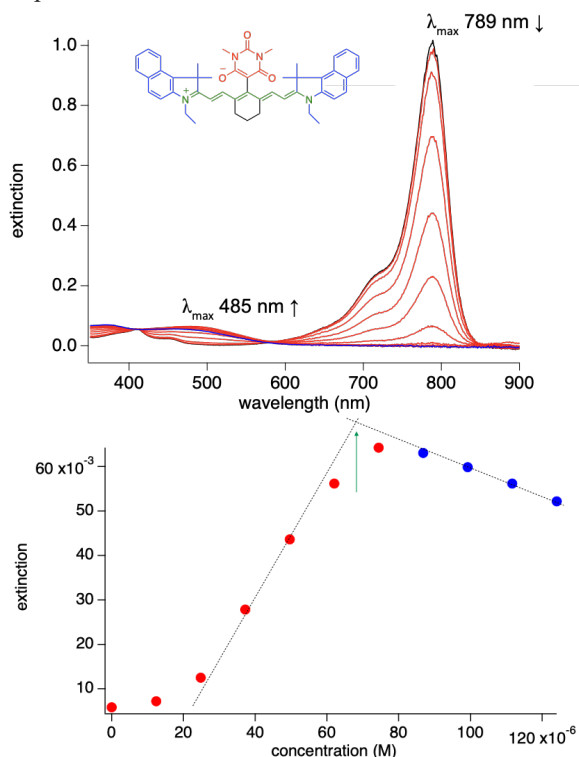


Fig. 2. Addition of $\text{CuBr}_2/\text{Br}^-$ and Sens ($c = 5 \times 10^{-5}$ M) in DMF: The inset shows the change of the OD at 485 nm while complex formation. Repeated experiment from ref. [8].

In this work, further 3d-metal ion bromides were investigated. These complementary relate to platinum, gold, and nickel ions. They were explored in water and organic media. Fig. 3 shows the results obtained using PtBr_4 in the titration experiment. Here, also a new hypsochromic shifted absorption band appeared demonstrating complexation between the barbiturate comprising sensitizer and the metal ion added. Spectra meet in the isosbestic point at 678 nm showing the existence of two participating species in the photochemical event.

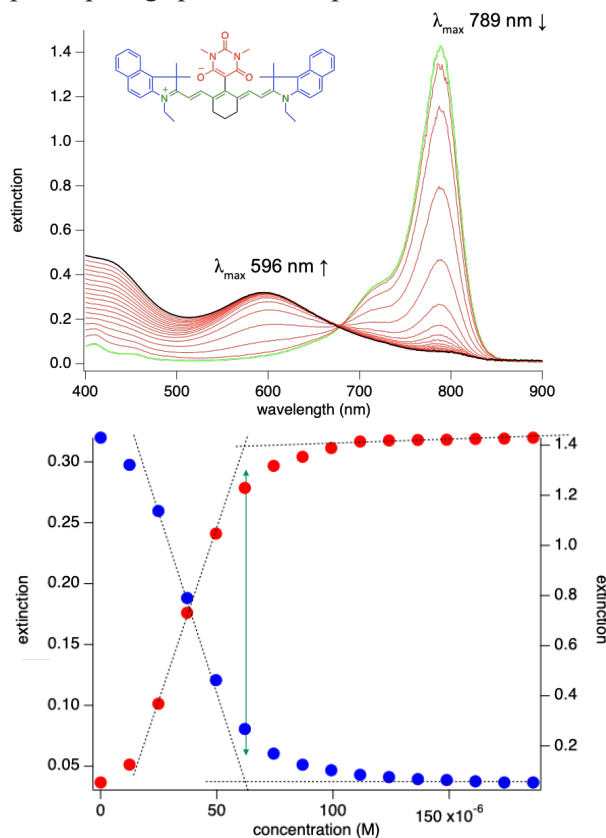


Fig. 3. Addition of $\text{PtBr}_4/\text{Br}^-$ and Sens ($c = 5 \times 10^{-5}$ M) in DMF: The inset shows the change of the OD at 596 nm while complex formation. Due to complex formation: Successful NIR sensitized photo-ATRP.

The formation of a new band after adding of PtBr_4 brings this system to more attention regarding the use in controlled radical polymerization experiments using NIR radiation. Ethyl(α -bromophenyl) acetate (**EBPA**) operated as initiator while the sensitizer used in in the experiment shown in Fig. 4 absorbed the NIR-radiation released by a high-power NIR LED at 820 nm.

Fig. 4 and Table 1 summarize the results obtained with the combination **Sens/EBPA/PtBr₄**. Average number molecular weight M_n results in high values above 80 kDa. Prolonged exposure shows growth of M_n which appears more typical for controlled polymerization conditions. Furthermore, the

dispersity of molecular weight D (M_w/M_n) starts slightly above 1.6 and shows a decrease with extended irradiation time. Chain extension experiments with the monomer methyl methacrylate were successful demonstrating the control of polymer growth.

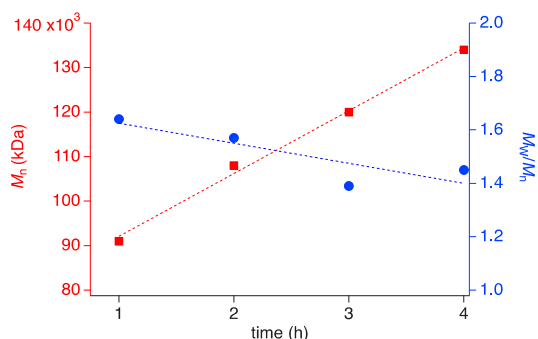


Fig. 4. Kinetic plot of the polymerization system using Sens and molecular weight characteristics and dispersity of PMMA vs irradiation time. $[MMA]_0/[EBPA]_0/[Pt^{II}Br_4]_0/[TBABr]/[Sens] = (300/1/0.02/0.0025/0.3)$.

Table 1. Results of photo-ATRP experiments: Two competing mechanisms. (Polymerization time: 2h, $[MMA]_0/[EBPA]_0/[Sens] = (300/1/0.3)$).

run	$[PtBr_4]/[L]$	conv. (%)	M_n (kDa)	M_w/M_n
A	0.04/0.01	9.7	118	1.9
B	0.04/0.005	4.7	128	2.0
C	0.04/0.02	4.7	147	2.0
D	0.02/0.01	5.3	141	1.9
E	0.08/0.01	18.2	65	2.0
F	0.0/0.01	0	0	-
G	0.02/0.0025	24.4	108	1.5

The metal catalyst concentration also importantly affects M_n . The higher the metal catalyst concentration, the lower M_n . Here, the metal catalyst, which complexes as shown in Fig. 3 with **Sens**, pushes the system to work according to a controlled polymerization mechanism. The metal-free experiment (run F) failed under the conditions chosen in Table 1. This shows that the metal catalyst is required to run the polymerization procedure.

Free radical polymerization typically competitively can occur resulting in larger dispersity. Nevertheless, the fact that no polymer was formed in case of run F gives the impression that the heavy metal ion takes some more responsibility to control growth of polymer. More investigations would be required to receive respective answers. This may include stability of

radical pairs and the role of triplet states formed by the presence of heavy metal atoms. Typically, the sensitizer used in these experiments bases on singlet chemistry.

Additional experiments focused on aqueous systems. Here, $AuBr_3$ operated as metal salt. Fig. 5 and 6 show the spectral changes proceeding upon addition of the sensitizer shown in these slides. This compound dissolves well in water and enables therefore controlled photopolymerization in aqueous medium. This could be of importance to make hydrogels.

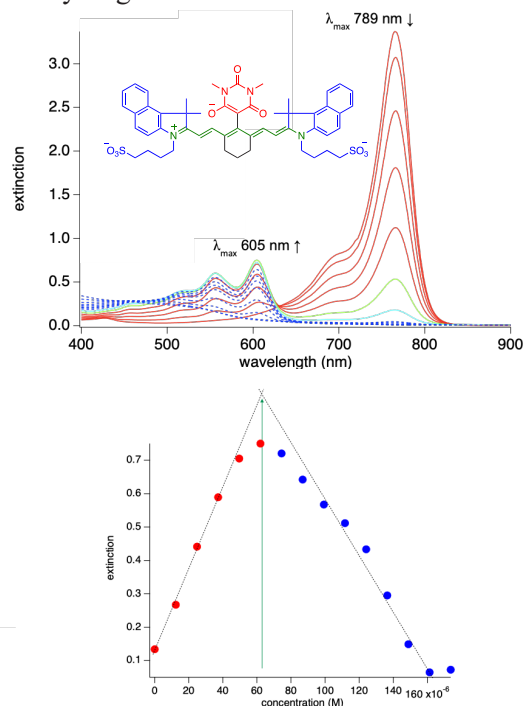


Fig. 5. Addition of $AuBr_3/Br$ ($c = 5 \times 10^{-5}$ M) and Sens in Water: The inset shows the change of the OD at 605 nm due to complex formation. Access possible to water based, NIR sensitized photo-ATRP with the possibility of the synthesis of hydrogels assuming the right monomers.

Titration curves show a decrease of the absorption band at 790 nm and formation of a new band at 605 nm. This is consistent with the experiment shown in Fig. 5 for lower concentrations of metal ion. Increase of metal ion concentration results in a decrease of the absorption at 605 nm and additional formation of new absorption in the blue/UV range. Polymerization experiments with water compatible monomers are in progress. The results will be reported elsewhere.

Further studies used $NiBr_2$ in titration experiments. Data shown in Fig. 6 show no spectral changes in the absorption spectra. Polymerization experiments showed no formation of polymer.

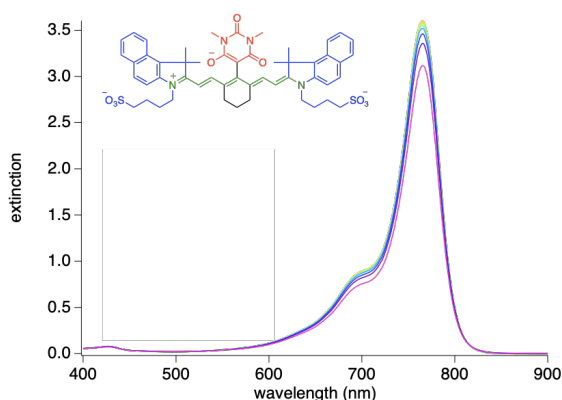


Fig. 6. Addition of NiBr_2/Br ($c = 5 \times 10^{-5} \text{ M}$) and **Sens** in Water. No new absorption band due to no complex formation. Unsuccessful activation of NIR sensitized photo-ATRP protocol

4. Summary

Consideration of controlled living polymerization techniques brings in front the advantages of ATRP as a powerful strategy for the target to synthesize tailor-made polymers. A major disadvantage is the requirement of a transition metal complex as catalyst which must have two stable oxidation states with no formation of metal oxides [15]. A successfully developed and applied strategy is the in-situ formation of transition metal complexes by photochemical reduction using photosensitizers.

Essential for these photopolymerization processes are the NIR sensitizers, which base on heptamethine dyes absorbing in the range of 700 to 1300 nm. In our work, successful synthesis of different absorbers based on benzo[c,d]indol-2(1H)-one or benzo[e]indol-2(1H)-one was. The solubility was influenced by functionalization so that compatibility in organic media or aqueous environment is possible for both cases. The absorption maxima of these organic sensitizers depend on the chain building agent needed throughout the synthesis process. It can be also influenced by functionalization. We also showed recently that there is the possibility of bathochromic shift by addition of metal ions/ligands [12]. This brings the access to new NIR light sources and the possibility to synthesize these sensitizers on demand and adapt them to an appropriate light source.

Another application of the synthesized sensitizers or absorbers can be seen to use them for photonic drying of coatings [3-5]. Here, very high extinction coefficients of these substances enable targeted drying. The NIR absorbing heptamethine dyes with the end groups benzo[c,d]- or benzo[e]-indolenes

have high extinction coefficients of several 100,000 $\text{M}^{-1}\text{cm}^{-1}$ and lead to high heat generation in combination with the right choice of an energy saving source light source; that is a high intensity NIR-LED or a laser with line-shaped focus.

Acknowledgement

Authors from Niederrhein University of Applied Sciences gratefully acknowledge the Federal Ministry of Economics and Climate Protection within the ZIM project KK5297501TA1.

References

1. R. Mülhaupt, *Angew. Chem. Int. Ed.*, **43** (2004) 1054.
2. S. Dadashi-Silab, *Chem. Rev.*, **116** (2016) 10212.
3. S. Cirak, B. Strehmel, and S. Driesen, WO2022123014 (2022).
4. B. Strehmel, V. Strehmel, C. Kütahya, and N. Meckbach, WO2022136292 (2022).
5. L. Appelhoff, Q. Wang, and B. Strehmel, WO2022200192 (2022).
6. B. Strehmel, S. Ernst, K. Reiner, D. Keil, H. Lindauer, and H. Baumann, *Z. Phys. Chem.*, **228** (2014) 129.
7. T. Brömme, C. Schmitz, D. Oprych, A. Wenda, V. Strehmel, M. Grabolle, U. Resch-Genger, S. Ernst, K. Reiner, D. Keil, P. Lüs, H. Baumann, and B. Strehmel, *Chem. Eng. Technol.*, **39** (2016) 13.
8. B. Strehmel, C. Schmitz, C. Kütahya, Y. Pang, A. Drewitz, and H. Mustroph, *Beilstein J. Org. Chem.*, **16** (2020) 415.
9. J. P. Fouassier and J. Lalevée, *Photoinitiators for Polymer Synthesis*, Wiley-VCH, Weinheim, 2012.
10. Q. Wang, S. Popov, A. Feilen, V. Strehmel, and B. Strehmel, *Angew. Chem., Int. Ed.*, **60** (2021) 26855.
11. Kütahya, N. Meckbach, V. Strehmel, J. S. Gutmann, and B. Strehmel, *Chem. Eur. J.*, **26** (2020) 10444.
12. C. Kütahya, N. Meckbach, V. Strehmel, and B. Strehmel, *J. Polym. Sci.*, **59** (2021) 2023.
13. C. Kütahya, C. Schmitz, V. Strehmel, Y. Yagci, and B. Strehmel, *Angew. Chem., Int. Ed.*, **57** (2018) 7898.
14. G. A. Reynolds and K. H. Drexhage, *J. Org. Chem.*, **42** (1977) 885.
15. S. Dworakowska, F. Lorandi, A. Gorczynski, and K. Matyjaszewski, *Adv. Sci.*, (2022) e2106076.

High Resolution and Low Stress Photo-Definable Polyimide

Tomoki Sakai^{1*}, Yumiko Okuda¹, Keigo Kato¹,
Kazuyuki Matsumura¹, and Hitoshi Araki¹

¹ *Department of Electronic & Imaging Materials Res. Labs., Toray Industries Inc.,
1-2, Sonoyama 3-Chome, Otsu, Shiga 520-0842, Japan*

**tomoki.sakai.e3@mail.toray*

Recently, realization of 5G communication systems attract much attention, and high functionality and miniaturizations of semi-conductor devices and electronic devices are required. For these purposes, the polyimides applied as interlayer dielectrics of these devices are expected to show high resolution and reliability in thick films. In this paper, we worked on developing high resolution and low stress negative tone photo-definable polyimide. By combining with high light transmittance polyimide and the UV cure system that suppress active species, we successfully obtained the fine patterns with high resolution even at 40 μm thickness. We also employed the thermal cure system with no cure shrinkage, so that the residual stress was still low even at dry conditions. Our developed polyimide also showed a good insulation reliability by biased HAST (High Accelerated Stress Test).

Keywords: Photo-definable Polyimide, High resolution, Low stress, Patterning, Low shrinkage, Low temperature cure

1. Introduction

Recently, the arrival of 5G era is expected to realize the high-speed, large-capacity and low latency communication [1-5]. 5G will expand the possibilities of various services such as self-driving cars, AR/VR gaming and smart home. To spread 5G technology, there is an increasing demand for higher functionality, higher frequency and miniaturization of semi-conductor devices or electronic devices.

For its excellent heat stability, electrical and mechanical properties, polyimide is widely used as a surface protective layer, interlayer dielectrics of semi-conductor devices or electronic devices [6-10]. For miniaturization of these devices, polyimide is required to obtain suitable thick pattern. Negative tone photo-definable polyimide (NGPI) was suitable for obtaining highly reliable thick film. However, NGPI was difficult to obtain fine pattern in thick film. In addition, the thick film on the silicon substrates had a problem of increased warpage.

In this paper, we developed high resolution and low stress negative tone photo-definable polyimide.

In order to obtain high resolution NGPI, we focused on light transmittance and diffusion of active species. When the diffusion of active species is reduced, the contrast between the exposed and unexposed area is increased. High light transmittance allows uniform exposure to the bottom of the pattern of NGPI. Furthermore, we developed a thermal cure system with no cure shrinkage to reduce warpage.

2. Experimental Section

2.1. Preparation of polyimides

Polyimide resins were synthesized by polycondensation of tetracarboxylic dianhydrides with diamines. The prescribed amount of diamines was poured into a 4 neck flask with a mechanical stirrer, a thermometer and an inlet pipe for nitrogen flow. Solvent was added into the 4 neck flask. Under nitrogen flow, the flask was heated to 60 °C. The prescribed amount of tetracarboxylic dianhydrides was added into the flask with solvent. The mixture in the flask was stirred for 1hr at 60 °C, followed by polycondensation was performed for 4 hours at 180 °C.

2.2. Preparation of polyimide solution

A Polyimide solution was obtained by following procedure. 10 g of polyimide was dissolved by solvent to prepare polyimide solution at concentration of 35 wt%. Then, 10~40 wt% crosslinker and 1~10 wt% photoinitiator were added to those solution. The solution was filtered through a 1.0 μm pore poly(tetrafluoro-ethylene) filter to remove the particles.

2.3. Transmittance measurement

The varnish sample was coated at about 10 μm thickness on glass by spin coating. Coated glass was pre-baked by hot plate. The pre-baked glass was exposed to 2000 mJ/cm² without photomask, then the exposed glass was post-baked by hot plate. The post-baked glass was cured in a clean oven (CLH-21CD (V)-S, KOYO THERMOSYSTEMS Co., Ltd) at a condition of 200 °C for 1 hour under N₂ atmosphere. The polyimide film on glass was measured by double beam spectrophotometer (U-2910, Hitachi High-Tech).

2.4. Patterning process

The varnish sample was coated on an 8-in Si wafer by a spin-coater (ACT-8, Tokyo-Electron). Then, the coated wafer was pre-baked on a hot plate (ACT-8). The film was exposed from 200 mJ cm⁻² to 500 mJ cm⁻² UV. After exposed wafer was post-baked on a hot plate, post-baked wafer was developed by 2.38% tetramethylammonium hydroxide aqueous solution (TMAHaq) at 23 °C. Finally, the PSPI patterned on wafer was cured under N₂ flow at 200 °C for 1 hour.

2.5. Measurement of residual stress

10 μm thick polyimide film was obtained on 6-in Si wafer. The film stress was calculated based on the change in radius of curvature of the wafer, using thin film stress measurement system (FLX3300-T, Toho Technology). First, the film stress was measured at a condition of 23 °C to 45%RH. Then, the film was dried by purging with nitrogen for 30 min at 2 L/min to 5 L/min and the dry film stress was measured under a dry condition at 23 °C.

2.6. Reliability tests

As shown in Fig 1., the polyimide solution was coated at 10 μm thickness on TEG substrate removed organic contaminants by plasma cleaning. The line & space, pitch and height of copper were 15 μm & 10 μm, 25 μm and 5.5 μm, respectively. Then biased HAST was carried out at 130 °C for 100 hours with 3.5 V in 85 %RH.

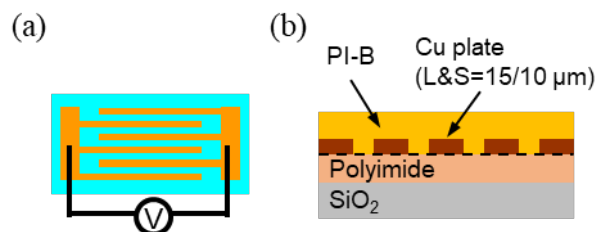


Fig. 1. (a) Top of view of test vehicle. (b) Cross section of test vehicle.

3. Results & Discussion

3.1. Light Transmittance and Patterning Formation of NGPI

We prepared negative tone photo-definable polyimide varnish samples in Table 1. PI-A and PI-B contained different polyimides, cross linkers and photo initiators. In order to obtain high resolution, we assumed that light transmittance and diffusion of active species were important. These approaches were expected to increase the contrast between the exposed and unexposed area and the exposure uniformity from the top to bottom of the pattern. We designed monomer molecule of polyimide (P2) in order to increase the light transmittance below 400 nm by suppressing the intra- and inter-polymer chain interaction based on charge transfer complex of the polyimide. Diffusion of active species of photo initiator into non-exposure area is one of the cause of lower resolution in general. We applied a UV cure system that the diffusion of active species was controlled to PI-B for high resolution.

First, we observed the light transmittance of NGPIs. Fig. 2 shows the light transmittance of NGPIs at 10 μm thickness. The transmittance at 365 nm of PI-A, which is a conventional NGPI, was 50%. On the other hand, that of newly developed PI-

Table 1. The compositions of NGPIs prepared in this work.

	Composition		
	Base polyimide	Cross linker	Photo initiator
PI-A	P1	M1	I1
PI-B	P2 (High light transmittance)	M2	I2

B was over 90%. Thus, we could obtain a high light transmittance NGPI.

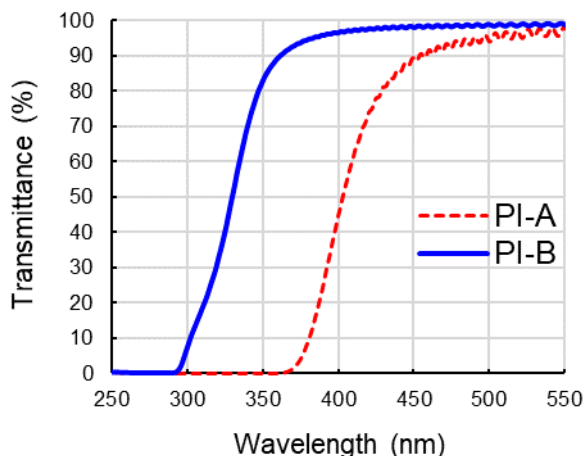


Fig. 2. The light transmittance of NGPIs at 10 μm thickness.

Next, we observed the pattern shape of NGPIs. Fig. 3 shows cross-section SEM images of patterned polyimide after cure. In case of PI-A, we could obtain patterned polyimide at 17 μm thickness on the silicon substrate and the minimum size of patterned width which we could obtain was 36 μm (aspect ratio: 0.5). On the other hand, in the case of PI-B, we could obtain patterned polyimide at 26 μm thickness on the silicon substrate and the minimum size of patterned width which we could obtain was 10 μm (aspect ratio: 2.5). Moreover, 40 μm thick PI-B could be patterned 20 μm width.

3.2. Residual stress measurement

We measured the residual stress of NGPIs by thin film stress measurement system. Fig. 4 shows the residual stress of NGPIs at 10 μm thickness. The residual stress of PI-A was 25 MPa at 23 °C to 45%RH. However, when the film was dried by purging with nitrogen, the stress was up to 35 MPa under dry conditions. These stress changes associated with drying were attributed to the water absorption properties of NGPIs. On the other hand, the stress of PI-B was 14 MPa at 23 °C to 45%RH, and the stress was up to 25 MPa when dried. In comparison with a conventional PI-A, PI-B was lower stress polyimide even in dry conditions.

The thermal cure system of PI-B could reduce cure shrinkage Fig. 5 shows the relationship between spin rotation speed of PI-B and film thickness after PB, development, and curing. We observed no thickness change even after development and cure. As PI-B had the advantage of no shrinkage, the residual stress became lower.

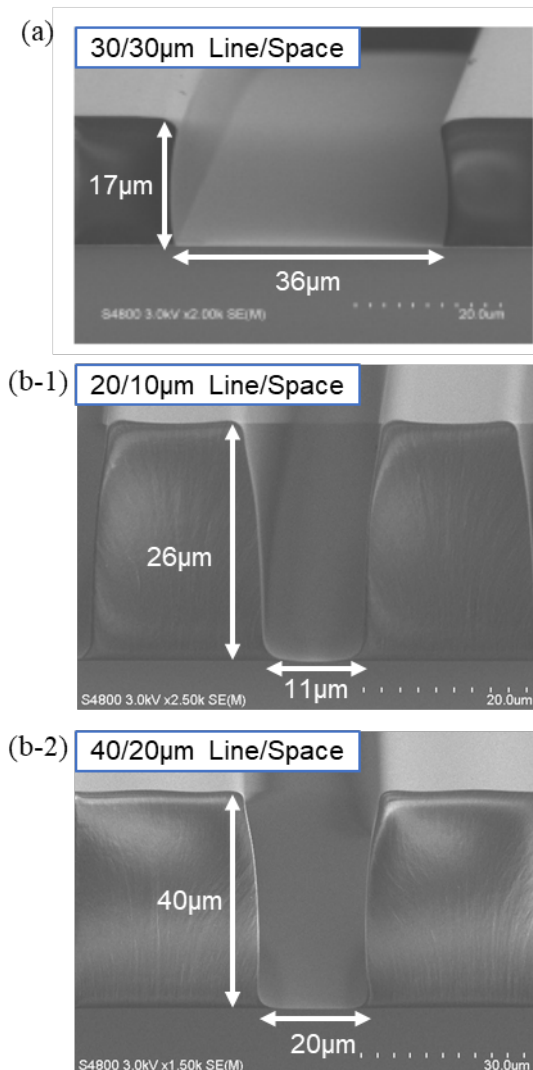


Fig. 3. Cross-section SEM images of patterned NGPIs. (a) PI-A (L/S width: 30/30 μm), (b) PI-B (L/S width: 20/10 μm or 40/20 μm).

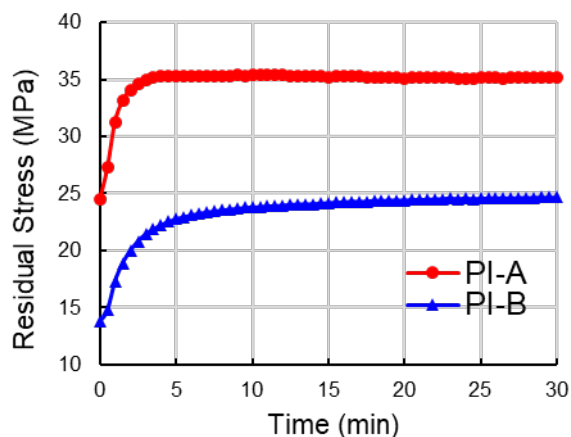


Fig. 4. Residual stress measurement of NGPIs at 23 °C to 45%RH while purging with dry nitrogen gas.

3.3. Reliability test results of PI-A

PI-B showed a good insulation reliability by biased HAST. As shown in Fig. 6, no short and open failure were observed at 130 °C for 100 hours with 3.5 V in 85 %RH.

This result indicated that PI-B have enough insulating performance as interlayer dielectrics even after the reliability test.

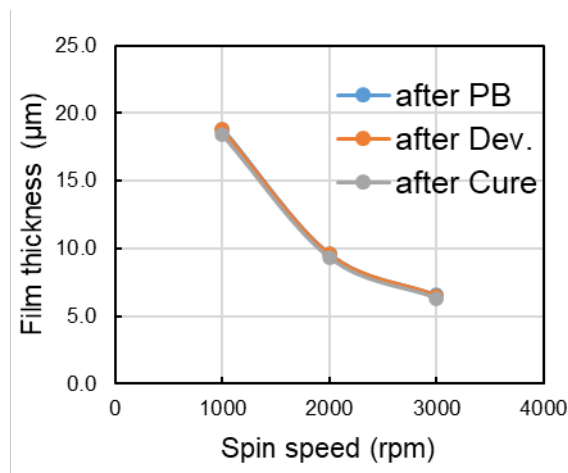


Fig. 5. Spin-curve of PI-B after pre-bake, development or cure.

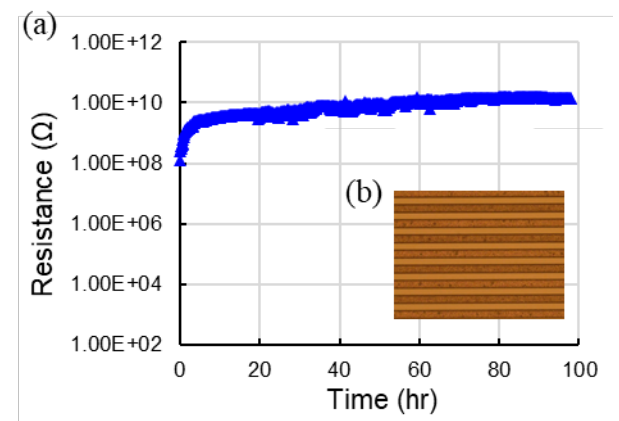


Fig. 6. (a) Resistivity of PI-B cured at 200 °C for 1 hr during the treatment at a condition of 130 °C, 85 RH%, and 3.5 V bias for 100 hrs. (b) Image of test vehicle after biased HAST test.

4. Conclusion

In this study, we combined two composition designs to develop high resolution NGPI. One was the synthesis of high light transmittance polyimide by designing monomer molecule to obtain high light transmittance NGPI. The other was the application of the UV cure system that inhibited the diffusion of active species. As a results, whereas the aspect ratio of conventional PI-A was 0.5 at 17 µm thickness, the aspect ratio of newly developed PI-B was 2.5 at 26 µm thickness and 2.0 at 40 µm thickness. In addition, we also employed the thermal cure system with no cure shrinkage. In consequence, the residual stress of PI-B became lower, and even under dry conditions was lower than that of PI-A to 45%RH. PI-B also showed a good insulation reliability by biased HAST.

Our novel high resolution and low stress polyimide are suitable for semi-conductor devices or electronic devices whose applications are 5G communication.

5. References

- [1] Y. Kishiyama, A. Benjebbour, S. Nagata, Y. Okumura, and T. Nakamura, *NTT Docomo Tech. J.*, **23_4** (2014) 6.
- [2] K. Shafique, B. A. Khawaja, F. Sabir, S. Qazi, and M. Mustaqim, *IEEE Access*, **8** (2020) 23022.
- [3] Y. Kishiyama, S. Suyama, and S. Nagata, *NTT Docomo Tech. J.*, **29_2** (2021) 6.
- [4] R. Dangi, P. Lalwani, G. Choudhary, I. You, and G. Pau, *Sensors*, **22** (2022) 26.
- [5] G. Ramesh, J. Logeshwaran, V. Aravindarajan, and F. Thachil, *ICTACT Journal on Microelectronics*, **8_2** (2022) 1338.
- [6] J. H. Kim, *J. Photopolym. Sci. & Technol.*, **22** (2009) 403.
- [7] M. Tomikawa, R. Okuda, H. Ohnishi, *J. Photopolym. Sci. & Technol.*, **28** (2015) 73.
- [8] T. Sasaki, *J. Photopolym. Sci. & Technol.* **29_3** (2016) 379.
- [9] T. Enomoto, S. Abe, D. Matsukawa, T. Nakamura, N. Yamazaki, N. Saito, M. Ohe, and T. Motobe, *2017 Int. Conf. Electron. Packag.*, (2017) 498.
- [10] M.-C. Fu, T. Higashihara, M. Ueda, *Polym. J.*, **50** (2018) 57.

Structure Characterization of Polymer Nano-Film on the Difference of Lattice Point Compounds

Shin-ichi Kondo^{1*}, Kazuma Yoshimura¹, Naoki Doi¹, Yasushi Sasai²,
Yukinori Yamauchi³, and Masayuki Kuzuya¹

¹ Laboratory of Pharmaceutical Physical Chemistry, Gifu Pharmaceutical University, 1-25-4 Daigaku-Nishi, Gifu 501-1196, Japan

² Faculty of Pharmacy, Gifu University of Medical Science, 4-3-3 Nijigaoka, Kani-shi, Gifu 509-0293, Japan

³ Department of Pharmaceutical Physical Chemistry, College of Pharmaceutical Sciences, Matsuyama University, 4-2 Bunkyo-cho, Matsuyama, Ehime 790-8578, Japan
*skondo@gifu-pu.ac.jp

In this paper we studied on the size and morphology of polymer nano-film synthesized with the new lattice point compound (LP1), comparing with the polymer nano-film of per-6-amino- β -cyclodextrin (Per-6-ABCD) used as the lattice point. It was also shown that the particle diameters of polymer nano-film composed of LP1 were larger than those of Per-6-ABCD. It was assumed that larger particle size of LP1 polymer nano-film might ascribe to the more flexible side chain and that the bulky and rigid structure of Per-6-ABCD might restrict the crosslinking reaction due to the steric hindrance. The AFM images suggested that the polymer nano-film in methanol might be expanded like a sheet and that in water the hydrophobic moiety might be turned inward to form a spherical or rod-like shape.

Keywords: Polymer nano-film, Lattice point compound, Particle size, Morphology, Self-assembled phospholipid layer

1. Introduction

The nano-film is a new type of material that possesses a two-dimensional polymeric structure with nano-meter thickness. Many of nano-film needs the supporting material [1-5]. Recently, free standing nano-films fabricated from molecular, atomic, and ionic components have been extensively investigated for systems with analytical and biomedical applications, such as separation matrices and drug delivery carriers [6-11].

On the other hand, we have developed the method to introduce a durable surface wettability on several hydrophobic polymers by plasma-assisted method [12-16], and to fabricate a self-assembled phospholipid (phosphatidyl choline (PC)) layer containing stearic acid (StA) (LDPE-StA-PC-SA) on it [17]. It was confirmed that LDPE-StA-PC-SA possessed fluidity resembling to cellular membrane. In recent years we have developed the polymer nano-film possessing hydrophilic and hydrophobic surface by using LDPE-PC-SA (Fig. 1).

As shown in Fig. 1, polymer nano-film synthesized in this way would be a 2-dimensional network polymer composing of lattice point and liker moiety. As the lattice points would also bind stearic acid, this area forms a hydrophobic surface. The morphology of polymer nano-film in organic solvents (methanol and chloroform) and water was estimated by ¹H-NMR spectra measurement and atomic force microscope (AFM) measurement [18-21].

In this paper we studied on the size and morphology of polymer nano-film synthesized with the new lattice point compound (LP1) shown in Fig. 2, comparing with the polymer nano-film of Per-6-amino- β -cyclodextrin (Per-6-ABCD) used as the lattice point reported in the previous paper [21]. We selected three kinds of linker shown in Fig. 3, succinic acid, glutaric acid and azelaic acid. The particle size and distribution of polymer nano-film in phosphate buffer solution (PBS) and methanol was estimated by dynamic light scattering (DLS).

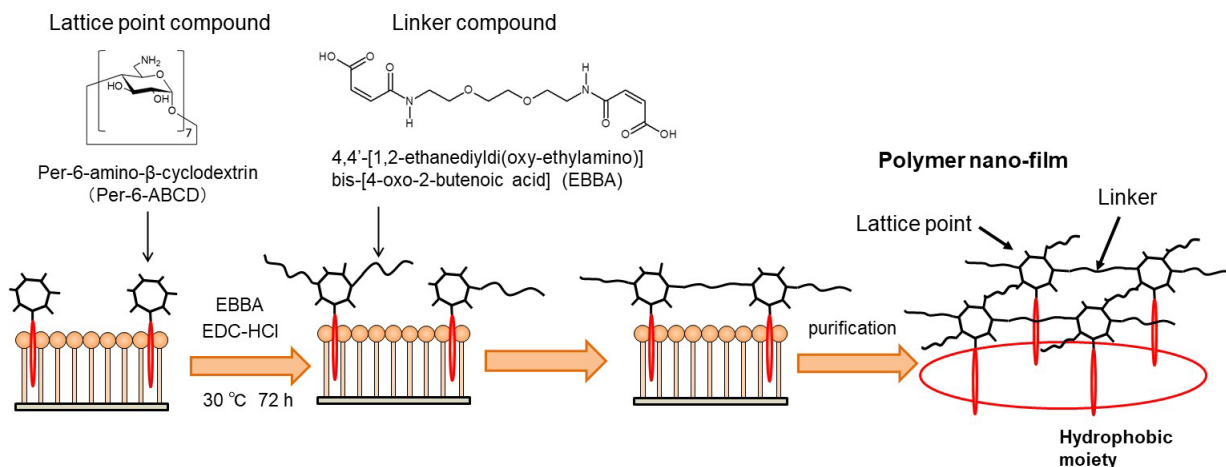


Fig. 1. Schematic illustration of the fabrication of polymer nano-film possessing hydrophilic and hydrophobic surface with the self-assembled phospholipid layer containing stearic acid.

The morphology of polymer nano-film in dry state was also estimated by AFM.

2. Experimental

2.1. General methods

¹H-NMR spectra were recorded on a JNM-ECZ400S FT-NMR spectrometer (JEOL) in either dimethyl sulfoxide-*d*₆ (DMSO-*d*₆) or methanol-*d*₄ (CD₃OD) or D₂O. TMS was used as an internal standard in DMSO-*d*₆ and CD₃OD.

2.2. Materials

Succinic acid was purchased from Kishida Chemical Co., Ltd. Glutaric acid and azelaic acid were obtained from Nakalai Tesque Inc. Per-6-amino-β-cyclodextrin (Per-6-ABCD) was synthesized according to the literatures [22].

2.3. Synthesis of benzyl phenyl carbonate (BPC)

To a solution of benzyl alcohol (1600mg, 15 mmol) and pyridine (1.2 mL) in dry dichloromethane (DCM) was added a solution of phenyl chloroformate (2350 mg, 15 mmol) in dry DCM (30 mL) in an ice bath. The reaction mixture was stirred at room temperature overnight, and then washed with 5% of sodium hydroxide aqueous solution, 1 mol/L of HCl aqueous solution and saturated saline. The DCM layer was dried and evaporated in vacuo to obtain BPC as a yellow oily substance (72 % yield). ¹H-NMR (400 MHz, DMSO-*d*₆): δ = 7.51-7.44 (m, 2H); 7.44-7.42 (m, 2H); 7.42-7.39 (m, 2H); 7.39-7.36 (m, 1H); 7.32-7.27 (m, 1H); 7.27-7.21 (m, 2H); 5.28 (s, 2H).

2.4. Synthesis of CBZ-TREN

To a solution of tris-(2-aminoethyl)amine (790mg,

5.4 mmol) in dry DCM was dropwisely added a solution of BPC (2500 mg, 11 mmol) in dry DCM (10 mL) in an ice bath under N₂ atmosphere. The reaction mixture was stirred at room temperature overnight, and then evaporated in vacuo. Column chromatography on silica gel (eluted with methanol/DCM=1/19 containing 1% triethylamine) afforded the desired product as a yellow green oil (77 % yield). ¹H-NMR (400 MHz, DMSO-*d*₆): δ = 7.39-7.34 (m, 4H); 7.34-7.32 (m, 4H); 7.32-7.27 (m, 2H); 7.22 (t, 2H); 5.01 (s, 4H); 3.16-3.09 (br, 2H); 3.05 (q, 4H); 2.54-2.49 (m, 2H); 2.49-2.43 (m, 4H); 2.43-2.34 (m, 2H).

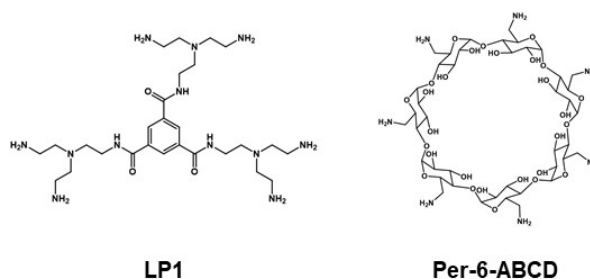


Fig. 2. Structures of lattice point compounds.

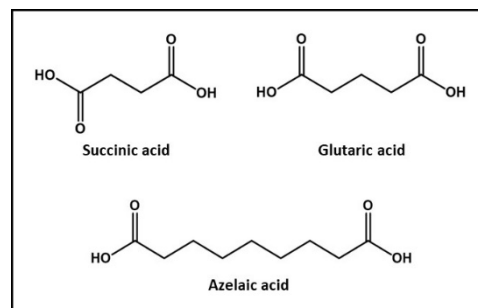


Fig. 3. Structures of three kinds of linker.

2.5. Synthesis of CBZ-LP1

A solution of 1,3,5-benzene tricarboxylic acid (270mg, 1.3 mmol) and 1-ethyl-3-(3-dimethylaminopropyl)carbodiimide hydrochloride (EDC·HCl) (800mg, 4.2 mmol) in dry dimethylformamide (DMF) was stirred for 1 h in an ice bath. To this solution was added a solution of CBZ-TREN (1700 mg, 4.2 mmol) in dry DNF (20 mL) in an ice bath. The reaction mixture was stirred at 8 °C overnight, and then evaporated in vacuo. Column chromatography on silica gel (eluted with methanol/DCM=3/17) afforded the desired product as a yellow solid (56 % yield). ¹H-NMR (400 MHz, DMSO-d₆): δ = 8.64 (t, 3H); 8.38 (s, 3H); 7.39-7.32 (m, 12H); 7.32-7.30 (m, 12H); 7.30-7.25 (m, 6H); 7.19 (t, 6H); 4.98 (s, 12H); 3.32 (q, 6H) 3.06 (q, 12H) 2.62 (t, 6H); 2.54 (t, 12H).

2.6. Synthesis of LP1

Pd(OH)₂ (99 mg) was added to a solution of CBZ-LP1 (990mg, 0.7 mmol) in dry methanol. The reaction mixture was stirred under H₂ atmosphere at room temperature for 24 h. The reaction mixture was filtered on celite and evaporated in vacuo. The desired compound was obtained as a yellow solid (92 % yield). ¹H-NMR (400 MHz, CD₃OD): δ = 8.64 (t, 3H); 8.53 (s, 3H); 3.52 (q, 6H); 2.84 (t, 12H); 2.74 (t, 6H); 2.68 (t, 12H); 2.62 (m, 12H).

2.7. Preparation of polymer nano-film

According to the literatures, LDPE-StA-PC-SA was fabricated, and then LP1 was immobilized on the LDPE-StA-PC-SA film [17, 18]. To 100 mL of water was added 1 mL of 0.047 μmol/ml EDC·HCl aqueous solution and 50 μL of 29 μmol/ml succinic acid in aqueous solution. This solution was kept at 30 °C for 30 min. The LDPE-StA-PC-SA film immobilizing LP1 (1 x 3 cm, 40 films) was soaked into this solution at 30 °C for 18 h. These films were washed with water. The films were immersed into 60 mL of ethanol and kept at 30 °C for 3 h. This ethanol solution was concentrated to about 7 mL in vacuo. The concentrated solution was transferred into a pre-swollen semi-permeable membrane (Spectra/ Por® 1 Dialysis Membrane Standard RC Tubing MWCO: 6 - 8 kD, Spectrum Laboratories, Inc.). The both sides of the tube were sealed with dialysis tubing closures (Dialysis Tubing Closures Standard Closure Type, 80 mm). The solution was dialyzed against 300 mL of methanol for 15 h. And then the dialysis membrane was immersed into 300 mL of pH 7.4 PBS to obtain the polymer nano-film solution. The polymer nano-

films crosslinked with glutaric acid or azelaic acid were also prepared in the similar manner.

2.8. Dynamic light scattering (DLS) measurement

DLS was measured by using a DLS-8000 (Otsuka Electronics) equipped with a He/Ne laser ($\lambda_0 = 633$ nm). A scattering angle of 90° was used to evaluate the size of polymer nano-film. The hydrodynamic diameter and the polydispersity factor, represented as μ_2/Γ^2 , were calculated using the Stokes-Einstein equation and the cumulant method. The number-average particle diameter was determined by histogram method with Marquardt calculation. Three replicates were measured.

2.9. Atomic force microscope (AFM) measurement in dynamic force mode

The PBS of polymer nano-film was exchanged into distilled water. The aqueous solution of polymer nano-film was casted on mica, and then dried to obtain AFM sample. The morphology of polymer nano-film was investigated by AFM with dynamic force mode employing Scanning Probe Microscopy AFM-5400L (Hitachi High-Technologies Co.) and cantilever (SI-DF20P2). AFM measurement was performed under atmospheric conditions.

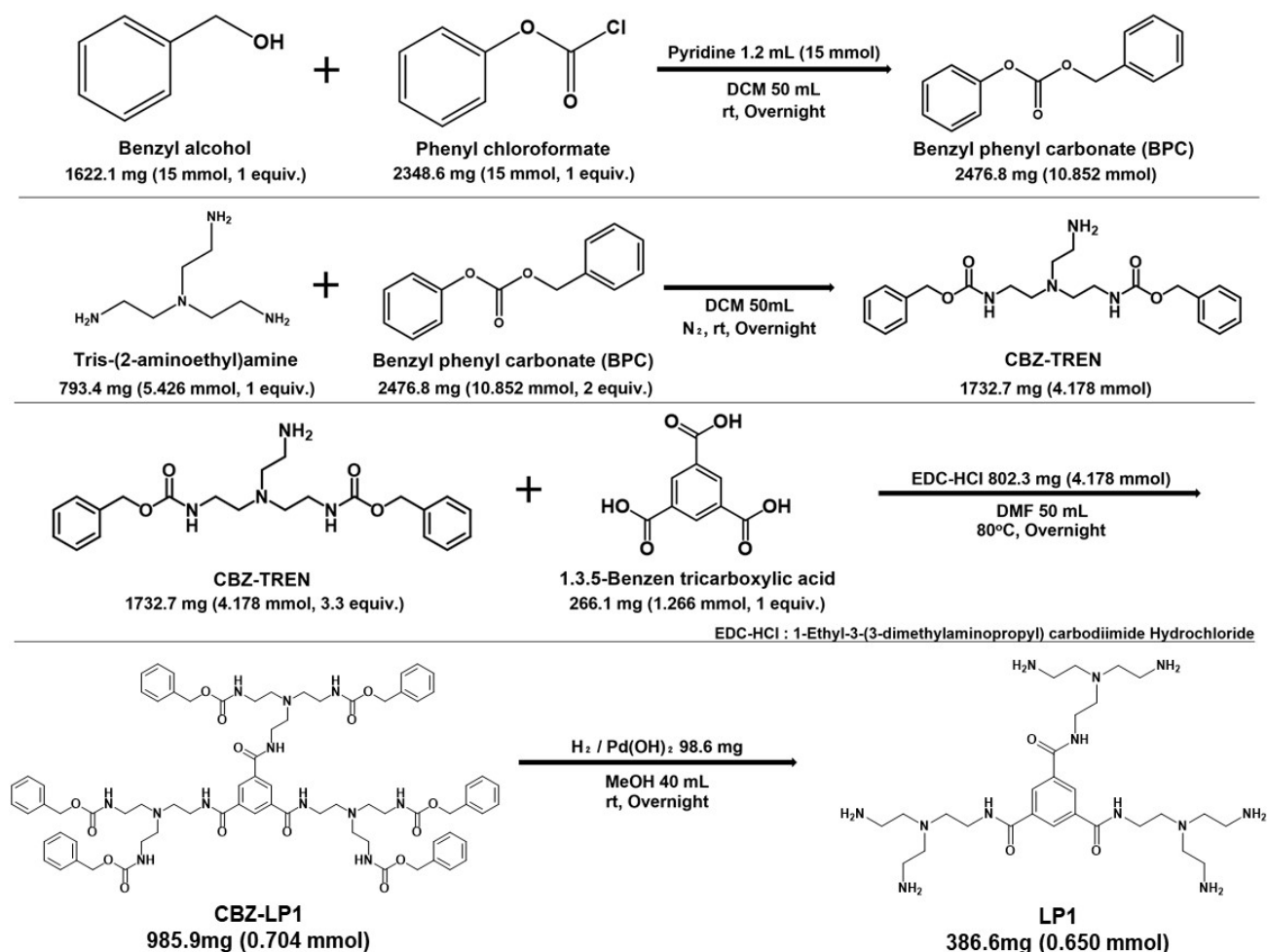
3. Results and Discussion

3.1. Synthesis of LP1

Scheme 1 shows the synthetic scheme of LP1. LP1 was synthesized in four step reactions. Total chemical yield was about 30 %. As shown in Fig. 2, LP1 possesses more flexible side chain of amino groups than those of Per-6-ABCD.

3.2. Changes in particle diameter of polymer nano-film by the different in lattice point compound

We synthesized two types of polymer nano-film, which were composed of LP1 or Per-6-ABCD as a lattice point compound, with azelaic acid as a linker moiety. The particle diameter of polymer nano-film was measured on DLS in methanol, pH 5 PBS and pH 7.4 PBS. Figure 4 shows the changes in particle diameter of polymer nano-film composed of LP1 or Per-6-ABCD against crosslinking time. It was seen from Fig. 4 that the particle diameter of both polymer nano-films increased with increasing crosslinking time and leveled off at about 8 h for LP1 and about 2 h for Per-6-ABCD. It was also shown that the particle diameters of polymer nano-film composed of LP1 were larger than those of Per-6-ABCD in each solvent. It was assumed that larger particle size of LP1 polymer nano-film might ascribe



Scheme 1

to the more flexible side chain and that the bulky and rigid structure of Per-6-ABCD might restrict the crosslinking reaction due to the steric hindrance.

The particle diameters of both polymer nano-films decreased in the order of methanol, pH 5 PBS and pH 7 PBS. This order could be rationalized as follows. These polymer nano-film possessed hydrophilic moiety (surface of LP1 and Per-6-ABCD) and hydrophobic moiety (surface binding stearic acid). As methanol is a good solvent for hydrophilic and hydrophobic moiety, these polymer nano-film would be expanded and showed the largest particle diameter among them. In aqueous solution the hydrophobic moieties could be turned inward, so that these polymer nano-films indicated smaller particle diameter than methanol due to a shrank conformation. There were several free amino groups which were unbounded to linker or stearic acid in one lattice point compound. As free amino groups were protonated in acidic condition, electrostatic repulsion between protonated amino groups would cause the expansion of polymer nano-

film. Therefore, the particle diameter at pH 5 was larger than that at pH 7.4.

3.3. Changes in the particle diameter of polymer nano-film synthesized with LP1 against linker length

Polymer nano-films were prepared with LP1 and three kinds of linkers shown in Fig. 3, and their particle diameter was measured on DLS measurement.

Table 1 shows the particle diameter of polymer nano-films in pH 7.4 PBS. The particle diameter of polymer nano-film increased with increasing the linker length and the crosslinking time. It was suggested that the particle diameter of polymer nano-film could be controlled by the linker length and the crosslinking time.

3.4. Morphology estimation of polymer nano-film in dry condition by AFM measurement

The methanol or aqueous solution of polymer nano-film synthesized with LP1 and azelaic acid were casted on mica, and then dried to obtain the

AFM sample. Figure 5 shows the AFM images of polymer nano-film synthesized with LP1.

Although the particle diameter estimated on AFM measurement was clearly smaller than those on DLS measurement, the order of particle diameter measured on AFM was same with those on DLS (see Fig. 4). Although DLS measurement was carried out in a solution, AFM measurement was performed in a dry state (without solvent). It was considered that the polymer nano-film would be remarkably shrunk in a dry state. As shown in Fig. 5 (A), the morphology of polymer nano-film from MeOH showed nearly rectangle shape, and the thickness was 1.27 nm. On the other hand, the polymer nano-film from water showed spherical or oblong morphology (Fig. 5 (B)), and the thickness was 5.24 nm. As mentioned above, methanol could solvate with both hydrophobic and hydrophilic moiety, but water could solvate with only hydrophilic moiety. Separately we measured ¹H-NMR spectra of polymer nano-film in CD₃OD and D₂O. ¹H-NMR spectra in CD₃OD showed the sharp peaks ascribed to LP1 and stearic acid moiety. However, ¹H-NMR spectra in D₂O indicated the sharp peaks of LP1 and the broad peaks of stearic acid moiety. These results suggested that the polymer nano-film in methanol might be expanded like a sheet and that the hydrophobic moiety might be turned inward in water to form a spherical or rod-like shape.

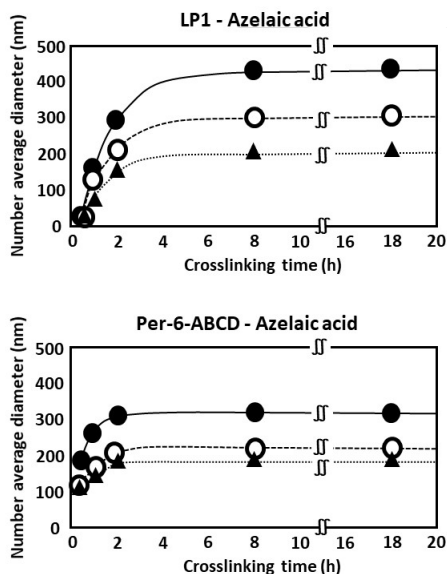


Fig. 4. Changes in particle diameter of polymer nano-film composed of LP1 or Per6-ABCD against crosslinking time.

● ; MeOH, ○ ; pH 5 PBS, ▲ ; pH 7.4 PBS.

The number average particle diameter was measured on DLS.

Table 1. Particle diameter (nm) of polymer nano-film with three kinds of linkers.

	2h	8h	18h
Succinic acid	80	140	150
Glutaric acid	110	160	165
Azelaic acid	150	200	205

The particle diameter of polymer nano-films was recorded on DLS in pH 7.4 PBS.

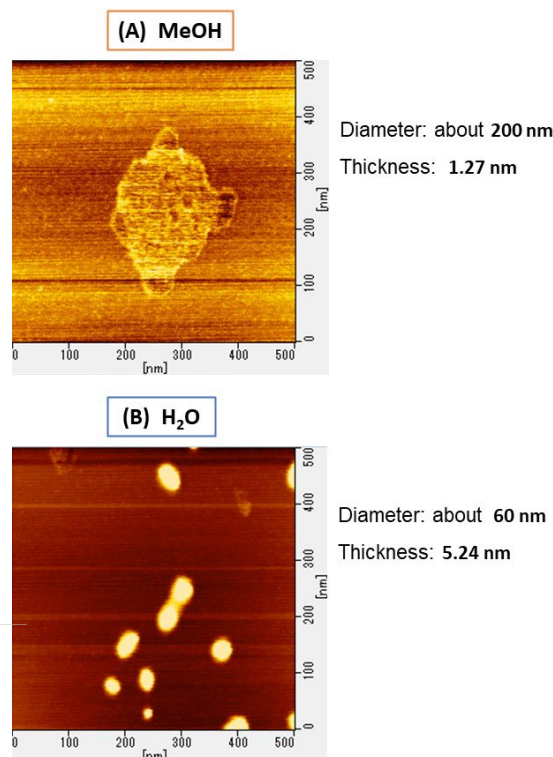


Fig. 5. AFM images of polymer nano-film in methanol (A) and water (B).

The polymer nano-film was synthesized with LP1 and azelaic acid

4. Conclusion

The conclusions drawn from the present study can be summarized as follows.

LP1 was synthesized in four step reactions. Total chemical yield was about 30 %. We synthesized two types of polymer nano-film, which were composed of LP1 or Per-6-ABCD as a lattice point compound, with azelaic acid as a linker moiety. The particle diameters of polymer nano-film composed of LP1 were larger than those of Per-6-ABCD in methanol and PBS. It was assumed that larger particle size of LP1 polymer nano-film might ascribe to the more flexible side chain and that the

bulky and rigid structure of Per-6-ABCD might restrict the crosslinking reaction due to the steric hindrance. The morphology of polymer nano-film from MeOH showed nearly rectangle shape, and the thickness was 1.27 nm. On the other hand, the polymer nano-film from water showed spherical or oblong morphology, and the thickness was 5.24 nm. These results suggested that the polymer nano-film in methanol might be expanded like a sheet and that the hydrophobic moiety might be turned inward in water to form a spherical or rod-like shape.

We are now actively elaborating the application to a drug carrier using the present polymer nano-film.

References

1. H. Tanaka, M. Mitsuishi, and T. Miyashita, *Chem. Lett.*, **34** (2005) 1246.
2. H. Endo, Y. Kado, M. Mitsuishi, and T. Miyashita, *Macromolecules*, **39** (2006) 5559.
3. H. Zhu, M. Mitsuishi, and T. Miyashita, *Macromolecules*, **45** (2012) 9076.
4. K. Takada, R. Sakamoto, S.-T. Yi, S. Katagiri, T. Kambe and H. Nishihara, *J. Am. Chem. Soc.*, **137** (2015) 4681.
5. C. Kuru, C. Choi, A. Kargar, D. Choi, Y. J. Kim, C. H. Liu, S. Yzvuz, and S. Jin, *Adv. Sci.*, **2** (2015) 1500004.
6. T. Bauer, Z. Zheng, A. Renn, R. Enning, A. Stemmer, J. Sakamoto, and A. D. Schlüter, *Angew. Chem.*, **50** (2011) 7879.
7. S. Motoyama, R. Makiura, O. Sakata, and H. Kitagawa, *J. Am. Chem. Soc.*, **133** (2011) 5640.
8. Z. Zheng, L. Opilik, F. Schiffmann, W. Liu, G. Bergamini, P. Ceroni, L.-T. Lee, A. Schlütz, J. Sakamoto, R. Zenobi, J. VandeBondele, and A. D. Schlüter, *J. Am. Chem. Soc.*, **136** (2014) 6103.
9. B. Ni, M. Huang, Z. Chen, Y. Chen, C.-H. Hsu, Y. Li, D. Pochan, W.-B. Zhang, S. Z. D. Cheng, and X.-H. Dong, *J. Am. Chem. Soc.*, **137** (2015) 1392.
10. N. Idota, S. Fukuda, T. Tsukahara, and Y. Sugahara, *Chem. Lett.*, **44** (2015) 203.
11. B. P. Nsdyskoyi, Y. Li, M. Imura, N. Miyamoto, T. Nakato, T. Sasaki, and Y. Yamauchi, *Angew. Chem.*, **54** (2015) 4222.
12. M. Kuzuya and T. Yamashiro, *J. Photopolym. Sci. Technol.*, **8** (1995) 381.
13. M. Kuzuya, Y. Matsuno, T. Yamashiro, and M. Tuiki, *Plasmas Polym.*, **2** (1997) 79.
14. M. Kuzuya, T. Yamashiro, S. Kondo, and M. Tuiki, *Plasmas Polym.*, **2** (1997) 133.
15. M. Kuzuya, T. Sawa, T. Yamashiro, S. Kondo, and O. Takai, *J. Photopolym. Sci. Technol.*, **14** (2001) 87.
16. S. Kondo, Y. Sasai, and M. Kuzuya, *Thin Solid Films*, **515** (2007) 4136.
17. S. Kondo, Y. Sasai, Y. Yamauchi, and M. Kuzuya, *J. Photopolym. Sci. Technol.*, **22** (2009) 477.
18. S. Kondo, T. Kusumoto, Y. Sasai, N. Doi, Y. Yamauchi, and M. Kuzuya, *J. Photopolym. Sci. Technol.*, **29** (2016) 439.
19. S. Kondo, Y. Sasai, Y. Yamauchi, and M. Kuzuya, *J. Photopolym. Sci. Technol.*, **31** (2018) 385.
20. S. Kondo, Y. Sasai, Y. Yamauchi, and M. Kuzuya, *J. Photopolym. Sci. Technol.*, **32** (2019) 541.
21. S. Kondo, N. Doi, Y. Sasai, Y. Yamauchi, and M. Kuzuya, *J. Photopolym. Sci. Technol.*, **34** (2021) 533.
22. S. Kondo, M. Suzuki, Y. Sasai, Y. Yamauchi, and M. Kuzuya, *J. Photopolym. Sci. Technol.*, **26** (2013) 545.

Preparation of a Polysilane–Methacrylate Copolymer with Two Methacrylate Species

Yukihito Matsuura^{1*}, Chihiro Amasaki¹, Tomoya Hasegawa², Masanobu Ohkita², and Tomoharu Tachikawa²

¹Department of Chemical Engineering, National Institute of Technology, Nara College
22 Yatacho, Yamato-koriyama, Nara 639-1080, Japan

²Frontier Materials Laboratories, Osaka, Gas Chemicals Co., Ltd.
5-11-61, Torishima, Konohana-ku, Osaka 554-0051, Japan

*matsuura@chem.nara-k.ac.jp

Polysilanes possess both electrical and optical functionalities. To use a polysilane in electronic devices, it must be chemically modified to connect to a metal atom. We developed a synthesis method for a polysilane–methacrylate copolymer using a polysilane as the photoradical initiator because methacrylate can be easily modified. Notably, both ends of the polysilane block are expected to be modified with methacrylate, which has a reactive functional group, to form chemical bonds with the metal electrodes in electronic devices. In this study, we prepared a polysilane–methacrylate copolymer with two methacrylate species. The methacrylates used for photopolymerization were 2-(methylthio)ethyl methacrylate and glycidyl methacrylate.

Keywords: Polysilane, 2-(Methylthio)ethyl methacrylate, Glycidyl methacrylate, Photopolymerization

1. Introduction

Polysilanes possess continuous Si–Si covalent bonds that result in electrical conductivity and absorption/luminescence in the ultraviolet (UV) range [1, 2]. Furthermore, we found that polysilanes amplified the spin polarization and exhibited magnetoresistance properties [3, 4]. However, these polymers have not been applied to electronic devices because they react with O₂/H₂O and gradually degrade. We developed a polysilane–methacrylate copolymer using a polysilane as the photoradical initiator by intentionally retaining the polysilane block [5, 6]. The methacrylate of a copolymer can be easily modified with reactive functional groups [7-9].

It has also been found that a molecule with a helical structure, such as a protein, exhibits a spin selectivity effect, that is, chiral-induced spin selectivity [10-12]. Furthermore, the tunneling distance in a protein molecule is comparable to that in a π -conjugated molecule [13]. Polysilanes also exhibit electrically conductive characteristics comparable to those of π -conjugated molecules [14]. If bond formation between a protein and

polysilane can be achieved for the purpose of passing an electric current, the polysilane may amplify the spin polarization that is induced in the protein. This protein–polysilane hybrid can be applied to magnetoelectronic devices. Furthermore, the unknown structure of a protein can be examined by forming a polysilane hybrid to measure the electric current as an aid for

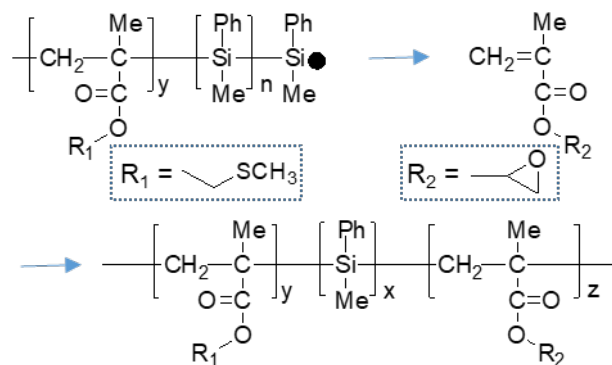


Fig. 1. Chemical structure of polysilane modified with 2-(methylthio)ethyl methacrylate (mteMA) and glycidyl methacrylate (glcMA).

nuclear magnetic resonance (NMR) and X-ray structural analyses. Polysilane–methacrylate copolymers with reactive functional groups such as isocyanates and amides have been developed by our research group [15–17].

In this study, a polysilane was modified with glycidyl methacrylate (glcMA), which can form covalent bonds with protein-containing alcohols [18]. Furthermore, because polysilanes must be modified to connect to the metal electrode, the polysilane used was reacted with 2-(methylthio)ethyl methacrylate (mteMA), which can adhere to the gold substrate via S–Au interactions [19]. In this study, as shown in Figure 1, we initially attempted the photopolymerization of a polysilane with mteMA. Subsequently, glcMA was reacted with the polysilane–mteMA copolymer as a photochemical initiator to modify the polysilane with both mteMA and glcMA.

2. Experimental

2.1 Materials

Poly(methylphenylsilane) (PMPS) was supplied by Osaka Gas Chemicals Co., Ltd. (OGSOL SI-10-10) [20]. The crude sample was purified using hexane via reprecipitation. glcMA and mteMA were purchased from Sigma-Aldrich Co., LLC. The methacrylate photoreaction was performed using the polysilane as a photoradical initiator.

A typical photoreaction was performed as follows: PMPS (0.5 g) and mteMA (0.5 g) were dissolved in distilled toluene (5 mL) in a Pyrex glass tube. The ratio of the units of methylphenylsilane (MPS) to methacrylate was approximately equimolar in the mixture. Degassing was performed using the freeze–thaw method. The tube was then irradiated with UV light (SEN LIGHTS CORPORATION,

high-pressure Hg lamp, 10 mW cm⁻²) for 15 min. The reaction mixture was reprecipitated in hexane (300 mL) and filtered through a glass filter (pore size: 20–30 μm). Finally, the residue obtained was vacuum-dried overnight. The product is referred to as PMPS–mteMA.

Using the same synthesis method, glcMA was used for the subsequent photopolymerization step using the first product as a photoradical initiator to obtain a polysilane modified with mteMA and glcMA. The polymerization step was carried out by varying the UV irradiation time to 5, 15, or 30 min. The products are referred to as Product-5, Product-15, and Product-30, respectively.

2.2 Measurements

The molecular weight was analyzed in tetrahydrofuran using a Shodex GPC-101 system with polystyrene standards. The ratio (x/y/z) of the number of MPS units to that of MA units was determined by ¹H-NMR spectroscopy using a JEOL JNM-ECX400 spectrometer with deuterated chloroform as the solvent. UV–visible (UV–vis) absorption spectra were obtained using a Shimadzu UV-3600 spectrophotometer. Fourier-transform infrared (FT-IR) spectra were obtained using a Shimadzu IR Affinity-ATR system equipped with a zinc selenide crystal. Raman spectroscopy was performed using a Raman microspectroscopy system Nanofinder 30 A spectrometer (Tokyo Instruments) with a 532 nm green laser. Thermogravimetric (TG) analysis was carried out using a Seiko Instrument TG/DTA7200 at a heating/cooling rate of 10 °C min⁻¹ in the temperature range of 30–550 °C. Differential scanning calorimetry (DSC) was performed using a Seiko Instrument DSC-X5400

Table 1. Characterization of products by GPC, ¹H-NMR, and UV-Vis absorption spectroscopy.

Sample	GPC		¹ H-NMR			UV-Vis
	Mn/10 ³	Mw/Mn	x	y	z ²⁾	λ _{max} (nm)
PMPS	5.1	3.2	136			331.4
PMPS–mteMA	5.4	2.4	94	9		326.0
Product-5 ¹⁾	5.1	2.4	80	9	5	325.5
Product-15	5.0	2.4	72	9	13	325.3
Product-30	4.5	2.1	60	8	13	324.0

¹⁾ Product prepared from PMPS–mteMA and glcMA by UV-irradiation for 5 min.

²⁾ x, y, and z were average values of units of MPS, mteMA, and glcMA.

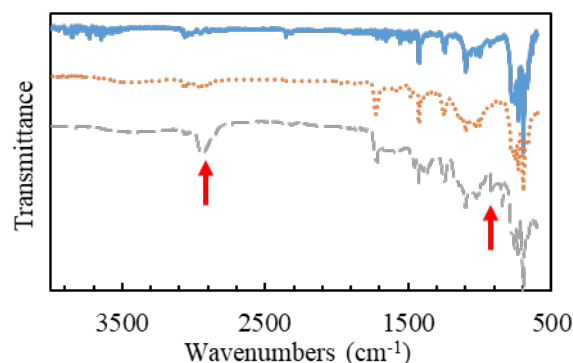


Fig. 2. FT-IR spectra of PMPS (blue solid line), PMPS–mteMA (orange dotted line), and product-15 (gray hash-dotted line).

at a heating/cooling rate of $10\text{ }^{\circ}\text{C min}^{-1}$ in the temperature range from -30 to $230\text{ }^{\circ}\text{C}$.

3. Results and discussion

We used PMPS–mteMA, which was synthesized from PMPS, as the photoradical initiator [19] to modify PMPS–mteMA with glcMA. Figure 2 shows the FT-IR spectra of PMPS, PMPS–mteMA, and Product-15. Compared to the spectrum of PMPS, the PMPS–mteMA spectrum exhibits a peak at 1720 cm^{-1} corresponding to the carbonyl group of the methacrylate. In addition, the spectrum of Product-15 had a peak at 916 cm^{-1} corresponding to the epoxy group of glcMA. Furthermore, the broad peak observed at approximately 2900 cm^{-1} in the Product-15 spectrum increased in vibration intensity compared to that in the PMPS–mteMA spectrum owing to the presence of methylene in the epoxy group. The FT-IR spectra of Product-5 and Product-30 showed the same tendency as that of Product-15. These results confirm the addition of glcMA to PMPS–mteMA.

Figure 3 shows the UV-vis absorption spectra of PMPS, PMPS–mteMA, and Product-15. PMPS exhibited UV absorption at 331.4 nm , which was derived from the σ -conjugation of continuous Si–Si bonds. PMPS–mteMA also exhibited UV absorption at a wavelength lower than that of PMPS, suggesting that photopolymerization shortens the polysilane block. Product-15 also exhibited UV absorption; however, its relative absorbance intensity decreased, resulting in a shoulder peak whose wavelength shifted to lower than that of PMPS–mteMA. This suggests that Product-15 retained the polysilane block even after two sequential photopolymerization steps.

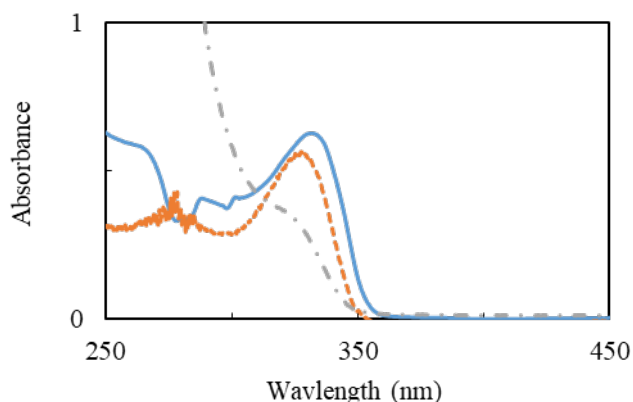


Fig. 3. UV-Vis absorption spectra of PMPS (blue solid line), PMPS-sulMA (orange dotted line), and product-15 (gray hash-dotted line).

Subsequently, quantitative structural analysis of the Product-5, -15, and -30 was performed using gel permeation chromatography (GPC), $^1\text{H-NMR}$, and UV-vis absorption spectroscopy. The properties of the products obtained are listed in Table 1. The average values of the unit numbers (x, y, z) were calculated from M_w and the ratios ($x/y/z$) determined by $^1\text{H-NMR}$ spectroscopy [21]. It was revealed that Product-5 contained glcMA units. The molecular weight of Product-5 was lower than that of PMPS–mteMA because of the decrease in the number of MPS units. This result was also confirmed by the redshift in the UV absorption (λ_{max}) of PMPS–mteMA. Product-15 had a similar molecular weight as Product-5, whereas the number of glcMA units was higher than that of PMPS–mteMA. In addition, Product-15 had a lower number of MPS units compared to Product-5, which was also confirmed by the redshift in λ_{max} . The molecular weight of Product-30 was lower than that of Product-15, whereas the number of mteMA and glcMA units remained almost unchanged. Based on these results, we can confirm that PMPS modified with mteMA and glcMA was prepared via the sequential photopolymerization of PMPS and two methacrylate species. Furthermore, it was clear that an excess UV irradiation of > 15 min retained the number of methacrylate units and shortened the polysilane block. Therefore, Product-15 is discussed in detail hereinafter because the polysilane block is relatively longer than that of the other products.

Figure 4 shows the TG results for PMPS, PMPS–mteMA, and Product-15. The weight of

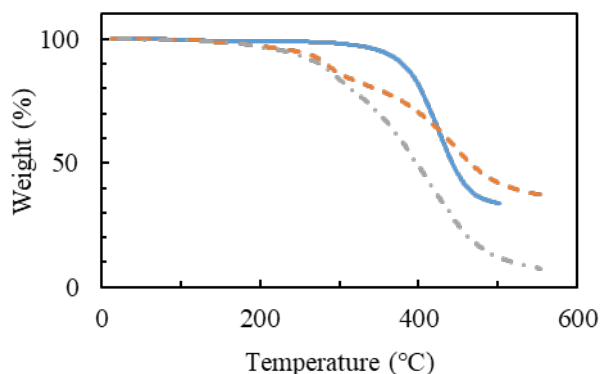


Fig. 4. Thermogravimetric (TG) analysis of PMPS (blue solid line), PMPS-mteMA (orange dotted line), and product-15 (gray hash-dotted line).

PMPS decreased at 350 °C and then continued to decrease monotonically to become 34 %. The weight of PMPS–mteMA showed a gradual decrease from 200 °C. The decrease in weight became moderate at 350 °C and diminished again from 400 °C to become 37 %. The first decrease in weight at 200 °C was due to the chain cleavage of mteMA blocks. The TG results of Product-15 showed the same tendency as those of PMPS–mteMA. The decrease in weight at 200 °C cannot be deconvoluted into mteMA and glcMA. Because the relative proportion of the polysilane block (the MPS unit) of Product-15 was smaller than that of PMPS–mteMA, the final decrease in its weight was 8.7 %. The residue obtained at > 500 °C may be silicon carbide-like compounds [22].

Subsequently, DSC analyses were performed on PMPS, PMPS–mteMA, and Product-15, and the results are shown in Figure 5. PMPS and PMPS–mteMA exhibited glass transitions at 150 and 146 °C, respectively. The glass-transition temperature of PMPS–mteMA was slightly lower than that of PMPS because of the shorter length of its polysilane blocks. Although the glass transition of Product-15 became unclear, a gentle step in the DSC curve was observed at approximately 130 °C, indicating a relatively short length of the polysilane block of Product-15, which was synthesized via two photopolymerization steps.

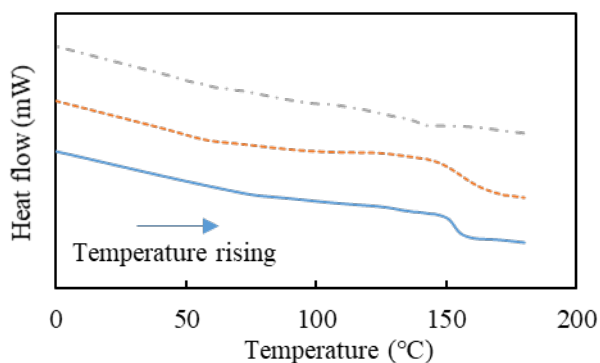


Fig. 5. DSC analysis of PMPS (blue solid line), PMPS-mteMA (orange dotted line), and product-15 (gray hash-dotted line).

Finally, the Raman spectra were analyzed, and the results are shown in Figure 6. The thickness of the films was approximately 5 μm. In general, Raman scattering analysis reflects the vibrations of isotropic bonds with a high polarizability. As

PMPS–mteMA and Product-15 consisted primarily of a polysilane structure, their Raman spectra were similar to that of PMPS. However, different results were obtained for PMPS and PMPS–mteMA upon detailed analyses of the spectra. Figures 6 (a), 6 (b), and 6 (c) show the depth profiles of the Raman spectra of PMPS and PMPS–mteMA, and Product-15, respectively. PMPS had Raman peaks at 702, 718, and 740 cm^{-1} . Although the detailed identification is unclear, these peaks can be assigned to the stretching vibrations of C–H and Si–C [23]. PMPS–mteMA exhibited Raman peaks at similar wavenumbers, with a shoulder peak at 705 cm^{-1} assigned to C–S bonding. This peak is located on the outermost surface of the Raman depth profile. Generally, the penetration length of a green laser is approximately 500 nm for a silicon wafer [24, 25]. Although our polysilane-related compounds possess organic moieties, we predict that their penetration length will have the same tendency as that of other polysilane-related compounds. Therefore, the PMPS–mteMA film contained S–CH₃ on its surface. As a film of Product-15

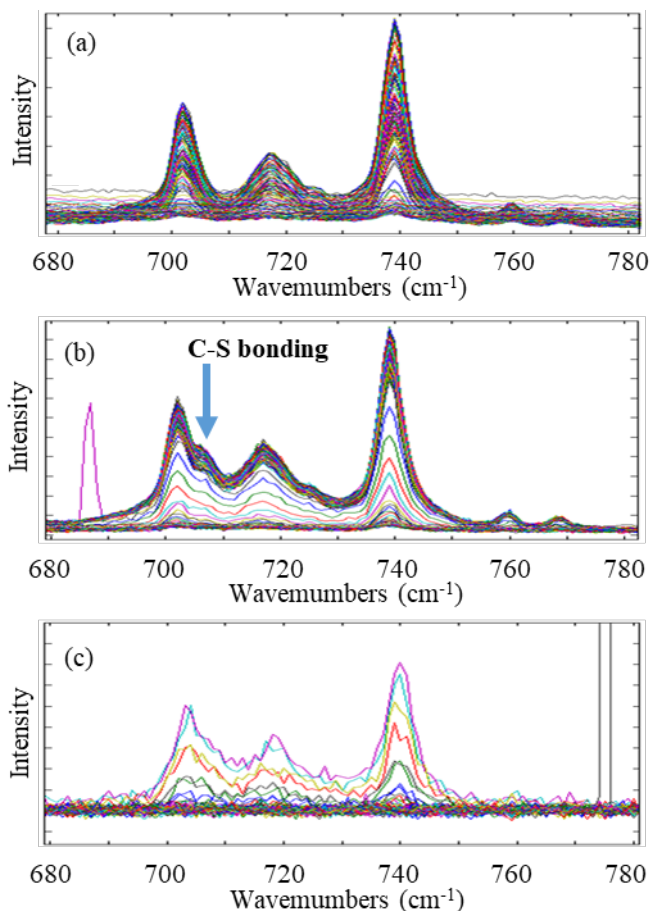


Fig. 6. Depth profile of Raman spectra of (a) PMPS, (b) PMPS-mteMA, and (c) Product-15.

was not film formation properties, the depth profile of Raman spectrum did not have a good resolution. However, Product-15 exhibits a similar Raman spectrum in this wavenumber range with PMPS-mteMA. We could not determine the detailed arrangement of the MPS, mteMA, and glcMA units from ¹H-NMR and GPC analyses; however, the location of mteMA in the film could provide insight into the fabrication of a device structure.

Conclusion

Polysilane copolymers modified with two methacrylate species were successfully synthesized using a polysilane as the photoradical initiator. The products obtained were polysilane blocks of 2-(methylthio)ethyl methacrylate and glycidyl methacrylate. The products retained the optical and thermal characteristics of the polysilane. Furthermore, the film fabricated using the product has a specific location where the surface primarily shares a methylthio group. These properties can be used to fabricate bioelectronic devices in the future.

Acknowledgement

This work was supported by JSPS KAKENHI Grant Number 19K05638.

References

1. R. D. Miller and J. Michl, *Chem. Rev.*, **89** (1989) 1359.
2. K. Takeda, H. Teramae, and N. Matsumoto, *J. Am. Chem. Soc.*, **108** (1986) 8186.
3. Y. Matsuura, *J. Appl. Phys.*, **119** (2016) 205501.
4. Y. Matsuura, *J. Appl. Phys.*, **121** (2017) 165501.
5. Y. Matsuura, K. Matsukawa, and H. Inoue, *Chem. Lett.*, **30** (2001) 244.
6. F. Kato, Y. Matsuura, M. Ohikita, and T. Tachikawa, *J. Photopolym. Sci. Tech.*, **34** (2021) 255.
7. Y. Matsuura, H. Inoue, and K. Matsukawa, *Macromol. Rapid Commun.*, **25** (2004) 623.
8. Y. Matsuura, S. Miura, H. Naito, H. Inoue, and K. Matsukawa, *J. Organomet. Chem.*, **685** (2003) 230.
9. K. Matsukawa and Y. Matsuura, *Mater. Res. Soc. Symp. Proc.*, **847** (2005) EE10.1.1.
10. D. Mishra, T. Z. Markus, R. Naaman, M. Kettner, B. Göhler, H. Zacharias, N. Friedman, M. Sheves, and C. Fontanesi, *PNAS*, **110** (2013) 14872.
11. R. Naaman, Y. Paltiel, and D. H. Waldeck, *Nature Rev. Chem.*, **3** (2019) 250.
12. R. Naaman, Y. Paltiel, and D. H. Waldeck, *Annu. Rev. Biophys.*, **51** (2022) 99.
13. C. D Bostick, S. Mukhopadhyay, I. Pecht, M. Sheves, D. Cahen, and D. Lederman, *Rep. Prog. Phys.*, **81** (2018) 026601.
14. R. S. Klausen, J. R. Widawsky, M. L. Steigerwald, L. Venkataraman, and Colin Nuckolls, *J. Am. Chem. Soc.*, **134** (2012) 4541.
15. Y. Matsuura, K. Matsukawa, R. Kawabata, N. Higashi, M. Niwa, and H. Inoue, *Polymer*, **43** (2002) 1549.
16. Y. Matsuura, T. Sakatani, Y. Kado, Y. Takahashi, Y. Muramoto, S. Fukunishi, and S. Minami, *Euro. Polym. J.*, **108** (2018) 219.
17. Y. Matsuura, *J. Appl. Phys.*, **130** (2021) 184301.
18. K. Sugita, D. Aoki, and K. Arimitsu, The 102nd CSJ Annual Meeting, Proceeding C203-1am-10.
19. Y. Matsuura, H. Inoue, and K. Matsukawa, *Polymer J.*, **36** (2004) 560.
20. H. Murase, M. Sugimoto, H. Nishimura, and K. Yamada, *Mater. Sci. Appl.*, **6** (2015) 576.
21. Results of photoreaction of PMPS-mteMA and Product-15 as follows: ¹H-NMR (CDCl₃, 400 MHz, δ). PMPS-mteMA: -1.0 - 0.8 (-Si-CH₃ 3H), 0.8 - 1.1 (-C(Me)-CH₂ 2H), 1.6-2.1 (-C-CH₃ in methacrylate 3H), 1.9 - 2.1 (-C-SH₃ 3H), 2.5 - 2.7 (-C-CH₂-S- 2H), 4.0 - 4.2 (-O-CH₂-C- 2H), 6.4-7.6 (-Si-C₆H₅ 5H). PMPS-mteMA-glcMA: -1.0 - 0.8 (-Si-CH₃ 3H), 0.8 - 1.1 (-C(Me)-CH₂ 2H), 1.6-2.1 (-C-CH₃ in methacrylate 3H), 1.9 - 2.1 (-C-SH₃ 3H), 2.5 - 2.7 (-C-CH₂-S- 2H), 2.8 - 2.9 (-C-CH₂-C- in epoxy 2H), 3.2 - 3.3 (-C-CH(-O)-C- in epoxy 1H), 4.0 - 4.2 (-O-CH₂-C- 2H), 6.4-7.6 (-Si-C₆H₅ 5H).
22. W. R. I. Cranstone, S. M. Bushnell-Watson, and J. H. Sharp, *J. Mater. Res.*, **10** (1995) 2659.
23. N. B. Colthup, L. H. Daly, S. E. Wiberley, *Introduction to Infrared and Raman Spectroscopy*, Third Edition, Academic Press (1990).
24. M. A. Green and M. J. Keevers, M. J., *Progress in Photovoltaics: Research and Applications*, **3** (1995) 189.
25. M. A. Green, *Solar Energy Materials and Solar Cells*, **92** (2008) 1305.

Photomechanical Rolling Motion of Mixed Molecular Glass Microspheres Containing an Azobenzene-based Amorphous Molecular Material

Hajime Nigorikawa and Hideyuki Nakano*

*Department of Applied Chemistry, Muroran Institute of Technology,
27-1 Mizumoto-cho, Muroran, Hokkaido 050-8585, Japan.*

**nakano@mmm.muroran-it.ac.jp*

By casting the aqueous suspension of the mixture of BMAB and m-MTDATA, mixed molecular glass microspheres could be fabricated, whereas just dome-shaped particles of single BMAB were obtained using an aqueous suspension of BMAB. Resulting mixed glass microspheres of BMAB and m-MTDATA were found to exhibit photomechanical behaviors similar to those of single BFAB and PBAB glass microspheres as previously reported, whereas photomechanical behaviors of microdomes of BMAB were not so much obvious. Upon grazing-angle irradiation of the mixed glass microspheres of BMAB and m-MTDATA with s-polarized laser beam, photomechanical shape changes took place to form peculiar shapes with curved horns. On the other hand, grazing-angle irradiation with p-polarized laser beam induced photomechanical rolling motion to transport on a substrate away from the light source.

Keywords: Photomechanical Behavior, Azobenzene, Amorphous Molecular Material, Glass Transition Temperature

1. Introduction

Photomechanical behaviors observed for organic photochromic materials have been attracting attentions especially since the findings of reversible photoinduced bending motions of azobenzene-based liquid crystalline polymer films [1,2], reversible photoinduced shape changes of diarylethene-based microcrystals [3], and photoinduced surface relief grating (SRG) formation of azobenzene-based amorphous polymer films upon interference irradiation with two coherent laser beams [4,5]. A variety of photomechanical behaviors observed for a series of photochromic molecular crystals and polymer films have been reported so far. Among these, photomechanical rolling motion is one of the most attracting phenomena that is expected to find practical application. Photomechanical rolling motions of a ring-shaped continuous film of azobenzene-based liquid-crystalline elastomer upon UV and visible light irradiation [6] and the motions of wheels and helical ribbons composed of

azobenzene-containing liquid crystalline network polymer to transport on the substrate upon single UV irradiation [7] have been reported.

We have been studying the creation of photochromic amorphous molecular materials [8-10] and among these studies, a variety of photomechanical behaviors have been found using azobenzene-based amorphous molecular materials [11-22]. They include SRG formation on the amorphous molecular films [11-13], mass flow at the surface of the amorphous films and transport of the crashed particles on the substrate upon oblique irradiation with single p-polarized beam [14,15], photoinduced bending motion of molecular glass fibers where bending direction could be controllable by changing the polarization direction of incident laser beam [16,17], photoinduced striped pattern formation and the subsequent band-like structure formation of the amorphous film prepared on agar gel due to twinkling of the film depending on the polarization direction of incident laser beam [18]. With regard to the particles of

azobenzene-based molecular glasses fixed in agar gels, they exhibited drastic photoinduced shape changes to elongate parallel to the polarization direction of the incident laser beam to form wavy string-like structures [19-21] and the ends of resulting string-like structures were found to be helical with rather left-handed screw [21]. All of these photomechanical behaviors of azobenzene-based amorphous molecular materials depended on the polarization direction of the incident laser beam and can be explained by considering that the molecules tend to move and/or vibrate parallel to the polarization direction of the incident visible laser beam accompanied by photochromic trans-cis and cis-trans isomerization reactions.

Very recently, we have found novel photomechanical behaviors including rolling motions observed for molecular glass microspheres of BFIAB and PBAB [22]. Grazing-angle irradiation of their microspheres with s-polarized laser beam induced drastic shape changes to form peculiar shapes with curved horns. In contrast, grazing-angle irradiation with p-polarized laser beam induced transport of the microspheres away from the light source. Observation of the behaviors from the side indicated that microspheres exhibited rolling motion to transport on the substrate. For gain further information about these photomechanical behaviors, molecular glass particles of single BMAB and of the mixture of BMAB and m-MTDATA with micrometer size were fabricated on a substrate and their

photomechanical behaviors were investigated in the present study. Fig. 1 shows molecular formula of BFIAB, PBAB, BMAB, and m-MTDATA together with their glass transition temperatures (T_g).

2. Experimental

Molecular glass particles of BMAB with micrometer sizes were prepared on the transparent glass substrate as follows. A 0.25 mL of THF solution of BMAB (20 mg mL^{-1}) was rapidly added into hot water (2 mL) at ca. $80 \text{ }^\circ\text{C}$ with stirring. The resulting suspension was casted on the substrate on standing at room temperature. It was then dried under reduced pressure in a desiccator for more than 3 h. For preparing the mixed particles of BMAB and m-MTDATA with a molar ratio of 7:3, similar procedure has been made using THF solution of the mixture of BMAB (10.56 mg mL^{-1}) and m-MTDATA (9.44 mg mL^{-1}) instead of the THF solution of BMAB.

Photomechanical behaviors were investigated using the same set-up as that for studying the photomechanical behaviors of single BFIAB and PBAB microspheres upon grazing-angle irradiation [22]. The samples prepared on the substrate were irradiated with polarized laser beam (488 nm, CYAN-488-100 CDRH, SpectraPhysics Inc.) with a grazing angle θ of 10° . Polarization direction of the incident laser beam was controlled by using appropriate wave plate and polarizer. Irradiated power of the beam to the sample was 17 mW (ca. 1.7 W cm^{-2}) controlled by a variable ND filter. Time-lapse microphotographs were taken by CCD camera (VB-7010, KEYENCE) attached to the optical microscope (Optiphot X2, Nikon Co.).

3. Results and discussion

Sample particles with micrometer sized were prepared by casting the aqueous suspensions of BMAB with and without m-MTDATA onto a glass substrate, followed by drying under reduced pressure at room temperature. Fig. 2 shows the optical microphotographs of the side views of obtained particles of single BMAB and the mixture of BMAB and m-MTDATA. Whereas BMAB formed dome-shaped particles, the mixture of BMAB and m-MTDATA form microspheres on the substrate similar to the result for BFIAB and PBAB [22]. Relatively low T_g of BMAB was assumed to cause the sample to flow and spread out on the glass substrate during sample preparation, resulting in such dome shape.

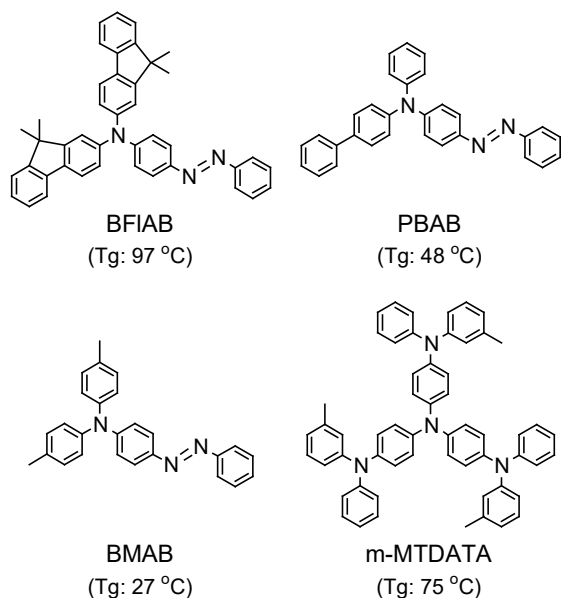


Fig. 1. Molecular Formula of BFIAB, PBAB, BMAB, and m-MTDATA with T_g .

Mixing with m-MTDATA was suggested to increase the T_g of the sample, allowing the formation of microspheres. In fact, T_g of the mixture of BMAB and m-MTDATA with a molar ratio of 7:3 was ca. 44 °C, estimated by differential scanning calorimetry, being higher than that of BMAB (27 °C). It was also suggested that microspheres obtained from mixed solutions of BMAB and m-MTDATA contained both materials homogeneously without separation.

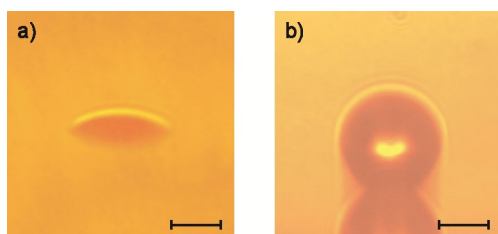


Fig. 2. Side views of the samples prepared on a substrate. a) BMAB, b) mixture of BMAB and m-MTDATA. Scale bar: 10 µm.

Fig. 3 shows the histogram of the size of the mixed glass microspheres of BMAB and m-MTDATA prepared on a substrate. The average diameter and standard deviation were 10.2 µm and 3.4 µm, respectively. The result was almost similar to those for single BFIAB and PBAB microspheres [22].

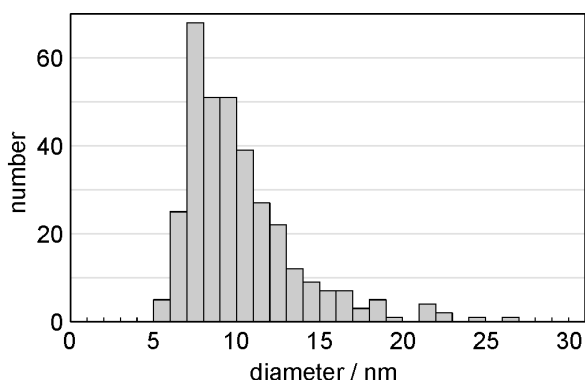


Fig. 3. Histogram of diameter of mixed microspheres of BMAB and m-MTDATA prepared on a glass substrate.

Then, photomechanical behaviors of the resulting mixed microspheres were investigated. Upon grazing-angle irradiation with a 488 nm s-polarized laser beam, drastic shape changes were observed. As shown in Fig. 4, the microspheres changed to form peculiar shapes with curved horns, being similar to the photomechanical behaviors observed for single BFIAB and PBAB

microspheres [22]. It was assumed that the molecules in the irradiated region move parallel to the polarization direction to form horns in both directions. At that time, the more irradiated photons were absorbed near the irradiated surface of the sample than inside, so that the closer side of the resulting horns to the light source elongate more efficiently than the opposite side, forming a curved structure away from the light source. Such photomechanical behavior was scarcely observed for BMAB microdome maybe due to such particle shape and its relatively low T_g .

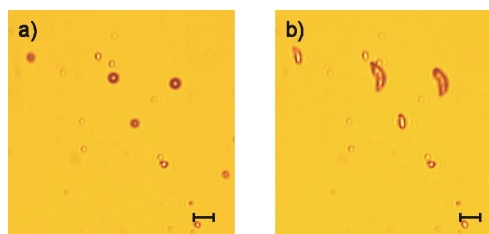


Fig. 4. Top view of photomechanical shape change of mixed microspheres of BMAB and m-MTDATA upon grazing-angle irradiation with s-polarized laser beam. Incident beam comes from the right side of the image. a) Before irradiation, b) After 60 min irradiation. Scale bar: 10 µm.

In contrast to s-polarized laser beam, grazing-angle irradiation with 488 nm p-polarized one was found to induce transport of the mixed microspheres on the substrate away from the light source, accompanied by some deformation of their shapes as shown in Fig. 5. The result was also similar to those for BFIAB and PBAB microspheres [22].

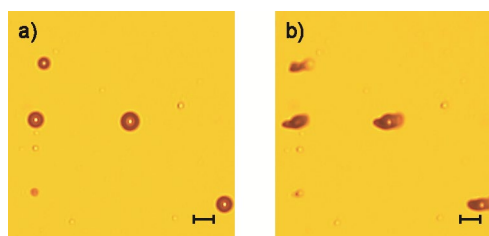


Fig. 5. Top view of photomechanical transport of mixed microspheres of BMAB and m-MTDATA upon grazing-angle irradiation with p-polarized laser beam. Incident beam comes from the right side of the image. a) Before irradiation, b) After 60 min irradiation. Scale bar: 10 µm.

For gain further information, we investigated the photomechanical motion viewing from the side. As shown in Fig. 6, the mixed microspheres of

BMAB and m-MTDATA were found to deform upon grazing-angle irradiation with p-polarized beam and roll to transfer away from the light source. Such photomechanical rolling motion was quite similar to those observed for single BFIAB and PBAB microspheres [22] and could be explained as follows. When the microsphere was irradiated with p-polarized laser beam at the grazing angle, photomechanical deformation took place in the direction parallel to the polarization direction of the incident beam to move to both upper and lower sides. With regard to upper side, molecules fall back in the direction of the original sphere like the curved horn formation observed when using s-polarized beams. With regard to lower side, molecules reached to the substrate and then push against it, generating driving force to exhibit rolling motion to transport. After such process, the newly revealed surface was irradiated and the same process was repeated.

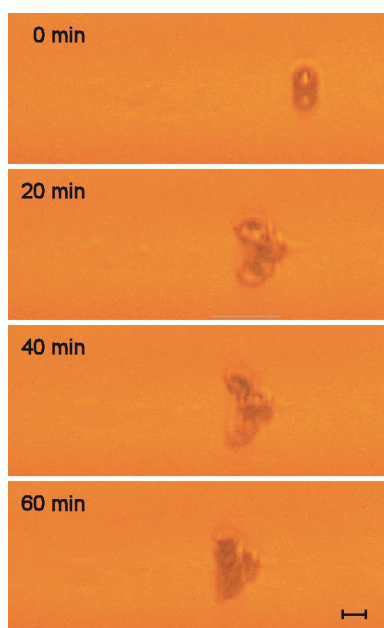


Fig. 6. Side view of photomechanical rolling motion of a mixed particle of BMAB and m-MTDATA upon grazing-angle irradiation with p-polarized laser beam. Incident beam comes from the right side of the image. Scale bar: 10 μm .

Fig. 7 shows the size dependence of the transporting speed upon grazing-angle irradiation with p-polarized laser beam. As well as single PBAB and BFIAB glass microspheres [22], the average speeds during 60 min irradiation were found to increase with decreasing the size of the mixed microspheres of BMAB and m-MTDATA. Regarding single BMAB particles, such

photomechanical transport was scarcely observed maybe due to relatively low T_g of BMAB. Thus, increasing in T_g of the material by mixing with m-MTDATA played an important role for photomechanical behaviors of the microspheres. In addition, it was suggested that not only BMAB but m-MTDATA molecules also moved in the mixed particles upon irradiation. Fig. 7 indicated that the average transport speeds of mixed microspheres were similar to those for PBAB microspheres rather than for BFIAB microspheres. In fact, average speeds for BFIAB, PBAB, and the mixed microspheres with diameter of 5-10 μm were 0.45, 0.14, and 0.18 $\mu\text{m min}^{-1}$, respectively. It was suggested that the higher T_g of the material was favorable for photoinduced transport probably because the higher viscosity of the material upon irradiation could produce larger mechanical power to push the substrate. Thus, the T_g of the material was suggested to be an important factor in characterizing its photomechanical behavior.

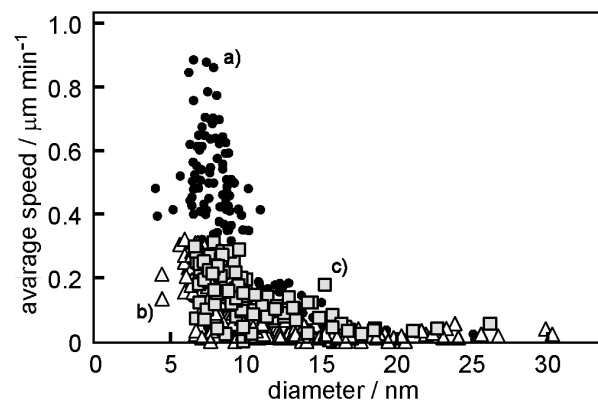


Fig. 7. Dependence of the average transport speed on diameter of the microsphere before irradiation. a) circle: BFIAB, b) triangle: PBAB, c) square: mixture of BMAB and m-MTDATA.

4. Conclusion

We have investigated the fabrication of microparticles of the single BMAB and the mixture of BMAB and m-MTDATA on a substrate and their photomechanical behaviors upon grazing-angle irradiation. Whereas microdomes were obtained for single BMAB, microspheres were fabricated on a glass substrate for the mixture of BMAB and m-MTDATA by casting their aqueous suspension onto a substrate. Although dome-shaped particles of single BMAB did not show so much obvious photomechanical behaviors, the mixed glass microspheres of BMAB and m-MTDATA exhibited photomechanical shape

changes and rolling motions upon grazing-angle irradiation with s- and p-polarized laser beams, respectively, similar to those observed for single BFIAB and PBAB microspheres. It was suggested that the increasing in Tg of the material by mixing with m-MTDATA into BMAB played an important role for fabrication of microspheres and their photomechanical behaviors.

Acknowledgement

This work was partly supported by JSPS KAKENHI Grant Number JP22K05248 and Izumi Science and Technology Foundation (2019–J–009).

References

1. Y. Yu, M. Nakano, and T. Ikeda, *Nature*, **425** (2003) 145.
2. Y. Yu and T. Ikeda, *Angew. Chem. Int. Ed.*, **45** (2006) 1378.
3. S. Kobatake, S. Takami, H. Muto, T. Ishikawa, and M. Irie, *Nature*, **446** (2007) 778.
4. P. Rochon, E. Batalla, and A. Natansohn, *Appl. Phys. Lett.*, **66** (1995) 136.
5. D. Y. Kim, S. K. Tripathy, L. Li, and J. Kumar, *Appl. Phys. Lett.*, **66** (1995) 1166.
6. M. Yamada, M. Kondo, J. Mamiya, Y. Yu, M. Kinoshita, C. J. Barret, and T. Ikeda, *Angew. Chem. Int. Ed.*, **47** (2008) 4986.
7. X. Lu, S. Guo, X. Tong, H. Xia, and Y. Zhao, *Adv. Mater.*, **29** (2017) 1606467.
8. T. Tanino, S. Yoshikawa, T. Ujike, D. Nagahama, K. Moriwaki, T. Takahashi, Y. Kotani, H. Nakano, and Y. Shirota, *J. Mater. Chem.*, **17** (2007) 4953.
9. H. Utsumi, D. Nagahama, H. Nakano, and Y. Shirota, *J. Mater. Chem.*, **12** (2002) 2612.
10. D. Nagahama, H. Nakano, and Y. Shirota, *J. Photopolym. Sci. Technol.*, **21** (2008) 755.
11. H. Nakano, T. Takahashi, T. Kadota, and Y. Shirota, *Adv. Mater.*, **14** (2002) 1157.
12. H. Nakano, T. Tanino, T. Takahashi, H. Ando, and Y. Shirota, *J. Mater. Chem.*, **18** (2008) 242.
13. H. Nakano, T. Takahashi, T. Tanino, and Y. Shirota, *Dyes Pigm.*, **84** (2009) 102.
14. H. Nakano and M. Suzuki, *J. Mater. Chem.*, **22** (2012) 3702.
15. M. Suzuki and H. Nakano, *J. Photopolym. Sci. Technol.*, **25** (2012) 159.
16. H. Nakano, *J. Mater. Chem.*, **20** (2010) 2071.
17. H. Nakano, R. Ichikawa, and R. Matsui, *Micromachines*, **4** (2013) 128.
18. A. Kitano, R. Ichikawa, and H. Nakano, *Opt. Mater.*, **86** (2018) 51.
19. R. Ichikawa and H. Nakano, *RSC Adv.*, **6** (2016) 36761.
20. H. Nakano, R. Ichikawa, H. Ukai, and A. Kitano, *J. Phys. Chem. B*, **122** (2018) 7775.
21. M. Matsubara, H. Ukai, M. Kuragano, K. Tokuraku, and H. Nakano, *Chem. Lett.*, **51** (2022) 493.
22. H. Nigorikawa and H. Nakano, *Chem. Lett.*, **51** (2022) 1150.

Measurement of Liquid Film Thickness Distribution Formed on a Two-fluid Jet Sprayed Surface Using a Fiber Optic Probe

Shinsuke Watanabe¹, Yuki Mizushima², Hiroki Takahashi³
Satomi Hamada³, Masayoshi Imai³, and Toshiyuki Sanada^{2*}

¹ Graduate School of Integrated Science and Technology, Shizuoka University, 3-5-1 Johoku, Naka-ku, Hamamatsu, Shizuoka 432-8561, Japan

² Department of Mechanical Engineering, Shizuoka University, 3-5-1 Johoku, Naka-ku, Hamamatsu, Shizuoka 432-8561, Japan

³ Ebara Corporation, 4-2-1 Honfujisawa, Kanagawa, 251-8502, Japan

*sanada.toshiyuki@shizuoka.ac.jp

In single-wafer wet processes, the surface etch rate is strongly dependent not only on the concentration and temperature of the chemicals but also on the structure of the formed liquid film flow. The two-fluid jet method, widely used in the single wafer process, will cause a different liquid film structure from the single liquid jet. In this study, we investigated the liquid film structure formed by a two-fluid jet where many droplets are sprayed with a high-velocity air stream. Using a fiber-optic probe, we measured the liquid film thickness distribution by changing the air and water flow rate. The liquid film just below the irradiation is thicker than the single liquid jet and rapidly decreases around it, and circular hydraulic jumps occur at a greater distance. The jump radius varied significantly depending on the air flow rate and the temperature of the liquid. The different liquid film structure formed by the two-fluid jet differs in the areas that are just below the irradiation and hydraulic jump, expected different chemical reactions occur.

Keywords: Cleaning, Two-fluid jet, Liquid film thickness, Optical fiber

1. Introduction

In the wet processes of semiconductor manufacturing, such as resist removal and cleaning, the surface etch rate is the most important parameter and must be accurately predicted. In the semiconductor manufacturing process, which has changed from a batch type to a single wafer type [1], the surface etch rate depends not only on the concentration and temperature of the chemical solution but also on the thickness and velocity distribution of the liquid film on the wafer surface [2-5], so it is necessary to clarify the flow conditions on the wafer surface. Although the liquid film structure on the wafer surface has been well investigated for single liquid jet flows [6-8], the liquid film structure formed on the sprayed surface for two-fluid jets needs to be clarified. This study investigated the liquid structure of liquid and gas

mixture sprayed surfaces [9-11].

The surface etch rate on a rotating wafer has been investigated for wafer rotation speed and chemical properties. It is known to vary with rotation speed, temperature, flow rate, flow velocity, and viscosity. Staudegger et al. [12] show that the etch rate on the outside of the wafer only dominates the wafer rotation speed because the chemical flow is almost exclusively in the direction of rotation. On the other hand, the area directly under the jet shows a high etch rate and depends on various parameters. For example, since fluid turbulence is directly related to the etch rate under the jet, changing the velocity distribution of the fluid inflow causes a large change in the etch rate [13]. The two-fluid jet method, widely used in single wafer processing, mixes air and water and injects them, so the surface liquid film structure is expected to be very different from

that of a single liquid jet.

In this study, we investigated the liquid film structure formed on the jetting surface using an optical fiber probe [14-16] to improve the cleaning performance of the two-fluid jetting method. This study investigates the distribution of liquid film thickness formed by a two-fluid jet with controlled air and water flow rates and compares the liquid film thickness formed on the surface of a single liquid jet. We compare the film structure from the point of circular hydraulic jumps estimated based on the continuity equation [17] and the velocity boundary layer thickness of the liquid film flow. We especially compared the locations where the predicted circular jumps occur. As a result, the liquid film immediately below the two-fluid jet was thicker than that of the one-fluid jet. The film thinned rapidly around the impinging region, resulting in a possible liquid film rupture of the inner structure of the hydraulic jump. The hydraulic jump radius varied greatly depending on the air flow rate and the fluid temperature.

2. Experimental

Figure 1 shows a schematic diagram of the experimental setup. We set a 150 mm diameter aluminum circular disk placed 7 mm vertically downward from the exit of an air nozzle with a 3.2 mm outlet diameter. We measured the formed liquid film thickness by the two-fluid jet with an optical fiber probe placed at the center of the aluminum plate. The two-fluid jet was generated by mixing water with high-speed air flow from an upstream air tank at the nozzle. We controlled the air and water flow rates by using regulators and valves downstream of the compressor and measured the flow rate with a flow meter.

Figure 2 shows the optical system for measuring the liquid film. We emitted a laser light from an optical fiber and measured the intensity of the reflected light from the gas-liquid interface to determine the thickness of the liquid film. The laser power connected to the fiber-optic probe is 10 mW, and the input light is split into two at a 50:50 split ratio by a 2×2 coupler. The light is emitted from the end face of the probe into the liquid phase and then reflected at the gas-liquid interface where the refractive index difference is large. We use a photodiode and recorder to record the intensity I of the reflected light returning to the probe.

We conducted calibration experiments to clarify the relationship between the reflected light intensity I and the liquid film thickness. Figure 3 shows the

results of the calibration experiment. The results of liquid film thickness distribution measurements were calculated based on the results of this calibration experiment.

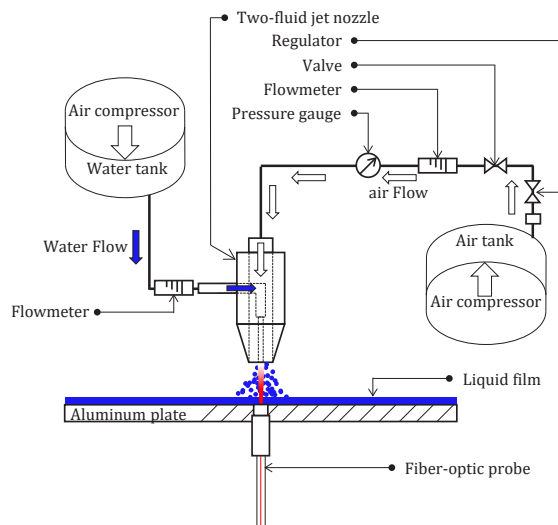


Fig. 1. Schematic diagram of the experimental apparatus.

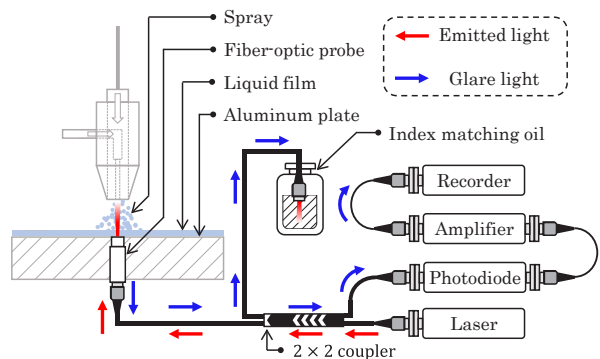


Fig. 2. Schematic diagram of optical system.

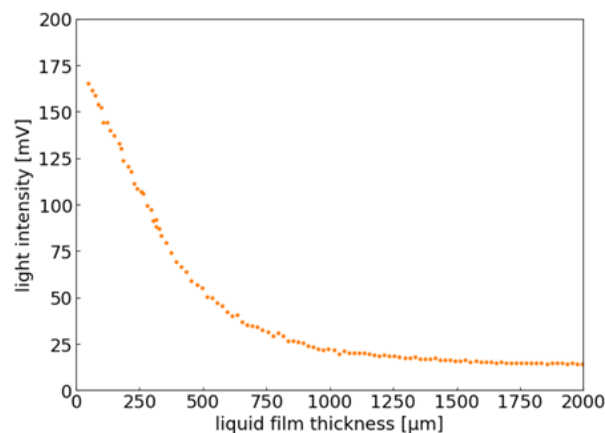


Fig. 3. Calibration curve for intensity I and film thickness of fiber-optic probes.

We performed a series of experiments for a constant water flow rate of 200 mL/min and four air flow rates of 50, 75, 100, and 125 L/min. For each set of experiments, the liquid film thickness was measured at 75 radial positions at 1 mm intervals from just below the nozzle to the edge of the aluminum disk. We measured the film thickness with a recording time of 1 s and a sampling rate of 100 kHz.

3. Results and discussion

3.1. Different air flow rates.

Figure 4 shows a typical experimental result of averaged film thickness distribution. The liquid film thickness below the nozzle shows about 200 μm, regardless of the liquid flow rate, and the film increases rapidly at a certain position. This is a circular hydraulic jump. The jump radius increases with increasing air flow rate.

To evaluate the distribution of liquid film thickness formed on the two-fluid jetting surface, we compared it with the theoretical model of a liquid film formed on the liquid jetting surface. The liquid film thickness h profile formed on the surface of a liquid jet with a circular hydraulic jump can be estimated based on the continuity equation [17],

$$h = \frac{q}{2\pi Rv} = \frac{a^2}{8R} . \quad (1)$$

Here q , R , v , and a are the water flow rate, jump radius, radial velocity, and jet diameter, respectively. Note that the liquid film distribution estimated for this inviscid fluid is thinner than that for a normal viscous fluid, i.e., a fluid developing a boundary layer.

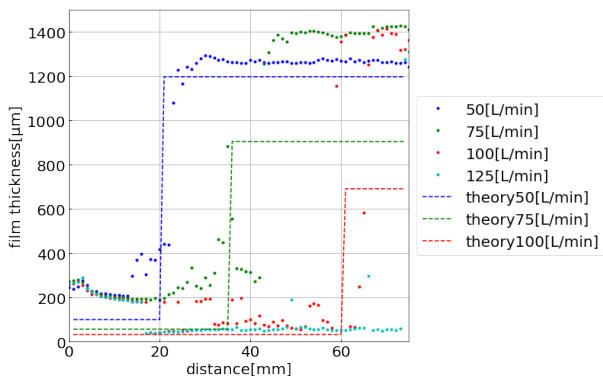


Fig. 4. Time averaged film thickness distribution formed by two-fluid jets with a comparison of the theoretical model.

By comparison with the theory, a thick film is formed just below the nozzle for all airflow conditions. The high-speed air flow ejected from the nozzle stagnates in the stagnation zone near the wall and is then deflected to the wall jet. This effect results in a thicker liquid film just below the nozzle. On the other hand, the film thickness at a position far enough from the nozzle diameter becomes thinner due to the high-speed airflow and approaches the thickness formed during a single liquid jet impact. This result indicates that the liquid film becomes very thin around the jet rather than directly under it, indicating the need for caution for the rupture of the film.

3.2. Different liquid temperatures.

Next, we discuss the liquid temperature effects on the liquid film structure. We performed additional experiments with a 50 °C temperature liquid. Figure 5 shows the measured liquid film thickness distribution with an airflow rate of 50 L/min. The figure shows that the hydraulic jump radius increases with the liquid temperature.

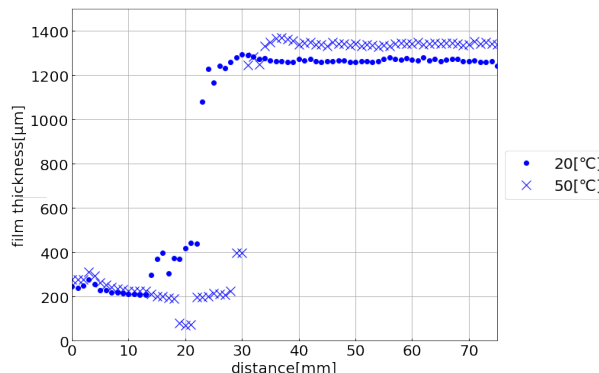


Fig. 5. Liquid film thickness profiles for different water temperatures (20 and 50 °C).

One model proposes that a hydraulic jump occurs when the boundary layer reaches the thickness of the liquid film [17]. The boundary layer thickness δ assuming that the horizontal velocity v_0 is equal to the impinging velocity of the jet can be calculated as follows [17],

$$\delta \propto \sqrt{\frac{vr}{v_0}} . \quad (2)$$

Here v and r are the kinematic viscosity and radial distance. The kinematic viscosity of 50°C water is almost half of 20°C water, so the boundary layer thickness is about 1.4 times greater for the 20°C

water at the same radial position. This is quantitatively consistent with the difference in jump radius position shown in Figure 5.

4. Conclusion

The liquid film thickness formed by the two-fluid jet is an important parameter concerning the etch rate. However, the knowledge about liquid film structures formed by many droplets with airflow is limited compared to liquid film structures by single liquid jets. Using a fiber-optic probe, we measured the liquid film thickness distribution formed by a two-fluid jet. We found the thicker liquid film formed by the two-fluid jet just below the nozzle due to a stagnant region in the high-speed airflow. Moreover, the liquid film thickness around the impingement region approaches the inviscid liquid jet impact. We also confirmed the formation of circular hydraulic jumps as in liquid jets. The radius of the hydraulic jump increased with increasing air flow rate. Therefore, care is needed for the rupture of the thin liquid film inside the hydraulic jump. Furthermore, the liquid temperature also changes the jump radius because the viscosity is related to the velocity boundary layer thickness. We plan to investigate the etch rate on the two-fluid jet impingement surface and the liquid film thickness on a rotating disk.

References

1. T. Hattori, *ECS Trans.*, **25** (2009) 3.
2. H. Habuka, S. Ohashi, and T. Kinoshita, *Mater. Sci. Semicond. Process.*, **15** (2012) 543.
3. H. Habuka, K. Mizuno, S. Ohashi, and T. Kinoshita, *ECS J. Solid State Sci. Tec.*, **2** (2013) P264.
4. T. Oinoue, S. Saito, A. Okuyama, Y. Hagimoto, and H. Iwamoto, *Solid State Phenom.*, **282** (2018) 83.
5. T. Lin, M. Hu, O. A. Zargar, W. H. Lai, and G. Leggett, *IEEE Trans. Semicond. Manuf.*, **35** (2022) 332.
6. E. J. Watson, *J. Fluid Mech.*, **20** (1964) 481.
7. T. Azuma, and T. Hoshino, *Buletin of JSME*, **27** (1984) 2747.
8. J. W. Bush, and J. M. Aristoff, *J. Fluid Mech.*, **489** (2003) 229.
9. I. Kanno, N. Yokoi, and K. Sato, *ECS Proc.*, **35** (1998) 54
10. T. Sanada, and M. Watanabe, *J. Photopolym. Sci. Technol.*, **28** (2015) 289.
11. H. F. Okorn-Schmidt, F. Holsteyns, A. Lippert, D. Mui, M. Kawaguchi, C. Lechner, P. E. Frommhold, T. Nowak, F. Reuter, M. B. Piqué, C. Cairós, and R. Mettin, *ECS J. Solid State Sci. Technol.* **3** (2014) N3069.
12. E. Staudegger, M. W. Hofbauer, and H. J. Kruwinus, *J. Electrochem. Soc.*, **156**, (2009) H340.
13. K. Kaneko, A. Tamenori, N. Alleborn, and F. Drust. *ECS Trans.*, **2** (2007) 295.
14. K. Ohba, T. Origuchi, and Y. Shimanaka, *Proc. 4th Sensor Symposium*, (1984) 33.
15. K. Yamaguchi, T. Sanada, and Y. Mizushima, *Mechanical Eng. Lett.* **6** (2020) 00419.
16. Y. Mizushima, *IEEE Trans. Instrum. Meas.*, **70** (2021) 1.
17. Y. Brechet, and Z. Neda, *Am. J Phys.*, **67** (1999). 723.

Surface Modification of Fluoropolymers by Atomic Hydrogen

Akira Heya*, Hideo Otsuka, and Koji Sumitomo

*Department of Materials and Synchrotron Radiation Engineering, University of Hyogo,
2167 Shosha, Himeji, Hyogo 671-2280, Japan
heya@eng.u-hyogo.ac.jp

The reaction of atomic hydrogen with fluoropolymers was investigated to clarify mechanism of surface modification. The atomic hydrogens were generated by decomposition of H₂ gas on a heated W mesh. We call the surface-treatment atomic hydrogen annealing (AHA). As the AHA treatment time increased, chemical bonds in polytetrafluoroethylene (PTFE) was changed from -CF₂-CF₂- to -CH₂-CF₂-, -CHF-CF₂-, and CF₃ below 200 °C. In the fluoropolymer films containing O atoms, named FO, both F and O atoms reacted with atomic hydrogen, however, the F atoms were preferentially removed by AHA compared to O atoms. The comparison with thermal treatment indicates that the surface modification was not due to thermal effect but to chemical reaction of atomic hydrogen such as defluorination. From the comparison to soft X-ray irradiation, the AHA modifies the fluoropolymers without excess damage.

Keywords: Atomic hydrogen annealing, Surface modification, Fluoropolymers, Polytetrafluoroethylene

1. Introduction

Polymer materials are cheap, light, and flexible. Such materials are expected for use as substrates for next-generation flexible semiconductor devices [1,2]. Fluoropolymers such as polytetrafluoroethylene (PTFE) show many excellent properties such as high chemical resistance, high thermal resistance, low relative permittivity, and low dielectric loss tangent. A micro-fluidic device for the application to a micro-total analysis system (μ -TAS) using PTFE has been investigated. However, PTFE is difficult to modify and microfabricate due to its excellent chemical and thermal stability, and there are no reports of PTFE being applied to microchemical chips. In addition, the hydrophobicity of PTFE makes it difficult for liquid to flow in the channel. The modification and microfabrication of PTFE are important for the realization of PTFE-based devices and have been investigated using X-rays [3,4], electron beams [5], ions [6], and plasma [7].

Atomic hydrogens, in other words, hydrogen radicals, are generated by catalytic cracking reaction on a heated catalyst [8,9]. We proposed a

surface treatment method using the atomic hydrogen, named as atomic hydrogen annealing (AHA) [10-20]. In AHA, the hydrogen molecules are decomposed by the catalytic cracking reactions on the heated tungsten (W) catalyst placed near the sample. The decomposition efficiency of H₂ is much higher on heated catalyst surface than in gas phase such as plasma process [21]. The AHA method treats on a large area sample simply by spreading the catalyst widely without plasma damage.

The technique is applied to surface cleaning of carbon contamination [19,22] and native oxide [20,23] and photoresist removal [24-27]. In addition, the surface modifications of plastic substrates, namely, polyvinyl chloride (PVC) [11,19], polyethylene (PE) [11], polypropylene (PP) [11,19], polyethylene naphthalate (PEN) [13,19], and poly methyl methacrylate (PMMA) [28] have been investigated for controlling the surface properties. It was found that the surface modification depended on the constituent elements (halogen and oxygen atoms) of the polymer and the surface protrusion formation was realized by combination of the chemical reaction of atomic hydrogen (depletion of

oxygen and halogen atom and/or decomposition of main chain) and the enhancement of etching effect due to local heating [19]. However, the surface modification of PTFE using atomic hydrogen has never investigated.

In this study, the reaction of PTFE and fluoropolymers with atomic hydrogen was investigated from the change in the surface property. Fluoropolymer films containing oxygen were also used to investigate the difference in reactivity of atomic hydrogen toward C-F and C-O. The mechanism of surface modification was discussed by comparison with soft X-ray irradiation and thermal treatment.

2. Experimental

Commercial PTFE substrate (UNIVERSAL CO. LTD., $300 \times 300 \times 0.5$ mm in size) were used. The PTFE substrate was cut to 14×28 mm. In addition, to investigate the difference in reactivity of atomic hydrogen toward C-F and C-O, fluoropolymer films containing O atoms, named FO, were prepared on single crystal Si (c-Si) substrates. The FO films were obtained from a fluoride coating agent (Fluoro Surf, FG-3650C-20, FLUORO TECHNOLOGY) of 100 μ l using a spin coater at 1000 rpm for 30 s. The FO contains not only C, F atoms but also O atoms as C-OH and O=C-OH. The film thickness of FO was 4 μ m.

The AHA apparatus used in this study and the concept of AHA are shown elsewhere [19]. In AHA, the hydrogen molecules are decomposed on a heated catalyst (W mesh). A 55×55 mm² W mesh with a wire diameter of 0.03 mm and having 50 holes/inch was heated to 1700 °C by electrical heating in H₂ atmosphere. The applied voltage and current of W mesh were 12.1 V and 30.6 A, respectively. The flow rate of H₂ and gas pressure were 100 sccm and 30 Pa, respectively. The distance between the W mesh and the sample was 80 mm. The AHA treatment time (t_{AHA}) was varied. The temperature of PTFE surface was measured by a K-type thermocouple (TC) attached on a PTFE substrate by a polyimide film tape (Kapton tape, 3M). In the FO/c-Si substrate, the sample temperature was measured by a K-type TC attached on a c-Si substrate by a ceramic bond (ARON CERAMIC D, TOAGOSEI).

To compare the AHA with other method, the FO film was irradiated with soft X-rays at BL07A in synchrotron radiation facility NewSUBARU. The light source of BL07A is a 2.28 m undulator. The storage-ring energy was 1 GeV. The photon energy

incident on the sample was 550 eV corresponding to the O 1s orbital level of 532.5 eV. The beam size measured with a fluorescent plate on the sample surface was 7.5×7.5 mm. The storage-ring current was 350 mA. The experiments were carried out using a monochromator to select the photon energy, because other order harmonic lights are included with an undulator source without a monochromator. The irradiation time was 120, 600, 1800, and 3600 s. The pressure was 5×10^{-5} Pa during soft X-ray irradiation. The sample temperature was measured with a K-type thermocouple in contact with the Si substrate. Under all conditions, the maximum temperature was the same as 40 °C. Furthermore, the change in surface property of FO film by thermal treatment was carried out. The FO/Si substrates were heated at 140, 200, 250, and 300 °C for 1800 s in air.

The surface properties were evaluated using X-ray photoelectron spectroscopy (XPS; ULVAC, PHI 5000 VersaProbe). For wide XPS spectra, an energy step of 0.2 eV, a pass energy of 117.4 eV, a dwell time of 20 ms, and 5 repeats were used. For narrow XPS spectra of C 1s, O 1s, and F 1s, an energy step of 0.2 eV, a pass energy of 23.5 eV, a dwell time of 100 ms, and 10 repeats were used. For the XPS measurements, a neutralizer gun was used to suppress the charge.

3. Results and discussion

3.1. Surface modification of PTFE

The C 1s spectra of the PTFE subjected to AHA

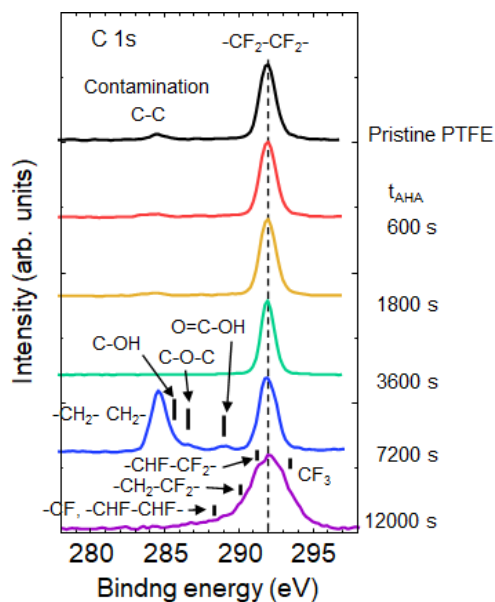
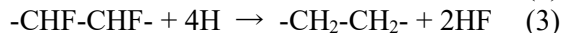
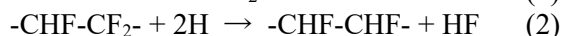
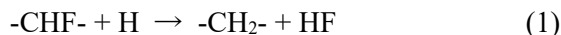


Fig. 1. C 1s XPS spectra of AHA-treated PTFE substrates.

were shown in Fig. 1. Before AHA, the C-C and -CF₂-CF₂- peaks were observed at 284.6 and 292.0 eV, respectively. The C-C peak was attributed to surface contamination of the PTFE substrate. At t_{AHA} of 1800, 2400, and 3600 s, the C-C peak disappeared. This shows that the carbon contamination was removed by chemical reaction with atomic hydrogen [19]. At a t_{AHA} of 7200 s, the C-C peak attributed to -CH₂- was clearly observed at 284.6 eV. Several small peaks were observed between the large peaks of -CH₂-CH₂- and -CF₂-CF₂-. These may be C-F related binding peaks. However, the small peaks were analyzed as C-O related binds because O 1s peak was observed. The origin of O is considered to be atmospheric oxygen or water vapor. Dangling bonds were formed by F abstraction during AHA and the C- bound to O after air exposure. Thus, the C-OH, C-O-C, and O=C-OH peaks were observed at 285.7, 286.9, and 289.0 eV, respectively. At a t_{AHA} of 12000 s, the -CF₂-CF₂- peak at 292.0 eV became broader due to the presence of -CHF-CF₂-, and CF₃ peaks at 291.3 and 293.5 eV, respectively. These changes were related to substitution of H to F and breaking of CF₂ bond by atomic hydrogen and a part of (-CF₂-CF₂)_n structure was changed to (-CHF-CF₂)_n, (-CF₂-CH₂)_n, (-CHF-CHF-)_n, and CF [29]. The changes from 7200 to 12000 s are thought to be caused by the following processes. First, F of PTFE surface is replaced by H. When -CHF is formed, the steric hindrance is smaller than elsewhere, so the following reactions are expected to occur preferentially.



In this case, both the -CH₂-CH₂- and -CF₂-CF₂- are detected (t_{AHA} of 7200 s). As the t_{AHA} increases further, -CH₂-CH₂- reacts with H and is desorbed as CH₄. In this case, -CH₂-CH₂- decreases and other CHF-related peaks appear as the terminal group increases (t_{AHA} of 12000 s).

The t_{AHA} dependences of peak area ratio of CF/CF₂ and CF₃/CF₂ estimated from decomposition of C 1s spectra are shown in Fig. 2. In this case, the area ratio was estimated from peak fitting of CF, CF₂, and CF₃ at 291.3, 292.0, and 293.5 eV in C 1s, respectively. At the t_{AHA} of 12000 s, small peaks on the low energy side were included as CF. As the t_{AHA} increased to 1800 s, the CF/CF₂ and CF₃/CF₂ increased. The t_{AHA} dependence of CF/CF₂ was related to reaction of CF₂ to CHF. In addition, the CF₃ formation occurred by breaking of main chain of -CF₂-CF₂- by atomic hydrogen. Furthermore, the CF/CF₂ and CF₃/CF₂ decreased as t_{AHA} increased to 7200 s. The tendency was related to the change from CF₂ to CH₂. The breaking of the main chain of -CF₂-CF₂- increased both CF/CF₂ and CF₃/CF₂ from 0.03 to 0.36 and CF₃/CF₂ from 0.06 to 0.31 at 12000 s.

3.2. Surface modification of FO (fluoropolymer containing oxygen)

The difference in reactivity of atomic hydrogen toward C-F and C-O was investigated using FO

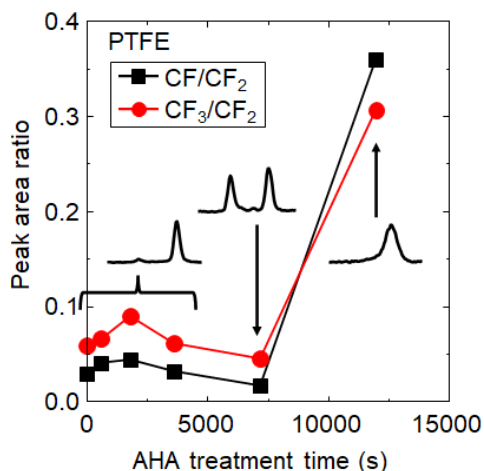


Fig. 2. Peak area ratio of CF/CF₂ and CF₃/CF₂ in PTFE as a function of t_{AHA}. The insets show schematic of the C 1s spectra.

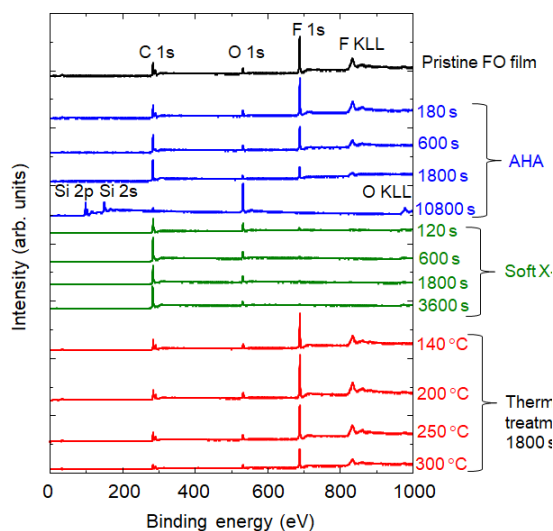


Fig. 3. XPS wide spectra of the pristine FO film, AHA-treated, soft X-ray irradiated, and thermal treated FO films.

film. The surface cracks and color change were visually observed in FO irradiated with soft X-rays. The XPS wide spectra of the pristine FO, the FO films subjected to AHA, soft X-ray irradiated, and thermal treated FO films are shown in Fig. 3. From the XPS wide spectra, the intensity of F 1s peak was decreased by AHA. At a t_{AHA} of 10800 s, the Si 2s and 2p peaks were observed. This indicates that the FO film on c-Si was etched by atomic hydrogen. The etching rate was estimated at last 1.9 nm/s. Although the O 1s peaks remained even at 3600 s, the F 1s peaks disappeared even at 120 s after soft X-ray irradiation. Furthermore, the wide spectra showed little change due to thermal treatment even at 300 °C.

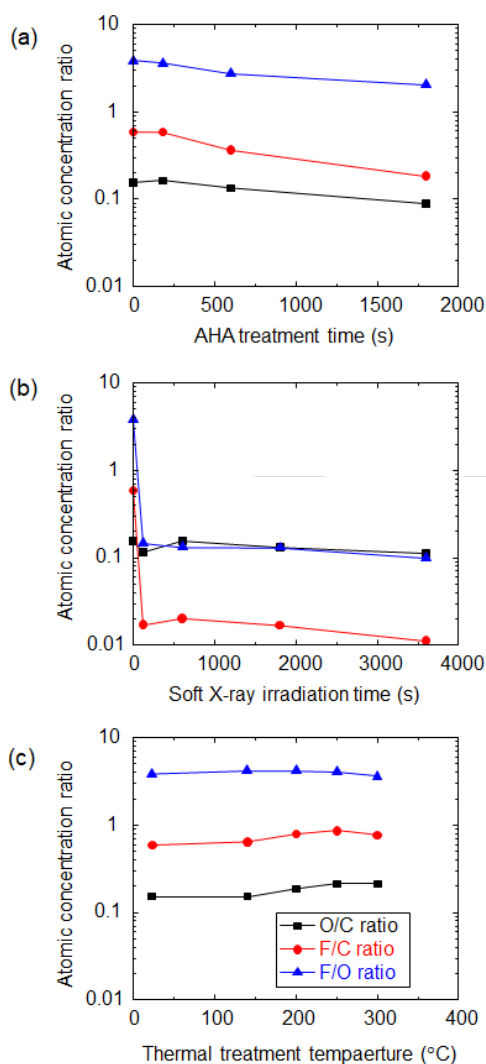


Fig. 4. F/O, O/C, and F/O ratios of the FO. (a) AHA treatment time dependence. (b) Treatment time dependence of soft X-ray irradiation. (c) Thermal treatment temperature dependence.

To discuss the chemical reaction of FO, the atomic concentrations were estimated from the peak areas of C 1s, F 1s, and O 1s. The F/O, O/C, and F/O ratios of the FO are shown in Fig. 4. The F/O, O/C, and F/O ratios decreased with increasing t_{AHA} . Although both F and O atoms react with atomic hydrogen, the F atoms are preferentially removed by AHA compared to O atoms from the decrement of F/O ratio.

In the soft X-ray irradiation, the F/O ratio decreased to below 0.02 even at 120 s. On the other hand, the O/C ratio was not decreased by soft X-ray irradiation. The F/C ratio of FO film subjected to soft X-ray irradiation was smaller than that subjected to AHA. However, the O/C ratio of the FO film subjected to soft X-ray irradiation was slightly larger than that subjected to AHA.

In the thermal treatment, the O/C, F/C, and F/O ratios were not changed at 140 °C. This temperature is the saturated sample temperature during AHA at 1800 s. This indicates that the removal of F and O atoms from FO film is due to a chemical reaction rather than a thermal effect. The O/C and F/C ratios were slightly increased with increasing treatment temperature above 200 °C. It was considered that O atoms in the FO were desorbed as CO and or CO₂ by high thermal treatment. The F/C is thought to have increased because of the simultaneous desorption of C and O atoms.

To further investigation the reaction, the C 1s, F 1s, and O 1s spectra are shown in Fig. 5. All the treatment time was 1800 s. The C-OH, O=C-OH, CF, CF₂, and CF₃ peaks in the C 1s spectra were reduced by AHA. However, the CF₂ and O=C-OH peaks

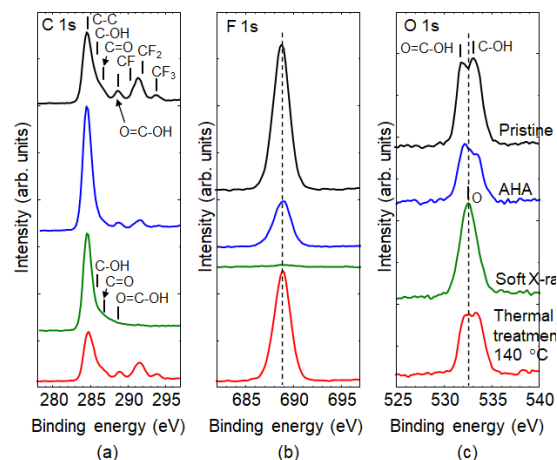


Fig. 5. C 1s (a), F 1s (b), and O 1s (c) spectra of the pristine FO, AHA-treated, soft X-ray irradiated, and thermal treated FO films. The treatment time was 1800 s.

remained after AHA. In contrast, the C-F related peaks were reduced by soft X-ray irradiation. Although the O=C-OH peak decreased, the C-OH and C=O bond remained after soft X-ray irradiation. The O=C-OH interacted more strongly with soft X-rays than C-OH and C=O. The F 1s peak intensity significantly decreased and full width at half maximum (FWHM) increased from 2.0 to 3.9 due to soft X-ray irradiation in contrast to pristine FO film. Two obvious components were detected in the O 1s spectra of the pristine, AHA-treated, and thermal-treated FO films, attributed to O=C-OH and C-OH [30]. In the soft X-ray irradiation, the single component was detected. This indicates that the O=C-OH is more easily removed in soft X-ray irradiation. The C 1s, F 1s and O 1s spectra were not

changed by thermal treatment at 140 °C.

The C 1s peak in the pristine GO was decomposed to C-C, C-OH, C=O, O=C-OH, CF, CF₂, and CF₃ bonds at 284.6, 285.6, 286.6, 287.2, 288.8, 291.1, 291.8, and 293.8 eV, respectively. Normalized area ratio and FWHM of each bond peaks as a function of t_{AHA} are shown in Fig. 6. The C-O and C-F related bonds decreased with increasing t_{AHA} . For the C-O related bonds, the O=C-OH was preferentially removed compared to the C-OH, C-O-C, and C=O. For the C-F related bonds, the CF and CF₃ bonds was preferentially removed compared to the CF₂. The normalized C-C peak area increased to 1.7. The FWHM of most O and F related bonds decreased with increasing t_{AHA} . This implies that the order of polymer molecules is improved during the process of removal of O and F atoms from FO due to atomic hydrogen. Alternatively, selective etching of low-density region, which is expected to be highly reactive with atomic hydrogen, may be occurring.

The dependences of soft X-ray irradiation time on the normalized peak area and FWHM are shown in Fig. 7. The C=O peak area changed drastically, but the C=O peak was too small to be accurately separated from the C 1s spectra. Therefore, further explanation is omitted. It was found that O=C-OH, C-OH, and C-O-C were more likely to be etched in that order. In contrast to AHA, the FWHM and fluctuation of the C-O related bonds was larger. The process of F abstraction by soft X-ray irradiation was shown to reduce the order of polymer molecules due to irradiation damage.

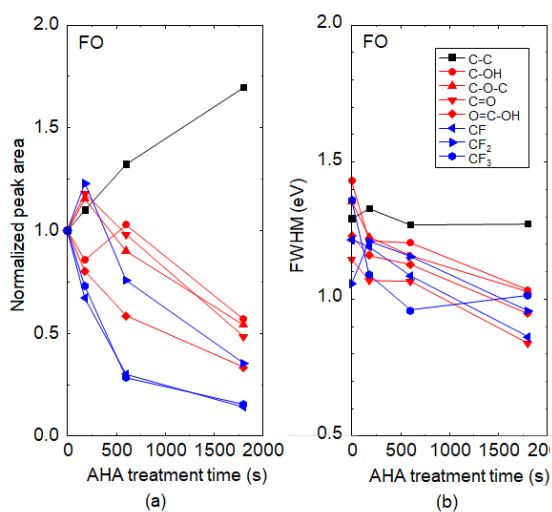


Fig. 6. Normalized area ratio (a) and FWHM (b) of each bond in FO as a function of t_{AHA} .

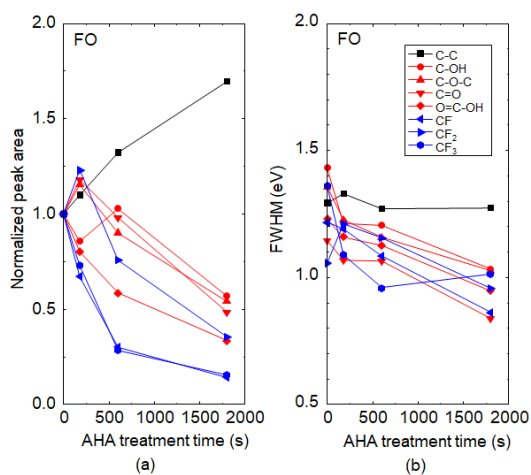


Fig. 7. Normalized area ratio (a) and FWHM (b) of each bond in FO as a function of soft X-ray irradiation time.

3.3 Reaction of atomic hydrogen with PTFE and FO

First, the mechanism of surface modification of PTFE is discussed in terms of the bond dissociation energy and thermal properties of PTFE. The bond dissociation energies of C-C and C-F are 3.8 and 4.7 eV, respectively [31]. It is expected that the C-F bond is more difficult to break because of its higher binding energy, but in fact, the C-F bond was preferentially broken and desorbed. This is because the bonds between C atoms in main chain are protected by F atoms covering the gaps. In AHA, the atomic hydrogen first causes a F depletion reaction, followed by a reaction affecting the C-C bond.

The glass transition temperature, heat resistance temperature, and melting point of PTFE are 115, 260, and 327 °C, respectively. The surface temperatures of PTFE at 600, 180, 3600, 7200, and 12000 s were 110, 140, 170, 190, and 200 °C, respectively. Although the surface properties of

PTFE were changed at 7200 and 12000 s, the difference in surface temperature was small as 10 °C. The large change in surface properties between 7200 and 12000 s was due to difference in treatment time, not surface temperature.

The changes in C 1s spectra indicate that the atomic hydrogen reacts with F of -CF₂- chains and some F atoms are removed by AHA. The speculated reactions of F removal from -CF₂- are as follows.



The surface modification was accomplished by the abstraction reaction of F with atomic hydrogen. In H₂ plasma treatment, the F abstraction reaction by hydrogen has been reported [7].

Next, the mechanism of surface modification of FO by atomic hydrogen is discussed in comparison with soft X-ray irradiation. The C-C bonds of main chain of FO are protected by the surrounding F elements as in PTFE, but are not completely protected by the C-OH and O=C-OH groups added to provide wettability. The bond dissociation energies of C-O, C=O, and O-H are 3.7, 7.6, and 4.8 eV, respectively [32]. As mentioned above, in AHA, the CF and CF₃ bonds were preferentially removed compared to CF₂ bond due to steric hindrance as well as PTFE. This may be because CF and CF₃ are located at terminal or sites that are not affected by steric hindrance. The reactivity of each bond with atomic hydrogen was independent of dissociation energy. In the soft X-ray irradiation, X-rays penetrate deeper than the depth of the XPS measurement, so there is no steric barrier effect. In addition, the transmission of soft X-ray depends more strongly on the elements than on the chemical bonds. The 550 eV was used to excite the electrons in O 1s orbital. The C-O related bonds were expected to be broken by electron excitation, while C-F bonds are preferentially removed by soft X-ray irradiation. Details are under consideration. The surface cracks and color change were visually observed in FO subjected to AHA in comparison with soft X-rays. It is shown that AHA modifies the FO film without excess damage.

4. Conclusion

The surface modification of PTFE and FO was realized by AHA at low temperature. In the surface modification of PTFE, it was shown that chemical reaction with atomic hydrogen depended on the molecular structure in which F surrounds the main chain of carbon. From the comparison to soft X-ray

irradiation, the AHA modifies the fluoropolymers without excess damage.

Acknowledgement

This work was supported in part by a research grant from the Mazda Foundation and JSPS KAKENHI Grant Number JP22K04877.

References

1. G. Shen, *Prog. Mater. Sci.* **31** (2021) 872.
2. B. Zazoum, K. M. Batoo, and M. A. A. Khan, *Sensors* **22** (2022) 4653.
3. Y. Zhang, T. Katoh, M. Washio, H. Yamada, and S. Hamada, *Appl. Phys. Lett.* **67**, 872 (1995).
4. Y. Haruyama, Y. Kato, K. Kanda, S. Matsui, T. Ideta, H. Ishigaki, *Radiat. Phys. Chem.* **75** (2006) 479.
5. Y. Nishi, M. Uyama, H. Kawazu, H. Takei, K. Iwata, H. Kudoh, and K. Mitsubayashi, *Mater. Trans.* **53** (2012) 1657.
6. M. Schulze, K. Bolwin, E. Gülzow, and W. Schnurnberger, *Fresenius J. Anal. Chem.* **353** (1995) 778.
7. M. E. Ryan, and J. P. S. Badyal, *Macromolecules*, **28** (1995) 1377.
8. I. Langmuir, *J. Am. Chem. Soc.* **34** (1912) 1310.
9. I. Langmuir and G.M.J. Mackay, *J. Am. Chem. Soc.* **36** (1914) 1708.
10. A. Heya, A. Masuda, and H. Matsumura, *Appl. Phys. Lett.*, **74** (1999) 2143.
11. A. Heya and N. Matsuo, *Jpn. J. Appl. Phys.*, **46** (2007) 3545.
12. A. Heya and N. Matsuo, *Jpn. J. Appl. Phys.*, **46** (2007) L709.
13. A. Heya and N. Matsuo, *Jpn. J. Appl. Phys.*, **47** (2008) 266.
14. A. Heya and N. Matsuo, *IEICE Trans. Electron*, **E93-C** (2010) 1516.
15. A. Heya and N. Matsuo, *Jpn. J. Appl. Phys.*, **53** (2014) 058002.
16. A. Heya and N. Matsuo, *Thin Solid Films*, **625** (2017) 93.
17. A. Heya, S. Hirano, and N. Matsuo, *Jpn. J. Appl. Phys.*, **58** (2019) 068006.
18. A. Heya, T. Harada, M. Niibe, K. Sumitomo, T. Watanabe, *J. Photopolym. Sci. Technol.*, **33** (2020) 419.
19. A. Heya, K. Sumitomo *J. Photopolym. Sci. Technol.*, **34** (2021) 561.
20. A. Heya, K. Sumitomo, *J. Photopolym. Sci. Technol.*, **35** (2022) 351.
21. H. Umemoto, K. Ohara, D. Morita, Y. Nozaki, A. Masuda and H. Matsumura, *J. Appl. Phys.*, **91**

- (2002) 1650.
22. Y. Song, Q. Lu, and X. Gong, *Thin Solid Films* **612** (2016) 96.
23. A. Izumi, T. Ueno, Y. Miyazaki, H. Oizumi, and I. Nishiyama, *Thin Solid Films* **516** (2008) 853.
24. A. Izumi and H. Matsumura, *Jpn. J. Appl. Phys.* **41** (2002) 4639.
25. M. Yamamoto, H. Umemoto, K. Ohdaira, S. Nagaoka, T. Shikama, T. Nishiyama, H. Horibe, *J. Photopolym. Sci. Technol.*, **28** (2015) 303.
26. T. Maruoka, Yousuke Goto, Masashi Yamamoto, Hideo Horibe, Eiji Kusano, Kazuhisa Takao, Seiichi Tagawa, *J. Photopolym. Sci. Technol.*, **22** (2009) 325.
27. M. Yamamoto, H. Horibe, H. Umemoto, K. Takao, E. Kusano, M. Kase, and S. Tagawa, *Jpn. J. Appl. Phys.*, **48** (2009) 026503.
28. A. Matsuo, S. Takagi, T. Nishiyama, M. Yamamoto, E. Sato, and H. Horibe, *J. Photopolym. Sci. Technol.*, **31** (2018) 369.
29. J. Hubert, T. Dufour, N. Vandencastele, S. Desbief, R. Lazzaroni, and F. Reniers, *Langmuir* **28** (2012) 9466.
30. A. Stypczyńska, T. Nixon, and N. Mason, *Eur. Phys. J. D* **68** (2014) 333.
31. J. -P. Cheng, “*CRC Handbook of Chemistry and Physics*”, eds. J. R. Rumble, CRC Press, Boca Raton London New York (2021-2022) 102nd ed., p.9-73
32. A. A. Nada, P. Hauser, and S. M. Hudson, *Plasma Chem. Plasma Process.* **31** (2011) 605.

Synthesis and characteristics of maleic anhydride-based photopolymers with pendant POSS groups for negative tone photoresists

Haruka Onoda^{1,2}, Akira Takahashi¹, Nobuhito Ito², Kazuya Sato²,
and Atsushi Kameyama^{1*}

¹ Department of Chemistry, Kanagawa University,
3-27-1 Rokkakubashi, Kanagawa-ku, Yokohama City, Kanagawa 221-8686, Japan
² TAIYO INK MFG. CO., LTD., 900 Hirasawa, Ranzan-machi, Hiki-gun, Saitama
355-0215, Japan

*kameya01@kanagawa-u.ac.jp

We have developed the photopolymers with pendant POSS group based on the synthetic approach using maleic anhydride, which was reacted with 2-hydroxyethyl methacrylate to enable the simultaneous incorporation of methacryloyl group for photocuring and carboxy group for solubilization in aqueous developers. Several photopolymers were prepared with different methacrylate component, which affects the physical properties of the resulting photopolymers. Investigation of the characteristics of the obtained photopolymers in comparison with a control sample revealed that the pendant POSS group as well as incorporated alicyclic structure enhance the thermal, low dielectric, and photoresist properties.

Keywords: Polyhedral oligomeric silsesquioxane, Maleic anhydride, Negative tone photoresist, Dielectric properties, Polymer Film

1. Introduction

Photoresist polymers have become essential materials for electronic devices production [1,2]. Recent progress of those devices in processing ability and downsizing requires continuous improvement of the physical properties of the photoresist polymers such as thermal stability, mechanical properties, and electric properties. To this end, organic-inorganic hybrid polymers have been energetically explored as the promising candidate owing to its superior properties compared to the purely organic materials [3]. Polyhedral oligomeric silsesquioxane (POSS) is the widely used inorganic component that can be easily connected to organic structures with its Si atom [4–6], leading to better dispersion at the molecular level compared to blending inorganic fillers such as silica. The incorporated POSS groups contributes to not only good thermal and mechanical properties but also low dielectric constant [7–9], which is an important property for

the insulating materials such as solder resists and sealants.

While the POSS-containing polymers have been widely explored, the ones for photoresist materials are relatively limited. The POSS-containing photoresists have been mainly researched for 157 nm lithography because of the good transparency of POSS at 157 nm [10–12]. Other examples include photoresists for 193 nm [13–15] and 248 nm [16–19] lithography, while the study of g-/h-/i-line photoresists, which have long been commonly used in the industry, are further limited [20–22]. Chang and co-workers reported pendant POSS-containing copolymers for negative-tone photoresists using mercury short arc lamp [20,21]. These copolymers possess rich alcohol groups in addition to carboxy groups at the side chains, which enhanced the interchain interaction by hydrogen bonding to increase the rate of photopolymerization and thus increase the photosensitivity. On the other hand, such enriched

hydrophilicity could offset the merits given by incorporated POSS groups such as low dielectric constant and water absorption.

In this study, we designed the POSS-containing photoresist copolymers synthesized using maleic anhydride (MA), which can react with alcohols to produce carboxy group. Using the alcohols with polymerizable groups such as 2-hydroxyethyl methacrylate (HEMA) enables simultaneous incorporation of both photopolymerization ability and solubility in an aqueous developer to the resulting polymers while forming requisite minimum OH groups. We investigated the synthesis, physical properties, and photoresist properties of the MA-based POSS-containing photopolymers. In addition, the effect of incorporation of alicyclic structures, which would be beneficial for thermal properties with its rigidity and low dielectric properties with its non-polar structures, was also investigated.

2. Experimental Section

2.1. Materials

All solvents and reagents were purchased from Sigma-Aldrich, Wako Pure Chemical Industries, Tokyo Chemical Industry (TCI), or Kanto Chemical, and used as received unless otherwise noted. Liquid monomers were purified by distillation under reduced pressure before use. Methacryloylpropylisobutyl POSS (^tBuPOSSMA) was purchased from Hybrid Plastics and used as received. 2,2'-Azobis(isobutyronitrile) (AIBN) was purified by recrystallization from methanol before use.

2.2. Measurements

FT-IR spectra were recorded on a JASCO Inc. FT/IR4600 spectrometer. ¹H-NMR measurements were carried out at 298 K using acetone-*d*₆ or DMSO-*d*₆ as the solvent on a JEOL JNML-ECZ-400 or JNM-ECA-600 instrument. UV-vis spectra were recorded on JASCO Inc. V-650 spectrometer. Number- and weight-average molecular weights (*M*_n and *M*_w) were determined by gel permeation chromatography (GPC) with Tosoh HLX8220 using RI detectors calibrated with polystyrene standards, using DMF solution of 10 mM LiBr and 10 mM phosphoric acid as the eluent at a flow rate of 1 mL/min. Differential scanning calorimetry (DSC) analysis were performed on a Seiko EXSTAR DSC 6200 at heating and cooling rate of 10 °C/min under N₂ flow. Thermal gravimetric analysis (TGA) was performed on a Shimadzu DTG-60H at heating rate of 10 °C/min under air

atmosphere from 25 to 900 °C. Film thickness was measured on Bruker Dektak XT-E. Dielectric properties were calculated from capacitance measured at a frequency of 1 MHz using a Keysight technologies 4275A LCR meter.

2.3. Synthesis of P-1

Representative procedure is as follows (P-1a-2): To a 200 mL flask were added ^tBuPOSSMA (5.15 g, 5.46 mmol), styrene (St, 3.42 g, 32.8 mmol), MA (3.22 g, 32.8 mmol) and methyl methacrylate (MMA, 3.29 g, 32.8 mmol) followed by dry-Tetrahydrofuran (dry-THF, 52.0 mL, 2.0 mol/L) and AIBN (0.516 g, 3.12 mmol). The mixture was stirred under argon bubbling for 30 min and stirred 60 °C for 24 h. The product was reprecipitated in an ethanol (2.00 L). The precipitate was filtered, washed with ethanol, and dried under reduced pressure at room temperature to afford a white solid (11.1 g, 74%).

¹H-NMR (600 MHz, acetone-*d*₆) δ (ppm) : 7.84–5.81 (br, 5.00H), 4.32–3.42 (br, 2.32 H), 2.42–2.93 (br, 1.81 H), 2.65–1.47 (br, 7.85 H), 1.47–0.80 (br, 6.52 H), 0.80–0.24 (br, 2.40 H).

FT-IR (KBr, cm⁻¹): 2955 (ν_{C-H}), 1859 (ν_{as C=O, anhydride}), 1781 (ν_{s C=O, anhydride}), 1730 (ν_{C=O, ester}), 1455 (ν_{C-C, Ar}), 1114 (ν_{Si-O-Si}).

2.4. Synthesis of P-2

Representative procedure is as follows: (P-2a-2) To a 100 mL three-neck flask were added P-1a (5.55 g, containing 12.5 mmol of MA moiety) dissolving by dry-THF (12.5 mL, 1.0 mol/L) and immersed in an ice bath. To a dropping funnel were added HEMA (8.13 g, 62.5 mmol), 4-methoxy phenol (MEHQ, 0.16 g, 1.25 mmol) and triethylamine (TEA, 1.64 g, 16.3 mmol). The solution was stirred and dropped into a three-neck flask. The mixture was stirred under argon bubbling for 10 min and stirred room temperature for 6 h. The product was reprecipitated in a 0.05 mol% HCl aq. (750 mL) and stirred 1h. The precipitate was filtered, washed with water, and dried under reduced pressure at room temperature to afford a white solid (6.81 g, 95%).

¹H-NMR (600 MHz, acetone-*d*₆) δ (ppm) : 7.66-6.24 (br, 5.00H), 6.24-5.88 (br, 0.818 H), 5.88-5.43 (br, 0.754 H), 3.78-3.15 (br, 2.19 H), 3.15-2.40 (br, 2.18 H), 2.40-1.31 (br, 11.9 H), 1.31-0.779 (br, 5.75 H), 0.78-0.229 (br, 2.28 H).

FT-IR (KBr, cm⁻¹): 3267 (ν_{O-H}), 2953 (ν_{C-H, alkyl}), 1730 (ν_{C=O, ester}), 1637 (ν_{C=C, vinyl}), 1454 (ν_{C-C, Ar}), 1121, 1115 (ν_{Si-O-Si}).

2.5. Time-conversion study of photopolymerization of P-2

Representative procedure is as follows: Polymer solution was formulated by dissolving 100 mg of P-2a, 2.15 mg of 2-methyl-1-[4-(methylthio)phenyl]-2-morpholinopropan-1-one (Omnirad 907, 5.0 mol% for Methacryloyl group) in 1,4-dioxane (400 mg). All sample films were prepared by spin-casting of polymer solution on a CaF₂ plate. The photo-irradiation was performed using a Xe lamp (Eagle Engineering CX-04E) equipped with a band-pass filter (Asahi Spectra SC0451) at 310 nm with the intensity of 1.58 mW/cm² under N₂.

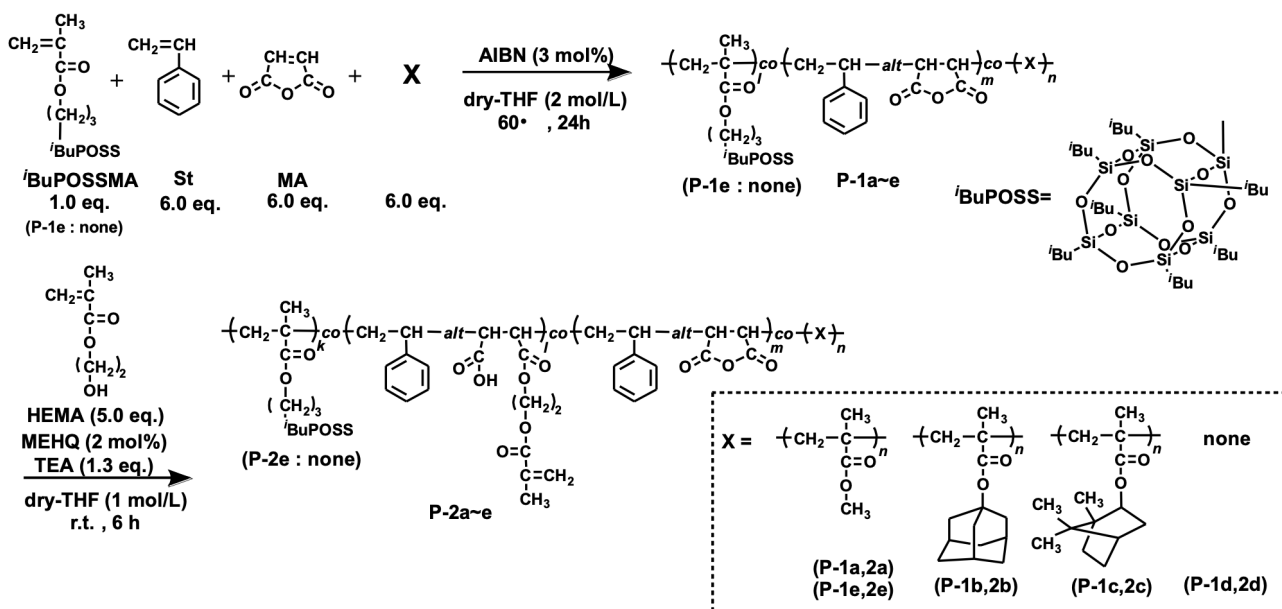
2.6. Photo-sensitivity study of P-2

Representative procedure is as follows: Polymer solution was formulated by dissolving 100 mg of P-2a, 2.15 mg of Omnirad 907 (5.0 mol% for Methacryloyl group) in 1,4-dioxane (400 mg). All sample films were prepared by spin-casting of polymer solution on a Si wafer. The photo-irradiation was performed using a Xe lamp (Eagle Engineering CX-04E) equipped with a band-pass filter (Asahi Spectra SC0451) at 310 nm with the intensity of 1.58 mW/cm² under N₂. P-2a and P-2e were developed by dipping in a 0.1 wt% Na₂CO₃ aq. at 25 °C for 60 sec. (P-2a) or 24 sec. (P-2e) and rinsed by water. P-2b~d were developed by dipping in a 1,4-dioxane/water (8/2, v/v) mixture at 25 °C for 18 sec. (P-2b), 40 sec. (P-2c), or 10 sec. (P-2d). Photo-sensitivity curve was determined by plotting the normalized film thickness after the development against exposure dose.

3. Results and discussion

3.1. Synthesis of MA-based pendant POSS-containing photopolymers

The targeted copolymers were synthesized by 2 steps according to Scheme 1. Prepolymers P-1a~c was first synthesized by radical copolymerization of ⁱBuPOSSMA, MA, and styrene (St) in combination with either methyl methacrylate (MMA) (P-1a), 1-adamantly methacrylate (ADMA) (P-1b), or isobornyl methacrylate (IBOMA) (P-1c). The copolymer with only ⁱBuPOSSMA, MA, and St (P-1d) and the one with MA, St, and MMA without POSS moieties (P-1e) were also prepared. The polymerization was carried out using AIBN as the initiator in dried THF at 60 °C for 24 h. The FT-IR spectra of the obtained copolymers showed the characteristic peaks of carboxylic anhydride at 1859 cm⁻¹ and 1781 cm⁻¹, confirming the incorporation of MA in the copolymer. P-1a~d showed Si-O-Si peak at 1114 cm⁻¹ attributed to the POSS moiety. ¹H-NMR of the copolymers revealed the MA composition of 29~41 mol%. ⁱBuPOSSMA composition was 2~3 mol% for P-1a~c and 7.1 mol% for P-1d. GPC analysis showed comparable molecular weight of P-1a~e around 10000 with a single peak top in either GPC profile. P-1 was next reacted with HEMA to produce P-2 with methacryloyl and carboxy groups. The addition reaction was carried out using triethylamine (TEA) as the base in dry-THF at r.t. FT-IR spectra of the products showed the C=C peak of methacryloyl group at 1637 cm⁻¹ and O-H peaks of the carboxy group at over 3200 cm⁻¹ region due to the addition of HEMA to the MA moieties in P-1. ¹H-NMR



Scheme 1. Synthesis of MA-based POSS-containing photopolymers.

Table 1. Synthesis of the photopolymers with pendant POSS, carboxy, and methacryloyl groups

Polym.	Yield (%)	Molar composition (wt%)					D.I. of HEMA ^{a)} (%)	Acid value ^{b)}	M_n (M_w/M_n) ^{c)}
		^t BuPOSS MA	St	MA + HEMA	MA	X			
P-1a-1	80	0.027 (21.0)	0.263 (22.2)	—	0.387 (30.7)	0.322 (26.1)	—	—	15500 (2.87)
P-1a-2	74	0.030 (22.2)	0.321 (26.6)	—	0.290 (22.6)	0.359 (28.6)	—	—	10600 (2.93)
P-1b	82	0.030 (16.7)	0.293 (17.7)	—	0.294 (16.8)	0.382 (48.9)	—	—	12200 (3.07)
P-1c	77	0.021 (12.5)	0.330 (21.4)	—	0.303 (18.4)	0.346 (47.7)	—	—	13300 (2.57)
P-1d	70	0.113 (54.4)	0.373 (19.8)	—	0.514 (25.8)	—	—	—	9220 (3.06)
P-1e	90	—	0.271 (28.1)	—	0.413 (40.4)	0.315 (31.5)	—	—	9590 (3.67)
P-2a-1	80	0.025 (16.9)	0.265 (19.4)	0.156 (25.1)	0.209 (14.4)	0.344 (24.2)	43	62	20500 (2.74)
P-2a-2	95	0.026 (15.9)	0.311 (21.2)	0.235 (35.0)	0.104 (6.68)	0.324 (21.2)	69	86	12000 (2.92)
P-2b	95	0.030 (14.5)	0.246 (13.2)	0.218 (25.5)	0.168 (8.49)	0.338 (38.3)	56	63	15600 (2.86)
P-2c	75	0.030 (14.8)	0.315 (17.0)	0.221 (26.2)	0.124 (6.31)	0.309 (35.6)	64	64	15200 (2.51)
P-2d	67	0.108 (45.6)	0.368 (17.1)	0.245 (25.0)	0.279 (12.3)	—	47	61	12100 (2.94)
P-2e	84	—	0.278 (22.9)	0.201 (36.2)	0.208 (16.1)	0.313 (24.8)	49	89	13900 (3.17)

a) Degree of introduction of HEMA to MA moieties determined by ¹H-NMR. b) Calculated milligrams of KOH required to neutralize the COOH group in 1 g of a sample. c) Estimated by GPC (RI, solvent : DMF, standard : PSt).

spectra of P-2 revealed the degree of introduction (D.I.) of HEMA to the MA moieties to be 43~69%. The above-described synthetic results are summarized in Table 1.

3.2. Characterization of MA-based POSS-containing photopolymers

Thermal and dielectric properties of the obtained photopolymers were next investigated. The results are summarized in Table 2. Physical properties of were characterized Thermal properties of P-2 were evaluated by thermal gravimetric analysis (TGA) and differential scanning calorimetry (DSC). The 5% weight loss temperature (T_{d5}) was in order of

Table 2. Thermal and dielectric properties of the photopolymers with pendant POSS, carboxy, and methacryloyl groups

Polymer	T_g ^{a)}	T_{d5} ^{b)}	D_k ^{c)}	D_f ^{c)}
P-2a-1	91	195	3.04	0.044
P-2b	118	212	2.75	0.035
P-2c	111	207	n.d.	n.d.
P-2d	103	204	3.19	0.043
P-2e	92	191	3.75	0.056

a) Determined by DSC (in N₂, 10 °C/min). b) 5% weight loss temperature (TGA, in air, 10 °C/min). c) Determined by LCR meter (1.00 MHz).

P-2b (212 °C) > P-2c (207 °C) > P-2d (204 °C) > P-2a-1 (195 °C) > P-2e (191 °C). The highest value of P-2b would be due to the rigid, alicyclic adamantyl group. P-2c with alicyclic isobornyl group and P-2d with rich MA composition also showed the good T_{d5} . DSC study revealed the glass transition temperature (T_g) of P-2 ranging from 91 °C to 118 °C. The order of T_g was same as T_{d5} , showing that the rigid alicyclic structures contributed to the thermal properties.

We next investigated the low dielectric properties, which are important factor particularly for recent high speed communication devices. P-2a-1 showed lower dielectric constant (D_k) of 3.04 and loss tangent (D_f) of 0.044 in comparison with P-2e ($D_k = 3.75$, $D_f = 0.056$), which is a non-POSS-containing control sample of P-2a. These results indicate that the pendant POSS group contributed to the low dielectric properties. P-2b, which possesses adamantyl group instead of methyl group in P-2a, showed further lower D_k (2.75) and D_f (0.035) than P-2a-1. The better properties of P-2b would stem from the adamantyl group, which possesses non-polar methylene and methine groups in addition to the rigid cage structure. These structural characteristics of adamantyl group are favorable for the low dielectric properties. Meanwhile, P-2d showed the

worst low dielectric properties among the herein tested samples. P-2d possesses the highest non-polar POSS composition, but the polar COOH composition is also highest for P-2d. Therefore, the large D_k and D_f values of P-2d would stem from the latter factor.

3.3. Photopolymerization and photoresist properties of MA-based POSS-containing photopolymers

The photo-polymerization properties of P-2 were evaluated by time-course FT-IR spectroscopy. P-2 films with 5 mol% of Omnirad 907 as the photoinitiator were prepared on a CaF_2 plate and irradiated by Xe lamp equipped with the band-pass filter that transmits *ca.* 290–470 nm. The C=C peak of methacryloyl group at 1636 cm^{-1} decreased as the irradiation (Fig. 1), indicative of the proceeding of the photo-curing reaction. The conversion of C=C functionality was plotted as a function of exposure dose (Fig. 2), which showed comparable reaction behavior for all P-2 samples. P-2d showed a bit slower reaction, possibly due to the relatively rigid backbone structure due to the rich *t*BuPOSSMA and MA compositions, which would limit the chain mobility to hinder the photopolymerization of the pendant methacryloyl groups. The photoresist properties of P-2 were investigated. The solubility of each P-2 was first checked to determine the development conditions. P-2a-2 and P-2e dissolved in alkaline aqueous

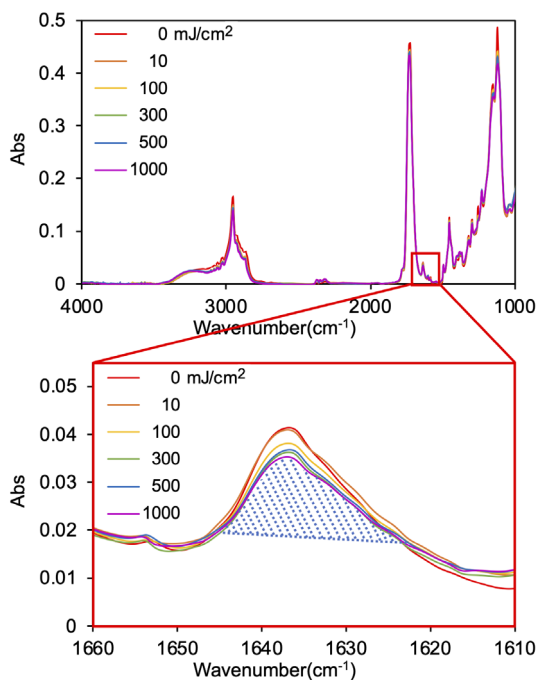


Fig. 1. Decrease of C=C peak in FT-IR spectra during the photo-irradiation of P-2a-2 films.

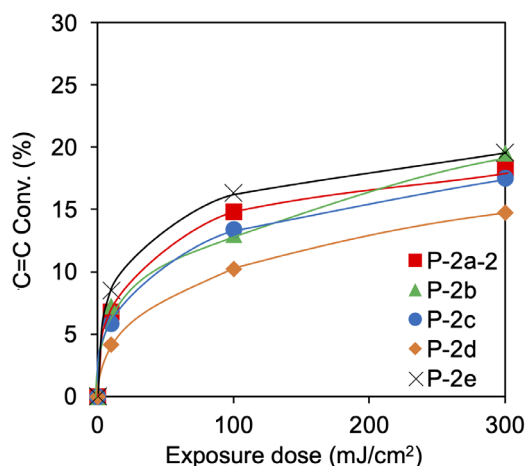


Fig. 2. Conversion of C=C peak area as a function of exposure dose during the photo-irradiation of P-2 films.

solutions such as Na_2CO_3 aq. and Me_4NOH aq., while P-2b~d did not dissolve in those solutions. Herein, the acid values of P-2b~d (61~64) were much lower than those of P-2a-2 and P-2e (86 and 89, respectively), which resulted in the alkaline solubility. Therefore, the development of P-2a-2 and P-2e films was carried out using 0.1 wt% aqueous Na_2CO_3 solution, while 1,4-dioxane/water (8/2, v/v) solution was used for P-2b~d.

The characteristic curves of P-2 for the photoresist properties were obtained by plotting the normalized film thickness after the development as a function of exposure dose (Fig. 3). The sensitivity ($D_n^{0.5}$) was defined as the exposure dose where the irradiated films retain 50% thickness of the original film after the development. The $D_n^{0.5}$ of P-2a-2 (7 mJ/cm^2) with POSS moiety was much smaller than that of its non-POSS-containing counterpart, P-2e (38 mJ/cm^2) (Fig. 3a), indicating that the POSS group contributed to the enhancement of the sensitivity. Herein, the photoreaction ratios of P-2a-2 and P-2e at the same exposure dose were almost the same (Fig. 2). These results show that P-2a-2 was insolubilized at fewer reaction ratio of the methacryloyl side chains compared to P-2e owing to the POSS moiety. On the other hand, P-2b and P-2c with alicyclic side chains in addition to the POSS group showed further higher sensitivity with $D_n^{0.5}$ of 2 mJ/cm^2 for P-2b and 4 mJ/cm^2 for P-2c (Fig. 3b). These results indicate that the alicyclic structures also contribute to the increased sensitivity of the photopolymers. Meanwhile, the sensitivity of P-2d ($D_n^{0.5} = 14\text{ mJ/cm}^2$) was lower than those of P-2b and P-2c, probably due to the slower photoreaction of P-2d as observed in the FT-IR study (Fig. 2).

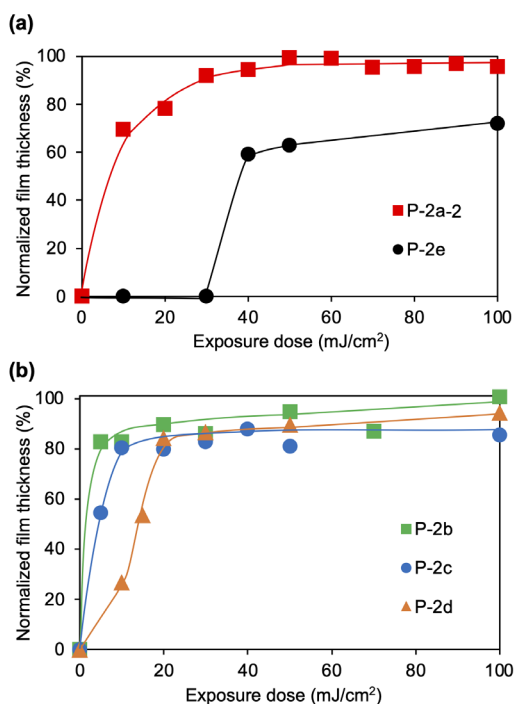


Fig. 3. Characteristic curves of (a) P-2a and P-2e (developer: 0.1 wt% Na_2CO_3 aq.) and (b) P-2b, c, and d (developer: 1,4-dioxane/water = 8/2, v/v).

4. Conclusion

In this study, we synthesized the pendant POSS-containing photopolymers by 2 steps via radical copolymerization using MA followed by the addition of HEMA to the MA moiety, and their physical and photoresist properties were investigated. The MA-based synthetic protocol enables the simultaneous incorporation of methacryloyl group for photocuring and carboxy group for solubilization in aqueous developers. The pendant POSS group contributed to the low dielectric properties and photosensitivity of the photopolymers. In addition, the incorporation of alicyclic structures to the photopolymers was shown to be efficient for enhancement of the thermal, low dielectric, and photoresist properties with their rigid and non-polar characters. This study offers beneficial insight to design improved photopolymers for various applications.

References

1. J. V. Crivello and E. Reichmanis, *Chem. Mater.*, **26** (2014) 533.
2. H. Xu, V. Kosma, E. P. Giannelis, and C. K. Ober, *Polym. J.*, **50** (2018) 45.
3. S. H. Mir, L. Nagahara, T. Thundat, P. M.-Tabari, H. Furukawa, and A. Khosla, *J. Electrochem. Soc.*, **165** (2018) B3137.
4. R. H. Baney, M. Itoh, A. Sakakibara, and T. Suzuki, *Chem. Rev.*, **95** (1995) 1409.
5. H. Zhou, Q. Ye, and J. Xu, *Mater. Chem. Front.*, **1** (2017) 212.
6. F. Chen, F. Lin, Q. Zhang, R. Cai, Y. Wu, and X. Ma, *Macromol. Rapid Commun.*, **40** (2019) 1900101.
7. D. B. Cordes, P. D. Lickiss, and F. Rataboul, *Chem. Rev.*, **110** (2010) 2081.
8. F. Ke, C. Zhang, S. Guang, and H. Xu, *J. Appl. Polym. Sci.*, **127** (2013) 2628.
9. H. W. Ro and C. L. Soles, *Mater. Today.*, **14** (2011) 20.
10. V. Jakubek, X. Q. Liu, V. R. Vohra, K. Douki, Y. J. Kwark, and C. K. Ober, *J. Photopolym. Sci. Technol.*, **16** (2003) 573.
11. E. Tegou, V. Bellas, E. Gogolides, P. Argitis, D. Eon, G. Cartry, and C. Cardinaud, *Chem. Mater.*, **16** (2004) 2567.
12. E. Tegou, V. Bellas, E. Gogolides, and P. Argitis, *Microelectron. Eng.*, **73–74** (2004) 238.
13. H. Ito, H. D. Truong, S. D. Burns, D. Pfeiffer, and D. R. Medeiros, *J. Photopolym. Sci. Technol.*, **19** (2006) 305.
14. A. M. Douvas, F. V. Roey, M. Goethals, K. G. Papadokostaki, K. Yannakopoulou, D. Niakoula, E. Gogolides, and P. Argitis, *Chem. Mater.*, **18** (2006) 4040.
15. R. Sooriyakumaran, H. Truong, L. Sundberg, M. Morris, B. Hinsberg, H. Ito, R. Allen, W. S. Huang, D. Goldfarb, S. Burns, and D. Pfeiffer, *Proc. of SPIE.*, **5753** (2022) 329.
16. H. Wu and K. E. Gonsalves, *Adv. Mater.*, **13** (2001) 670.
17. K. E. Gonsalves, M. Thiyagarajan, K. Dean, P. Santiago, L. Rendon, A. Jeyakumar, and C. L. Henderson, *Proc. of SPIE.*, **5753** (2005) 467.
18. J. H. Choi, P. H. Kang, Y. C. Nho, and S. K. Hong, *Solid. State. Phenom.*, **119** (2007) 299.
19. J. Rathore, Q. Dai, B. Davis, M. Sherwood, R. D. Miller, Q. Lin, and A. Nelson, *J. Mater. Chem.*, **21** (2011) 14254.
20. H. M. Lin, S. Y. Wu, P. Y. Huang, C. F. Huang, S. W. Kuo, and F. C. Chang, *Macromol. Rapid Commun.*, **27** (2006) 1550.
21. H.-W. Su, W.-C. Chen, W.-C. Lee, and J.-S. King, *Macromol. Mater. Eng.*, **292** (2007) 666.
22. Y. Ishida, T. Hayakawa, M. Kakimoto, and Y. Kimae, *J. Photopolym. Sci. Technol.*, **21** (2008) 155.

JOURNAL OF PHOTOPOLYMER SCIENCE AND TECHNOLOGY

Volume 36, Number 4, 2023

- Novel Photoinitiator System for Simultaneous Physical Drying and Free Radical Polymerization of Water-Borne Dispersions with Near-Infrared Excitation (Dedicated to D.C. Neckers (1938–2022) and Y. Yagci (1952–2023) according to their achievements in photopolymer science) 205
Lukas Appelhoff, Nicolas Hornemann, Remco Fokkink, Jochen S. Gutmann, Thomas E. Kodger, and Bernd Strehmel
- Physical and Chemical Drying of Coatings with NIR Absorbers to Replace Oven Technologies 213
Sascha Driesen, Nicolai Meckbach, Jochen S. Gutmann, and Bernd Strehmel
- The Design and Synthesis of New NIR-Active Sensitizers for Use in Photochemical Processes and Controlled Polymerizations 221
Nicolai Meckbach, Sascha Driesen, Jochen S. Gutmann, and Bernd Strehmel
- High Resolution and Low Stress Photo-Definable Polyimide 227
Tomoki Sakai, Yumiko Okuda, Keigo Kato, Kazuyuki Matsumura, and Hitoshi Araki
- Structure Characterization of Polymer Nano-Film on the Difference of Lattice Point Compounds 231
Shin-ichi Kondo, Kazuma Yoshimura, Naoki Doi, Yasushi Sasai, Yukinori Yamauchi, and Masayuki Kuzuya
- Preparation of a Polysilane-Methacrylate Copolymer with Two Methacrylate Species 237
Yukihito Matsuura, Chihiro Amasaki, Tomoya Hasegawa, Masanobu Ohkita, and Tomoharu Tachikawa
- Photomechanical Rolling Motion of Mixed Molecular Glass Microspheres Containing an Azobenzene-based Amorphous Molecular Material 243
Hajime Nigorikawa and Hideyuki Nakano
- Measurement of Liquid Film Thickness Distribution Formed on a Two-fluid Jet Sprayed Surface Using a Fiber Optic Probe 249
Shinsuke Watanabe, Yuki Mizushima, Hiroki Takahashi, Satomi Hamada, Masayoshi Imai, and Toshiyuki Sanada
- Surface Modification of Fluoropolymers by Atomic Hydrogen 253
Akira Heya, Hideo Otsuka, and Koji Sumitomo
- Synthesis and characteristics of maleic anhydride-based photopolymers with pendant POSS groups for negative tone photoresists 261
Haruka Onoda, Akira Takahashi, Nobuhito Ito, Kazuya Sato, and Atsushi Kameyama